-307

Numerical Simulation of Global Formation of Auroral Arcs

December, 1979

Akira Miura

Geophysics Research Laboratory
University of Tokyo

CONTENTS

Acknowledgement
ABSTRACT
Chapter I. GENERAL INTRODUCTION 1
Chapter II. A REVIEW OF OBSERVATIONAL RESULTS IN ASSOCIATION WITH QUIET AURORAL ARCS 4
1. Auroral oval and quiet auroral arcs 5
2. Large-scale electric fields and currents in the auroral region ionosphere 6
3. Perturbation electric fields associated with auroral arcs 10
4. Particle precipitation, field-aligned currents and electrojets associated with quiet auroral arcs 11
Chapter III. A REVIEW OF THE THEORY OF QUIET AURORAL ARCS 14
1. A review of the theory of formation of quiet auroral arcs 14
2. Precipitation of auroral electrons 17
3. Physical picture of the ionosphere-magnetosphere feedback instability 21
4. Basic equations 24
5. Stability analysis 28
Chapter IV. GLOBAL FORMATION OF AURORAL ARCS 31
1. Introduction 31
2. A lumped constant circuit description of the magnetosphere 33
3. Numerical models and procedures 39
4. Numerical results and their physical interpretation .. 46
4-1. Unperturbed states 46
4-2. Dynamic evolution of auroral arcs 49
4-3. Dependence of the auroral arc development on the ionospheric electron density distribution . 53
4-4. Dependence of the auroral arc development on the magnetospheric conditions 57
Chapter V. DISCUSSION 60
1. Comparison of numerical results with observational results 60
2. Global distribution of quiet auroral arcs 64
Chapter VI. SUMMARY AND CONCLUSION 66
APPENDIX A. THE ENERGY SOURCE OF THE FEEDBACK INSTABILITY 69
APPENDIX B. NUMERICAL PROCEDURES 87
APPENDIX C. AN ALTERNATING DIRECTION IMPLICIT SCHEME FOR THE GENERAL ELLIPTIC PARTIAL DIFFERENTIAL EQUATION 91

ACKNOWLEDGEMENTS

I wish to express my sincere gratitude to Professor T. Sato, who has given me continuous enlightenment and encouragements throughout the course of this work, and to Professor T. Tamao for his important comments and encouragements, which have helped illuminate this thesis.

It is a pleasure to thank Professors N. Fukushima, T. Oguti, S. Kokubun, and Drs. E. Kaneda, T. Iijima, K. Hayashi for numerous helpful discussions and important comments throughout the course of this work. I also thank Professors T. Obayashi, A. Nishida, Y. Inoue and Drs. Y. Kamide and H. Fukunishi for their important comments and suggestions on this work, from which I have benefited greatly.

Thanks are also due to Dr. K. Makita and Mr. H. Taniguchi for helpful discussions throughout the course of this work and to Mr. M. Tanaka, Mr. M. Ozaki, Mr. M. Kunitake, Mr. S. Fujita, and Mr. S. Ohtsuka for their interests and comments on this work.

Numerical computations in this thesis were performed by using HITAC 8700-8800 at the Computer Center, University of Tokyo.

Abstract

Global simulation of the formation of auroral arcs has been performed for a three-dimensional coupling system between the ionosphere and the magnetosphere. First, a realistic model of the auroral oval, incorporating with two pairs of the large-scale stationary Birkeland currents, the electric potential difference over the polar cap, and the day-night asymmetry of the electron density distribution, is constructed as an initial state. Second, dynamic evolution of auroral arcs in the oval is simulated under reasonable ionospheric and magnetospheric conditions, by solving a system of coupling equations including a positive feedback effect from the magnetosphere to the ionosphere. It is found that multiple auroral arcs with their fully developed form appear in the dark sector of the auroral oval, more preferentially in the evening sector, within a time scale of the order of a few to several minutes. The fully developed auroras consist of multiple arcs, each having a shape elongating parallel to the east-west direction, a couple of thousands kilometers in its length, and 10 to 40 km in width. A pair of small-scale Birkeland currents, one is upward directing and the other downward, develops associated with each arc. Their intensity reaches to 10 to 200 $\mu A/m^2$ at the 110 km height. Intense precipitation of auroral electrons induces a strong enhancement of the ionospheric electron density ($2 \times 10^{11} m^{-3} \sim 10^{12} m^{-3}$) and the associated electrojet intensity reaches to 5 to 20 kA. Each pronounced density enhancement (auroral arc) is strongly polarized by the background north-south current so that the electric field inside the arc is reduced considerably compared with its stationary value. The potential difference in each arc due to the above

polarization process attains to several hundreds to a few kilovolts. The overall structure of the developed auroras is found to be dependent largely upon the global distribution of the electron density, the stationary large-scale Birkeland currents and the associated electric field intensity in the auroral oval: Auroral arcs appear only in the night sector but not in the day sector owing to the large recombination loss in the sunlit hemisphere. They appear predominantly in the region of the large-scale upward Birkeland current, where the situation is more favorable in growing a perturbation to a large intensity. Important roles of the magnetospheric response to the potential perturbation in the ionosphere in the formation process of auroral arcs are also clarified. For instance, the shorter the bounce time of the Alfvén wave propagating parallel to a field line, the narrower the width of the arc; this is a fact demonstrating clearly that the ionospheric perturbation, which is nearly resonant with the Alfvén oscillations in the magnetosphere, can grow into auroral arcs in the coupling system. Both qualitative and quantitative results of the numerical simulation are in good agreement with several observational results of the quiet auroral arcs and electric fields in the vicinity of auroral arcs.

I. GENERAL INTRODUCTION

Our knowledge of the global characteristics of the auroral region ionosphere and the local characteristics of auroral arcs has progressed very much in recent years. The large-scale Birkeland currents have been found to be concentrated in two neighboring principal zones surrounding the geomagnetic pole, which almost coincide with the location of the auroral oval [Armstrong and Zmuda, 1970; Iijima and Potemra, 1976 a]. Ionospheric conductivities and currents in the auroral region were investigated by Brekke et al. [1974]. They have shown that the ratio of Σ_H to Σ_p is almost 2 in the quiet period.
Electric field measurement in auroral and polar latitudes by Banks et al. [1973] has shown that the electric fields are predominantly northward in the evening and afternoon sectors and are southward in the morning and prenoon sectors. Horwitz et al. [1978] have recently made an extensive study of the latitudinal distributions of the convection electric field, the Hall and Pedersen conductivities and the horizontal current for the range of invariant latitudes 63° - 68°. Their results show the existence of strong electric fields with amplitudes of 50 - 100 mV/m, which are typically northward in the afternoon-evening sector and southward in the morning sector, in agreement with the result of Banks et al. [1973].

Local characteristics of quiet auroral arcs and the relationship among the macroscopic quantities associated with quiet auroral arcs have also been clarified by a number of rocket experiments of the Rice university group [Cloutier et al., 1973; Park and Cloutier, 1971; Casserly and Cloutier, 1975; Sesiano and Cloutier, 1976]. Their experiments have revealed that small-scale, field-aligned currents with an intensity of

the order of 10 $\mu A/m^2$ are associated with quiet auroral arcs and strong enhancement of auroral electrojets of either westward or eastward direction appears in coincidence with the arcs. Electric fields in the vicinity of auroral arcs have been measured by Aggson [1969], Wescott et al. [1969], and Maynard et al. [1973]. They have shown that electric fields are large just outside of the auroral arcs, whereas those within the arcs are very small.

The principal purpose of the present thesis is to carry out a numerical simulation of global formation of quiet auroral arcs with a view to understanding the interrelationship among the above mentioned observational facts: First, a realistic background model of the quiet auroral oval is constructed on the basis of the related observational results. This model of the auroral oval includes two pairs of large-scale Birkeland currents, large-scale polar cap electric fields, and a day-night asymmetry of the electron density distribution. Next, a numerical simulation is performed under the reasonable ionospheric and magnetospheric conditions in order to clarify the dynamic process of the quiet arc formation as a result of the ionosphere-magnetosphere coupling via Alfvén wave. The interrelationship among the electric fields, electrojets, and field-aligned currents, etc, associated with the quiet arcs will be self-consistently interpreted by the present numerical simulation.

Previous theory underlying the present work is the feedback theory of auroral arcs, some prototypes of which were previously discussed [Sato and Holzer, 1973; Holzer and Sato, 1973; Ogawa and Sato, 1971; Atkinson, 1970]. All of these works have shown that the ionosphere plays a leading role in the formation of quiet auroral arcs. Quite recently, Sato [1978] has shown that the feedback theory can explain very well many of the important characteristics of quiet auroral arcs.

In chapter II of this thesis, extensive observational results associated with quiet auroral arcs are reviewed. In chapter III, a brief summary on the theory of quiet auroral arcs is given, together with the mechanism of field-aligned acceleration of auroral electrons (III-2). The feedback mechanism is applied to a realistic three-dimensionally coupled ionosphere-magnetosphere system in chapter IV: First, a differential equation, which describes the three-dimensional hydromagnetic coupling relation between the ionosphere and magnetosphere in terms of the magnetic field line length (2ℓ) and the Alfven speed (V_A), is derived in IV-2 from the ideal MHD equations. Second, a numerical model of the quiet-time auroral oval is introduced in IV-3. Third, numerical simulations under several ionospheric and magnetospheric conditions are performed in IV-4. Numerical results are discussed in comparison with the observational results in V-1 and global distribution of quiet auroral arcs is physically interpreted in V-2. Summary and conclusion are given in Chapter VI. In Appendix A the dispersion relation of the feedback instability is discussed in detail and the energy source of the instability is clarified. Details of the important numerical procedure in the present simulation are given in Appendices B and C.

II. A REVIEW OF OBSERVATIONAL RESULTS ASSOCIATED WITH QUIET AURORAL ARCS

Important observational results associated with the quiet auroral arcs are reviewed in this chapter. They are important in constructing numerical models and interpreting numerical results given in chapter IV. Quiet auroral arcs [Cloutier et al, 1970; Vondrak et al., 1971] are stable auroral arcs which appear in quiet period without any substorm activity and they extend in the east-west direction with a typical length of a few thousand kilometers. They are a few tens of kilometers in width and are associated with a pair of intense small-scale upward and downward field-aligned currents [Cloutier et al., 1973; Park and Cloutier, 1971; Casserly and Cloutier, 1975; Sesiano and Cloutier, 1976].

Let us briefly discuss the relationship of quiet auroral arcs to other auroral forms. Visible auroral arcs are conventionally classified into several types [Akasofu, 1977; Oguti, 1978; Davis, 1978]. The most common classification is based on whether aurora is discrete or diffuse. According to Akasofu [1977], a discrete aurora is a curtain-like structure and appears as a single arc or is separated from other arcs by a dark space of a few tens of kilometers in width. A diffuse aurora, on the other hand, is defined as either a broad band of luminosity at least several tens of kilometers in width or a group of discrete aurora which are closely packed along a rather narrow east-west belt. One important aspect of the diffuse aurora is that it is nearly conjugate. According to this classification, it appears plausible to identify the quiet auroral arcs observed by the Rice university group as individual discrete auroral arcs forming a diffuse aurora. A group of faint discrete auroral forms occurring on the equatorward side of the discrete aurora in the evening sector [Oguti, 1978] might possibly correspond to the quiet auroral arcs.

Important characteristics of the auroral oval and quiet auroral arcs are reviewed in II-1. The background structure of the auroral oval, which is important in constructing numerical models and in interpretation of numerical results, is reviewed in II-2. II-3 and II-4 consist of the summary on important observational results associated with quiet auroral arcs.

II-1. Auroral oval and quiet auroral arcs

It is well known that auroral arcs appear predominantly in a latitudinally confined region around the magnetic pole, the so-called auroral oval. Feldstein [1966] has defined the auroral zone as a region where the frequency of auroral appearances exceeds 60%. His observation has shown that the auroral zone has the following characteristics: It has an oval shaped form surrounding the geomagnetic pole. It is located at geomagnetic latitude of 67° - 72° in nighttime and of 77° - 80° in daytime for Kp = 0 - 1 (the left panel of Figure 1). It expands to a substantial degree in a latitudinal range on disturbed days (Kp > 5).

Of particular importance associated with the appearance of auroral arcs in the auroral oval is the existence of large-scale field-aligned currents [Armstrong and Zmuda, 1970; Iijima and Potemra, 1976 a; Iijima and Potemra, 1976b]. Armstrong et al. [1975] have found that all the visual auroral arcs lie within the latitudinal range occupied by the Birkeland current flow. Kamide and Akasofu [1976] have analyzed a large amount of satellite magnetic data in the evening sector. They have shown that while discrete auroral arcs are confined within the region of the upward field-aligned current, the region of diffuse auroras, located equatorward of the discrete auroras, appears to coincide with the region of the downward field-aligned current.

Stable quiet auroral arcs which appear in quiet times without any substorm activity are likely to have a different formation mechanism from that of breakup and postbreakup arcs. Lassen and Danielsen [1978] have shown that quiet time auroral arcs are ordered along the statistical auroral oval and arc patterns in the oval are most prominent when B_z is negative. Belon et al. [1969] investigated spatial and temporal conjugacy of quiet auroral arcs at high latitudes near magnetic midnight. The magnetic activity was very low throughout the period of their experiment, however, auroras were observed between dp latitudes 66° and 71°. On the basis of the high degree of auroral conjugacy they have concluded as follows: The geomagnetic field lines are closed, stable, and relatively undistorted up to dp latitude 71° during magnetically very quiet periods. The field lines control strongly precipitation of auroral particles at all dp latitudes, where auroras are observed (dp latitudes 65° to 71°). This experimental result may indicate that quiet auroral arcs are caused by a mechanism operating symmetrically in both hemispheres with the stable closed field lines.

II-2. Large-scale electric fields and currents in the auroral region ionosphere

Large-scale field-aligned currents and electric fields in the auroral region ionosphere

A considerable progress has thus far been made experimentally in clarifying the global distribution of field-aligned currents and electric fields in the auroral region ionoshere. A result of the observation of the high latitude field-aligned current distribution by Iijima and Potemra [1976 a, 1976 b] is shown in the right panel of Figure 1. Large-scale upward and downward field-aligned current pairs are seen to be concentrated in two neighboring principal zones which almost coincide with the location of the auroral oval (see the left panel

of Figure 1). Of primary importance in this figure is that the field-aligned current directions on the dusk side are opposite to those on the dawn side. The region 1 (poleward region) current pairs persist even during the period of very low geomagnetic activity with a value of current density $>0.6\mu A/m^2$ for Kp = 0. They attain the the maximum current density of $2\mu A/m^2$ in the forenoon sector during moderately disturbed conditions (2- < Kp < 4+). In region 2 (equatorward region) the largest current density occurs in the night side with a peak value of $1 - 1.3\mu A/m^2$ for 2- < Kp < 4+. The currents in region 1 are statistically larger in density than the currents in region 2 at all local times except the midnight sector. From the continuity of electric current, it is expected that the poleward and equatorward current sheets are partially short-circuited in the auroral region ionosphere via latitudinal Pedersen currents [Armstrong and Zmuda, 1970]. Observational result by Horwitz et al. [1978] agrees with this simple view. That is, latitudinal currents in the auroral region ionosphere are flowing in such a direction as to connect the two field-aligned current sheets, i.e., northward on the dusk side and southward on the dawn side.

Regardless of geomagnetic activities, the direction of the electric fields in the ionosphere is predominantly northward in the afternoon-evening sector, while it is southward in the morning sector [Mozer, 1971; Heppner, 1972; Banks et al., 1974; Mozer and Lucht, 1974; Horwitz et al., 1978]. Banks et al. [1973] have shown that the westward electric field is generally much smaller than the north-south component in the auroral zone. Furthermore, they have shown that the north-south component of the electric field is often larger by a factor of 3 to 10 than the east-west component. According to Mozer and Lucht [1974] the large-scale north-south electric field

component at the auroral latitude is typically a factor of about 3 larger than the westward component. The southward component intensity changes from about +30 mV/m at the dawn to -30mV/m at the dusk. These results are in agreement with observational results by Horwitz et al. [1978]. Three panels in Figure 2 show observational results of electric field distributions at the auroral latitude 63° - 68° for three moderately disturbed days. It is shown in this figure that strong electric fields in the range 50 - 100 mV/m are typically directed northward in the afternoon-evening sector and southward in the morning sector. Comparison of these panels with the right panel of Figure 1 suggests that substantial parts of region 1 and region 2 large-scale field-aligned current sheets are closed by the Pedersen currents due to the north-south component of large-scale electric fields.

Now let us turn our attention to the east-west component of the electric field in the ionosphere. Heppner [1977] derived an empirical relationship between the Kp index and the total potential difference across the polar cap ΔV as $\Delta V = 20\ kV + Kp \times 20\ kV$. Mozer and Lucht [1974] have shown that the east-west component of the electric field at the auroral latitude directs westward in the night sector and eastward in the day sector and their intensity is usually below 10 mV/m in the quiet period. According to Mozer [1971] the westward electric field is intensified prior to the substorm onset near local midnight. Banks et al. [1974] have shown that a westward electric field in magnitude from -10 to +35 mV/m exists during a period of magnetic disturbance in the midnight sector.

Figure 3 is a diagram summarizing the basic structure of large-scale electric fields at the auroral latitude and their spatial relationship with the large-scale field-aligned currents.

Horizontal current distribution in the auroral region ionosphere

Three panels in Figure 4 show large-scale horizontal current distribution at the auroral latitude [Horwitz et al, 1978] for the same three disturbed days as shown in Figure 2. Local midnight is located near at 1100 UT in these panels. As is required from the direction of the electric field in Figure 2, east-west currents, major part of which are Hall currents driven by the large north-south electric field, are eastward on the dusk side and westward on the dawn side. Their intensity is typically 1 A/m. Furthermore, these panels show that the latitudinal currents direct northward on the duskside and southward on the dawnside. Substantial parts of these latitudinal currents can be ascribed to Pedersen currents driven by the north-south electric fields shown in Figure 2 by the following reason: First, a ratio of Σ_H to Σ_p is about equal to 2 for quiet periods in all local times [Brekke et al., 1974]. Second , the north-south electric field component is usually several times larger than the east-west component. It should be emphasized, however, that an important effect arises from the presence of the westward electric field in the night sector of the auroral oval. That is, since the westward electric field drives a northward Hall current in the night sector, the total northward current (Pedersen plus Hall current) increases on the evening to midnight sector but the total southward current decreases on the midnight to morning sector. Indeed, such a tendency is recognized in Figure 4. This dawn-dusk asymmetry of the north-south current may have an important influence upon the global distribution of quiet auroral arcs.

Global distribution of height integrated Hall and Pedersen conductivities, which controls significantly the horizontal current distribution in the auroral region ionosphere, has been studied in detail by Brekke et al. [1974]. The upper panel of Figure 5 shows that Hall and Pedersen conductivities

change as much as several to ten times between the day and the night in quiet days; this change is due to a daily variation by solar EUV radiation. A remarkable result shown in the lower panel is that a ratio between the height integrated Hall and Pedersen conductivities is fairly constant and close to 2 for all local times during quiet days.

II-3. Perturbation electric fields associated with auroral arcs

The large-scale electric fields and currents are locally modified strongly by the intense precipitation of auroral electrons causing a strong enhancement of conductivities inside auroral arcs. As we have seen in the previous subsection, the ambient large-scale electric field can take a different configuration in the auroral region ionosphere; although the north-south electric fields are usually predominant, the westward electric field is intensified at the midnight sector in periods prior to substorm onsets [Mozer, 1971] or in magnetic disturbance [Banks et al., 1974]. The relative orientation between the auroral arc and the background electric field is important in determining a magnitude of polarization electric field inside the auroral arc [Boström, 1964; Beaujardiere 1977].

It is an important test for any model to explain apparently contradictory experimental results concerning the relationship between the electric field and the auroral arc as shown in the following:

By using double probes Aggson [1969] has found that the electric field intensity decreases considerably inside auroral arcs. Wescott et al. [1969] have observed electric fields in the vicinity of stable auroral forms. They have shown that while electric field is large near an auroral arc, the field within the auroral arc is very low. It should be noted that in the period of their experiment the background large-scale

electric field was mainly in southward and its intensity, calculated from the cloud motion, was 10 - 30 mV/m. Maynard et al. (1973) have found that electric field becomes small in the region of large electron fluxes (4.7 keV). These experimental results may indicate that the electric field is reduced considerably from the background value inside the auroral arc. However, a number of experimental evidences do not indicate such a substantial decrease in electric field inside auroral arcs or even show a slight increase in them inside auroral arcs [Mozer and Fahleson, 1970; Carlson and Kelley, 1977]. One example is an experiment by Carlson and Kelly [1977]. They have shown that the electric field is large inside the visible arc (an active auroral arc during the late expansion phase of a substorm), correlated with the electron fluxes, and has a large equatorward component.

II-4. Particle precipitation, field-aligned currents and electrojets associated with quiet auroral arcs

Rice University group has made an extensive observation of Birkeland currents and electrojets associated with quiet auroral arcs [Cloutier et al., 1973; Park and Cloutier, 1971; Casserly and Cloutier, 1975; Sesiano and Cloutier, 1976]. Table 1 summarizes important observational results of their rocket-borne experiments for three different days. These results agree in that a pair of upward and downward field-aligned currents develop coincident with a visual arc, field-aligned current density associated with an arc system is a few to several tens $\mu A/m^2$ and intensity of auroral electrojets is several to a few tens of kA. The only important difference in Table 1 is the difference of electrojet direction between the experiment of Park and Cloutier [1971] and the other two experiments. This difference, however, is probably ascribable to the difference in the direction of the background electric field.

It is generally accepted that electrons with energy from 0.1 to 10 keV are most responsible for auroral forms in visible and near-infrared wavelengths that constitute a major part of the auroral morphology [Rees, 1969; Paulikas, 1971]. The flux of charged particles above a quiet auroral arcs was found to be primarily electrons in the energy range 2 - 18 keV [Vondrak et al., 1971]. A characteristic feature of the auroral electron spectrum associated with the discrete auroral form is the existence of monoenergetic peaks in its spectrum [Evans, 1968; Westerlund, 1969, Pazich and Anderson, 1975; Arnoldy et al., 1974]. Pazich and Anderson [1975] have shown that energy spectra of the electron flux measured by rocket-passage over visible aurora always exhibit a peak within the measured energy range; this peak is located in the energy range from $\sim$3 to $\sim$10 keV and the electron flux in regions of maximum flux tends to be the most field-aligned in the energy interval showing the highest intensity. Arnoldy et al. [1974] have shown that field-aligned peaks of electron energy spectrum in the various rocket flights are observed to occur in the range from 0.5 to about 5 keV. According to them these field-aligned electrons are very monoenergetic with full width at half maximum less than 1 keV. From the high degree of field alignment and the monoenergetic character, they have concluded that these events can be attributed to relatively cool plasma falling through an electric potential difference at altitudes not too far from the rocket altitude. Although energetic electrons are responsible for the visible emission they may not be principal carriers of field-aligned currents : Spiger and Anderson [1975] have calculated the magnitude of the sheet current associated with a quiet auroral arc from particle flux measurements in the range 0.5 - 20 keV. They have found that the magnitude is lower (by a factor of $\approx$ 5) than that calculated from the magnetometer measurements. Their conclusion

based on this result is that the majority of the current is carried by particles of energy < 500 eV.

III. A REVIEW OF THE THEORY OF QUIET AURORAL ARCS

In this chapter we shall review in detail the theory of formation of quiet auroral arcs [Sato, 1978; Sato and Holzer, 1973; Ogawa and Sato, 1971; Atkinson, 1970], which is underlying the present thesis. Important mechanisms of acceleration of auroral electrons are also reviewd briefly in §2, since the numerical model in chapter IV is based on an important assumption on the precipitation of auroral electrons. The physical picture of the feedback mechanism important in understanding numerical results in chapter IV is clarified in §3. In §4 and §5 basic equations and stability analysis are given.

III-1. A review of the theory of formation of quiet auroral arcs

Auroral arcs which appear in the quiet period are likely to have a different formation mechanism from that of breakup and postbreakup arcs. From a standpoint that the ionosphere-magnetosphere coupling plays an important role in the formation of quiet auroral arcs, Atkinson [1970] and Ogawa and Sato [1971] have proposed two different mechanisms of auroral arc formation.

Atkinson [1970] has proposed that a nonlinear instability involved in the ionosphere-magnetosphere coupled system, where the ionospheric Pedersen current is closed by polarization current in the magnetosphere, is responsible for a formation of auroral arcs. A serious difficulty in this model, however, is an assumption that the ionospheric electric field is perfectly mapped to the magnetosphere, i.e., the complete neglect of the induction field (current).

The basic idea underlying the models of Sato and coworkers is as

follows: If the upward field-aligned current (downward electron precipitation) and the ionospheric potential perturbation are properly phased, the ionospheric density enhancement is accelerated to grow with time by the precipitation of electrons flowing to neutralize the polarization charges arising from the original density enhancement and the unperturbed dc electric field. Ogawa and Sato [1971] have shown that a feedback loop, in which the Pedersen current is closed by the induction current flowing along the field line is unstable by the mechanism mentioned above. However, there was some difficulty in assumptions in their model. One assumption is that they have invoked a very low-frequency plasma instability to generate an ionization irregularity. Second, the phase lag between the electron precipitation and the ionospheric potential perturbation was given a priori in their model. To overcome these difficulties Sato and Holzer [1973] have proposed a model, in which one ionosphere is active and the other is passive. The phase difference between the ionospheric potential perturbation and the field-aligned current was determined by taking into account the capacitance and the inductance of the magnetosphere. By this proper choice of the phase difference, the model has successfully shown that arcs could develop spontaneously from an initial small seed without invoking any low-frequency plasma instability in the ionosphere. One difficulty in this model, however, was that the growth rate of the instability is not substantial in the electrojet layer height because of the Pedersen resistivity in the conjugate ionosphere.

Quite recently, Sato [1978] has proposed a model, in which the difficulty in Sato and Holzer's model is resolved by an assumption of symmetrically conjugate ionospheres. He has numerically integrated basic equations describing the feedback instability for a fixed value of the

north-south unperturbed current and for two fixed magnetospheric impedances (Z = 4.12 iH/S, 1.24 iH/S). Important results obtained are as follows:

1. An auroral arc can develop within a few tens of seconds from an initial seed if hot electrons take part in the instability.

2. A pair of oppositely flowing field-alinged currents develops associated with an arc. The upward component coincides with the density enhancement, whereas the downward one comes on either the equatorward or the poleward side, depending on the direction of the ambient horizontal current. The intenisty of the field-aligned current can be as large as the observed values, say 20 $\mu A/m^2$, for reasonable parameters.

3. The electrojet current can grow to a few thousand amperes and the induced potential associated with the arc can reach several hundred volts.

4. The induced electric field inside the arc is almost constant and different from outside.

III-2. Precipitation of auroral electrons

In previous section we have seen that the feedback instability can drive a local field-aligned current in the ionosphere-magnetosphere coupled system. However, another important step is required in applying the feedback instability to the formation of quiet auroral arcs. That is, precipitation of auroral electrons is necessary for the formation of auroral arcs. Since this thesis does not persue the microscopic process pertaining to acceleration of auroral electrons, a specific assumption must be made to combine the feedback instability and the precipitation of auroral electrons. In this section, therefore, we shall briefly review several mechanisms, which have been proposed to explain the acceleration of auroral electrons causing discrete auroral forms.

There is considerable evidence which indicate that auroral electrons are accelerated by parallel dc electric field in the region not too far from the ionosphere. Mozer et al. [1977] have observed an extremely large ($\lesssim$ 500 mV/m) dc electric fields (both in parallel and perpendicular direction) in spatially confined regions at altitudes below 8000 km in the auroral zone. These structures are found to be associated with intense electrostatic waves.

Swift (1965) is the first to point out the importance of the current driven instability at the topside ionosphere for acceleration of auroral electrons. He has proposed that when the field-aligned current in the auroral zone becomes intense enough to excite ion acoustic instability, anomalous resistivity is generated and the potential difference maintained by the resistivity is responsible for the acceleration of

auroral electrons. Kindel and Kennel [1971] have investigated in detail the marginal stability condition of current-driven electrostatic instabilities such as Buneman, ion acoustic and electrostatic ion cyclotron instabilities for the parameters of the topside ionosphere. They have shown that at the topside ionosphere where Te ~ Ti holds, thus the ion acoustic instability being heavily damped by the ion Landau damping, the electrostatic ion cyclotron wave is unstable to the smallest field-aligned electron current. One of their result is shown in Figure 6. In this figure the critical electron fluxes are plotted versus altitude by solid lines for various current driven instabilities. The dashed curves represent the variation of the current density with altitude on the assumption that the field-aligned current flux is conserved along a flux tube. It should be noted in this figure that current density greatly exceeds the critical value wherever the electron density decreases with height faster than the magnetic field; this place corresponds to the topside ionosphere.

Several theoretical attempts have thus far been made to explain physical mechanism to maintain the potential difference along the magnetic field line. Papadopoulos [1978] has suggested that anomalous resistivity driven by field-aligned electron current [Kindel and Kennel, 1971] leads to a generation of run away electrons, which gain the energy comparable to the parallel potential difference maintained by the anomalous resistivity. Block [1972] has shown a possibility that auroral electrons are accelerated by potential jump associated with a double layer. He has shown that a stationary potential double layer can be determined self-consistently

with a charge distribution along the field line. Swift [1975] has found that there is a time-independent solution for the Vlasov-Poisson equations, which describes one dimensional double layer oblique to field lines. In this case, however, the double layer exists in the distance the order of the ion Larmor radius owing to the polarization drift of ions by the perpendicular electric field component. Furthermore, in order to explain the energy source of the double layer, Swift [1977] has proposed that the energy of earthward streaming of plasma sheet protons is fed into the double layer via the inverse cascade of flute-mode ion cyclotron turbulence. That is, he has attributed the V-shaped potential distribution to the large scale $\vec{E} \times \vec{B}$ eddy turbulence excited by microscopic ion gyrational motion. Kan and Akasofu [1976] have suggested that an earthward flow of plasma in a very thin layer near the outer surface of the plasma sheet can not only generate the V-shaped potential, but also drive a field-aligned current. They have proposed that anomalous resistivity and/or double layer driven by the field-aligned current is responsible for field-aligned energy spectrum of the auroral electrons [Arnoldy et al, 1974]. Hasegawa [1976] has shown that a shear Alfvén wave resonantly excited by the large-scale incompressible MHD surface wave is mode-converted to a kinetic Alfvén wave. He has proposed that a MHD scale parallel potential difference along an entire field line associated with the kinetic Alfvén wave gives rise to acceleration of auroral electrons.

In applying any mechanisms mentioned above to the acceleration of auroral electrons, however, a key problem is whether such a time independent

state (turbulent or laminar) can be realized as a time dependent problem or not. Such a problem has recently been attacked successfully by numerical simulations. Hubbard and Joyce [1979] have shown that a Buneman instability in a current-carrying plasma develops into a double layer in the time asymptotic state. Quite recently, Sato and Okuda [1979] have shown by a particle simulation that a double layer is formed from the ion acoustic instability. They have shown that anomalous resistivity generated by the ion acoustic instability causes the buildup of a dc potential which in turn accelerates electrons further to enhance the original instability leading to the formation of double layers.

As we have seen above, a possible energy source for anomalous and/or double layer at the topside ionosphere is an intense field-aligned electron current. If such a field-aligned electron current is driven by some macroscopic dynamics involved in the ionosphere-magnetosphere coupled system, anomalous and/or double layer would be formed in the topside ionosphere, the viability being demonstrated by above mentioned particle simulation [Sato and Okuda, 1979]. As proposed by many authors, the parallel dc potential maintained by the anomalous and/or double layer would then accelerate electrons to the energy to cause visual auroral forms.

III-3. Physical Picture of the ionosphere-magnetosphere feedback instability

Physical picture of the ionosphere-magnetosphere feedback instability responsible for quiet auroral arc formation is given in this section.

The feedback mechanism is summarized in Figure 7. For comparison with the numerical results given in Chapter IV, let the left side of the figure correspond to the north and the magnetic field be downward. Given a northward component of the large-scale horizontal current j_{IO} which may be the Pedersen current closing the large-scale Birkeland (field-aligned) current or the Hall current driven by the large-scale westward electric field, then a small density perturbation δn in the ionosphere, no matter how small and by whatever mechanism it may be produced, is naturally accompanied by polarization charges; Positive charges accumulate in the northern part of the density peak and negative charges accumulate in its southern part as indicated by positive and negative signs, respectively, in Figure 7. In the absence of field-aligned current, the density irregularity moves with the electric $(\vec{E}_o \times \vec{B}_o)$ drift velocity. Therefore, let us take a reference system that moves with the zeroth-order electric drift, namely, a system moving with the field lines. In the actual system, electrons can freely move along the field lines to neutralize the ionospheric space charges that are primarily caused by the ion (Pedersen) motions associated with the perturbation electric fields. Specifically, electrons come down along the field lines toward the positive part of the potential perturbation to neutralize the positive charges and go up from the negative part denoted by the vertical dashed arrows in Figure 7. As a result of this field-aligned motion of electrons and the horizontal motion of ions in the ionosphere, a closed field-aligned current loop is

set up as indicated by $j_{||}$. Hence, the plasma density in the positive part of the potential perturbation increases (convergence of the plasma) but decreases in the negative part (divergence of the plasma). These motions cause an additional drift of the density perturbation V_{ph} in the direction of j_{IO}. This spontaneous drift under the action of the induced field-aligned current produces a new physical effect on the development of the perturbation; since it moves relative to the geomagnetic field, the potential perturbation can be considered as an ac generator in the reference system fixed to the zeroth-order magnetic field. Thus, the induced field-aligned current becomes a time-varying current. We must therefore consider a temporal response of the magnetosphere to the ionospheric potential generator, namely, a magnetohydrodynamic response of the magnetosphere.

Let the magnetospheric response be inductive as illustrated in the middle portion of Figure 7. Then upward field-aligned current undergoes a phase lag by $\pi/2$ behind the positive potential perturbation with respect to the direction of j_{IO}. This means that the position of the downward flow of electrons coincides with the peak position of the density perturbation and the position of the upward flow coincides with the valley of the density perturbation. As a result of this positive feedback loop the initial density perturbation grows with time. On the other hand, let the magnetospheric response be capacitive. Then, upward field-aligned current leads to the positive potential perturbation by $\pi/2$ in phase, so that electrons flow into the valley of the density perturbation as shown in the bottom of Figure 7. Thus the perturbation decays with time.

From the above physical consideration, it is obvious that a necessary condition for the feedback instability is that the magnetosphere responds

to the ionospheric potential perturbation as an inductive load. Generally, the magnetospheric plasma responds to the ionospheric electrostatic potential generator as an inductance or a capacitance depending on the frequency of the potential variation seen in the reference frame fixed to field lines. In other words, the response of the magnetosphere depends on whether the substantial closure current in the magnetosphere is induction current or polarization current. It is therefore expected that an ionospheric perturbation with a frequency, hence, with a latitudinal scale that automatically meets the above requirement, grows spontaneously subject to the ionosphere-mangetosphere feedback mechanism.

III-4. Basic equations

As we have seen in the previous section, a precipitation of electrons (field-aligned current) downward into the ionosphere is controlled by the polarization potential arising from the density perturbation and the unperturbed current in the ionosphere. This means that the original density perturbation in the ionosphere is affected by the effect (polarization potential) it produces. In order to describe this closed feedback system, therefore, the relationships among the ionospheric density perturbation, the ionospheric potential perturbation,and the field-aligned current at the ionospheric height must be specified self-consistently by coupled equations. The coupled equations are formulated as follows [Sato, 1978; Atkinson, 1970].

The flow velocities of electrons (minus sign) and ions (positive sign) in the E-layer height are given by

$$\vec{V}^{\pm} = \mu_H^{\pm} \frac{\vec{E} \times \vec{B}_o}{B_o} \pm \mu_p^{\pm} \vec{E} \tag{3.1}$$

where $\vec{B}_o$ is the ambient magnetic field and $\vec{E}$ is the electric field; $\mu_H^{\pm}$ and $\mu_p^{\pm}$ are the Hall and Pedersen mobilities, respectively. In (3.1) we have neglected effects of the neutral wind and diffusion.

Continuity equations of electrons and ions in the ionosphere are

$$\frac{\partial n}{\partial t} + \vec{\nabla}_\perp \cdot (n\vec{V}^-) = - \frac{\gamma + 1}{eh} j_h - \frac{1}{eh} j_c - \alpha(n^2 - n_o^2) \tag{3.2}$$

$$\frac{\partial n}{\partial t} + \vec{\nabla}_\perp \cdot (n\vec{V}^+) = - \frac{\gamma}{eh} j_h - \alpha(n^2 - n_o^2) \tag{3.3}$$

where $\vec{\nabla}_\perp$ is the divergence operator in the plane perpendicular to the magnetic field $\vec{B}_o$, j_h and j_c are the current of precipitating auroral electrons ($j_h \leq 0$) and the current of field-aligned cold electrons, respectively; n is the plasma density, since the plasma is quasi neutral $n = n^+ \simeq n^-$ in the low frequency range of our concern, n_o is the ambient plasma density, γ is the ion pair production rate, α is the recombination coefficient, and h is the effective height range of the ionospheric region of interest. In (3.3) we have defined $j_\parallel > 0$ for the downward current and neglected ion contribution to the field-aligned current.

Substitution of (3.1) into (3.2) and (3.3) yields

$$\frac{\partial n}{\partial t} + \mu_H^- \vec{\nabla} n \cdot \frac{\vec{E} \times \vec{B}_o}{B_o} - \mu_p^- \vec{\nabla} \cdot (n\vec{E})$$

$$= - \frac{\gamma + 1}{eh} j_h - \frac{1}{eh} j_c - \alpha(n^2 - n_o^2) \qquad (3.4)$$

$$\frac{\partial n}{\partial t} + \mu_H^+ \vec{\nabla} n \cdot \frac{\vec{E} \times \vec{B}_o}{B_o} + \mu_p^+ \vec{\nabla} \cdot (n\vec{E})$$

$$= - \frac{\gamma}{eh} j_h - \alpha(n^2 - n_o^2) \qquad (3.5)$$

In order to remove the term $n\vec{\nabla}\cdot\vec{E}$ arising from the charge separation we multiply (3.4) and (3.5) by μ_p^+ and μ_p^-, respectively, and add the resulting equations to obtain

$$\frac{\partial n}{\partial t} + \frac{\mu_p^+ \mu_H^- + \mu_p^- \mu_H^+}{\mu_p^+ + \mu_p^-} \vec{\nabla} n \cdot \frac{\vec{E} \times \vec{B}_o}{B_o}$$

$$= - \frac{\gamma}{eh} j_h - \frac{1}{eh} \frac{\mu_p^+}{\mu_p^+ + \mu_p^-} j_\parallel - \alpha(n^2 - n_o^2) \qquad (3.6)$$

where $j_\parallel = j_\parallel^- = j_c + j_h$. In the ionospheric region of interest (100 - 150 km)

we can well approximate

$$\frac{\mu_p^+ \mu_H^- + \mu_p^- \mu_H^+}{\mu_p^+ + \mu_p^-} \cong \mu_H^- \cong B_o^{-1}$$

$$\frac{\mu_p^+}{\mu_p^+ + \mu_p^-} \cong 1$$

Thus (3.6) is further reduced to

$$\frac{\partial n}{\partial t} + \frac{\vec{E} \times \vec{B}_o}{B_o^2} \cdot \vec{\nabla} n = -\frac{\gamma}{eh} j_h - \frac{1}{eh} j_{\parallel} - \alpha(n^2 - n_o^2) \tag{3.7}$$

This governs the time development of the ionospheric plasma density.

Next, from the quasi-neutrality condition the current continuity equation at the ionospheric height becomes

$$\vec{\nabla}_\perp \cdot \vec{j}_\perp = \frac{j_{\parallel}}{h} \tag{3.8}$$

where $\vec{j}_\perp = ne(\vec{V}^+ - \vec{V}^-)$ can be written from (3.1) as

$$\vec{j}_\perp = -neM_H \frac{\vec{E} \times \vec{B}_o}{B_o} + neM_p \vec{E} \tag{3.9}$$

where $M_H = \mu_H^- - \mu_H^+ \cong \mu_H^- \cong B_o^{-1}$ and $M_p = \mu_p^+ + \mu_p^- \cong \mu_p^+$. If we substitute the ionospheric electric field $\vec{E}$, which is derived from the electrostatic potential ϕ as

$$\vec{E} = -\vec{\nabla}_\perp \phi \tag{3.10}$$

into (3.9), (3.8) becomes an elliptic partial differential equation to

determine ϕ.

In order to close the chain of the feedback, required is another important relationship, which connects the induced potential $\tilde{\phi}$ to the induced field-aligned current $\tilde{j}_{\parallel}$ at 110 km height, where the tilde denotes the time dependent component. To express this relationship generally, we introduce a magnetospheric impedance Z that determines $\tilde{j}_{\parallel}$ once $\tilde{\phi}$ is determined in the ionosphere:

$$\tilde{j}_{\parallel} = Z^{-1}\nabla^2\tilde{\phi} \tag{3.11}$$

where it should be remarked that Z generally includes differential and/or integration operators with respect to t. A specific form of Z depends naturally on the magnetohydrodynamic property of the magnetospheric plasma.

III-5 Stability analysis

In this section we shall seek a linear unstable solution of (3.7) - (3.11), which would eventually develop into an arclike solution[Sato, 1978].

We use a coordinate system, in which the positive x axis is directed northward, the positive y axis toward the east, and the positive z axis downward (parallel to the magnetic field). Assume that there are unperturbed electric fields E_{xo} and E_{yo} in the rest frame of the neutral ionosphere. Then the field lines are convected in the x direction with the electric drift, namely E_{yo}/B_o. We rewrite a closed set of governing equations (3.7) - (3.11) in the reference frame moving with this electric drift in the x direction. Assuming that the perturbation is uniform in the y direction, i.e., $\partial/\partial y = 0$, (3.7) - (3.11) becomes in this reference frame

$$\frac{\partial n}{\partial t} = - \frac{\gamma}{eh} j_h - \frac{1}{eh} j_{\parallel} - \alpha(n^2 - n_o^2) \tag{3.12}$$

$$\frac{\partial j_x}{\partial x} = \frac{j_{\parallel}}{h} \tag{3.13}$$

$$j_x = M_p en(E_{xo} + E_x) - M_H enE_{yo} \tag{3.14}$$

$$\tilde{j}_{\parallel} = Z^{-1} \frac{\partial^2}{\partial x^2} \tilde{\phi} \tag{3.15}$$

where E_x is the perturbation electric field associated with the density perturbation. Since the effect of precipitation of hot electrons is to accelerate an instability, it is sufficient for the stability analysis to examine the case in which the field-aligned current is carried by cold electrons. Therefore we put $j_h = 0$ in (3.12). If we linearize

(3.12) - (3.15) on the assumption that all the perturbations take the form of $\exp(i\omega t - ikx)$, we obtain the dispersion relation:

$$\omega = i2\alpha n_o + k(M_p E_{xo} - M_H E_{yo}) \frac{1}{1 + Z/R} \tag{3.16}$$

where $R = (heM_p n_o)^{-1}$. From (3.16) we have

$$\mathrm{Re}(\omega) = k(M_p E_{xo} - M_H E_{yo})/(1 + X^2) \tag{3.17}$$

$$\mathrm{Im}(\omega) = k(M_p E_{xo} - M_H E_{yo})X/(1 + X^2) - 2\alpha n_o \tag{3.18}$$

where $X = \mathrm{Im}(Z)/R$. Since $M_p E_{xo} - M_H E_{yo}$ is proportional to the unperturbed north-south ionospheric current, (3.17) implies that the perturbation moves in the direction of the large-scale north-south current in the reference system moving with the electric drift in the x direciton.

Without loss of generality we are allowed to assign the real frequency $\mathrm{Re}(\omega)$ to be positive and the wave number k to include the sign of the phase velocity, therefore $k(M_p E_{xo} - M_H E_{yo}) > 0$. With this choice of positive sign for $\mathrm{Re}(\omega)$ we can conclude that a necessary condition for the feedback instability is $X > 0$, namely, $\mathrm{Im}(Z) > 0$. This indicates that the magnetospheric impedance Z must be inductive for the feedback instability, being in agreement with the requirement predicted from the physical picture. We shall see in Appendix A that this requirement is also derived from an energy consideration. Another necessary condition for the instability is that $M_p E_{xo} - M_H E_{yo}$, i.e., the unperturbed north-south current must be large enough to overcome the damping.

It is readily seen from (3.18) that the most unstable mode satisfies $Im(Z) = R$. The phase velocity of the most unstable mode is therefore given by

$$V_{ph} = \frac{Re(\omega)}{k} = \frac{1}{2}(M_p E_{xo} - M_H E_{yo}) \tag{3.19}$$

For comparison with simulation results in chapter IV, we rewrite V_{ph} in the rest frame of the neutral ionosphere. Using the fact that the frequency in the rest frame of the neutral ionosphere $\omega^{I.S.}$ is Doppler - shifted from ω by $kM_H E_{yo}$, the phase velocity $V_p^{I.S.}$ in the rest frame of the neutral ionosphere becomes

$$V_{ph}^{I.S.} = \frac{Re(\omega^{I.S.})}{k} = \frac{1}{2}(M_p E_{xo} + M_H E_{yo}) \tag{3.20}$$

We shall derive in Appendix A the same dispersion relation as (3.16) based on the concept of Alfven wave reflection at the ionosphere and the energetics of the instability in the ionosphere-magnetosphere coupling system will be discussed in detail.

IV. GLOBAL FORMATION OF AURORAL ARCS

IV-1. Introduction

The principal purpose of this chapter is to extend the feedback theory to a three-dimensionally coupled ionosphere-magnetosphere system and to 'globally simulate' the development of quiet auroral arcs. The numerical simulation is performed in a simple but realistic model of the auroral oval which includes two pairs of large-scale Birkeland currents, large-scale polar cap electric fields, and a day-night asymmetry of the electron density distribution.

A key to the present numerical simulation is the magnetospheric response to the ionospheric potential disturbance. Since the way of 3-dimensional MHD coupling between the ionosphere and the magnetosphere, hence the resulting auroral structure, depends essentially on the magnetospheric impedance Z, Z must be fomulated so as to satisfy the following requirements: It must be able to simulate the inhomogeneous character of the auroral region ionosphere and be able to describe both the inductive and capacitive property of the Alfvén wave in the magnetosphere. Furthermore, the simulation model must include a realistic model of the precipitation of auroral electrons responsible for the visual auroral forms and a strong ionospheric density enhancement.

In IV-2 a response equation is derived on the basis of the ideal magnetohydrodynamic equations. Then, a model of the precipitation of auroral electrons is specified in the first half of IV-3. The latter half of IV-3 is devoted to constructing a realistic model of the auroral oval based on the extensive observational results. Simulation results are

given for a number of ionospheric and magnetospheric parameters in IV-4. The detail of the numerical procedure relevant to the present simulation is given in Appendices B and C.

IV-2. A lumped constant circuit description of the magnetosphere

We have seen in the previous chater that a key to understanding the ionosphere-magnetosphere coupling is to specify properly the magnetospheric impedance Z, which describes the response of the magnetosphere to the ionospheric disturbance. Since this thesis concerns principally the effects of the magnetohydrodynamic coupling between the ionosphere and the magnetosphere on the ionospheric disturbances, we approximate the passive magnetosphere by a lumped constant circuit with two reactive elements. Although the detail of the amplitude and phase distribution of the MHD wave along the field line is sacrificed by this lumped constant circuit analysis, this treatment reduces greatly the machine time and the memory storage for the numerical computation. We shall see later that lumped constants derived still preserve the essence of the three-dimensional ionosphere-magnetosphere coupling in the low frequency range via Alfvén wave. The circuit analysis of the passive magnetosphere was tried elsewhere [Dewitt, 1968; Sato and Holzer, 1973 for lumped circuit; Sato, 1978 for distributed circuit]. In what follows a response function Z of the magnetosphere is derived based on the ideal MHD equation.

We start with the linearized ideal MHD equations which are written in the reference frame fixed to the field lines:

$$\vec{\nabla} \times \vec{B} = \mu_o \vec{j} \tag{4.1}$$

$$\vec{\nabla} \times \vec{E} = - \frac{\partial \tilde{\vec{B}}}{\partial t} \tag{4.2}$$

$$\rho_o \frac{\partial \tilde{\vec{v}}}{\partial t} = \tilde{\vec{j}} \times \vec{B}_o \tag{4.3}$$

$$\tilde{\vec{E}} + \tilde{\vec{v}} \times \vec{B}_o = 0 \tag{4.4}$$

where the tilde and the suffix o denote the perturbation term and the unperturbed term, respectively, and the incompressibility (i.e., $\tilde{\rho} = 0$) is automatically satisfied. Taking the curl of (4.2) and using (4.1) yield

$$\vec{\nabla}(\vec{\nabla} \cdot \tilde{\vec{E}}) - \vec{\nabla}^2 \tilde{\vec{E}} = -\mu_o \frac{\partial \tilde{\vec{j}}}{\partial t} \tag{4.5}$$

Under the assumption of $\sigma_{\parallel} = \infty$, i.e., $\tilde{E}_{\parallel} = 0$ (equivalent to (4.4)), the parallel component of (4.5) is given by

$$\frac{\partial}{\partial s} (\vec{\nabla}_{\perp} \cdot \tilde{\vec{E}}_{\perp}) = \mu_o \frac{\partial \tilde{j}_{\parallel}}{\partial t} \tag{4.6}$$

where s is a coordinate variable along the field line and we have defined $\tilde{j}_{\parallel} > 0$ for the current flowing in the negative s direction. This gives a relationship between the charge density and the induced field-aligned current density.

Let us turn our attention to the component perpendicular to the magnetic field. The polarization current across the field line (derived from (4.3) and (4.4)) is expressed as

$$\tilde{\vec{j}}_{\perp} = \frac{\rho_o}{B_o^2} \frac{\partial \tilde{\vec{E}}_{\perp}}{\partial t} \tag{4.7}$$

If ρ_o is independent of the coordinate perpendicular to the magnetic field, taking div of (4.7) yields

$$\frac{\rho_o}{B_o^2} \frac{\partial}{\partial t} (\vec{\nabla}_{\perp} \cdot \tilde{\vec{E}}_{\perp}) = \vec{\nabla}_{\perp} \cdot \tilde{\vec{j}}_{\perp} = B_o \frac{\partial}{\partial s} \left(\frac{\tilde{j}_{\parallel}}{B_o} \right) \tag{4.8}$$

where used is the three-dimensional current continuity equation derived by taking div of (4.1). Thus we have arrived at the wave equations (4.6) and (4.8) that can describe the field-aligned magnetohydrodynamic coupling. The wave equations are familiar in the transmission line analysis and are easily solved in the steady state ($\partial/\partial t = i\omega$) by imposing a proper boundary condition along the field line.

We define a coordinate along the field line in such a way that $s = 0$ and $s = \ell$ correspond to the foot of the field line (ionosphere) and the equator, respectively. Since we are interested in obtaining a lumped constant circuit representation of the magnetospheric plasma, we assume that B_o and ρ_o are uniform and equal to their average values along the field line and we neglect a curvature of the field line. Then taking $\partial/\partial s$ of (4.8) and using (4.6), we obtain

$$\frac{\partial^2 \tilde{j}_{\parallel}}{\partial s^2} = - \frac{\omega^2}{V_A^2} \tilde{j}_{\parallel} \tag{4.9}$$

Thus $\tilde{j}_{\parallel}$ is generally expressed as

$$\tilde{j}_{\parallel} = A \cos \left(\frac{\omega}{V_A} s \right) + B \sin \left(\frac{\omega}{V_A} s \right) \tag{4.10}$$

where A and B are constants, which should be determined by a proper boundary condition. Substituting (4.10) into (4.8) yields

$$\vec{\nabla}_{\perp} \cdot \tilde{\vec{E}}_{\perp} = i\mu_o V_A \left[A \sin \left(\frac{\omega}{V_A} s \right) + B \cos \left(\frac{\omega}{V_A} s \right) \right] \tag{4.11}$$

If we assume that the two hemispheres are symmetrically conjugate with respect to equatorial plane, hence $\tilde{j}_{\parallel} = 0$ at $s = \ell$, we obtain from (4.10)

$$\frac{B}{A} = -\cot\left(\omega \frac{\ell}{V_A}\right) \tag{4.12}$$

This is enough to specify the impedance along the field line as

$$\frac{\vec{\nabla}_\perp \cdot \tilde{\vec{E}}_\perp}{\tilde{j}_\parallel} = i\mu_o V_A \cot\left[\frac{\omega}{V_A}(\ell - s)\right] \tag{4.13}$$

Therefore the magnetospheric impedance seen from the ionosphere (s = 0) becomes

$$\frac{\vec{\nabla}_\perp \cdot \tilde{\vec{E}}_\perp}{\tilde{j}_\parallel^{I.S.}} = i\mu_o V_A \cot\left(\omega \frac{\ell}{V_A}\right) \tag{4.14}$$

As is readily seen on the right hand side of (4.14), the response equation gives multiple resonances at

$$\omega = \frac{V_A}{\ell} n\pi \quad (n = 1, 2, 3, \cdots\cdots\cdots) \tag{4.15}$$

Since we are interested only in the low frequency regime describing a resonance of the Alfvén wave with the longest wave length along the field line, we retain only the lowest frequency in (4.15). We expand the right hand side of (4.14) around $\omega = \pi V_A/\ell$, using an identity

$$\cot x \approx \frac{2}{x - \frac{\pi^2}{x}} \quad (x \sim \pi) \tag{4.16}$$

to obtain

$$-i\omega \frac{2\mu_o \ell}{\pi^2} \tilde{j}_\parallel^{I.S.} = \left[\left(i\omega \frac{\ell}{\pi V_A}\right)^2 + 1\right] \vec{\nabla}_\perp \cdot \tilde{\vec{E}}_\perp^{I.S.} \tag{4.17}$$

This implies that the magnetosphere can be represented by a parallel circuit of an inductance $2\mu_o \ell/\pi^2$ and a capacitance $\ell/(2\mu_o V_A^2)$, in the frequency regime that we are concerned with. Using these lumped constants we can express the response equation describing the relationship between $\tilde{\phi}^{I.S.}$ and $\tilde{j}_{\parallel}^{I.S.}$ as

$$\frac{2\mu_o \ell}{\pi^2} \frac{\partial \tilde{j}_{\parallel}^{I.S.}}{\partial t} = \left[\left(\frac{\ell}{\pi V_A} \right)^2 \frac{\partial^2}{\partial t^2} + 1 \right] \nabla_{\perp}^2 \tilde{\phi}^{I.S.} \tag{4.18}$$

where we have assumed that the electric field component perpendicular to the magnetic field is electrostatic, i.e., $\vec{E}_{\perp} = -\vec{\nabla}_{\perp}\tilde{\phi}$, since we are interested in a low frequency perturbation with $|\omega/k_{\perp}| << V_A$ [Rudakov and Sagdeev, 1961].

Let us discuss the physical property of (4.18). Linearizing (4.18) on the assumption that the perturbation takes the form of $\exp(i\omega t - ikx)$, where x is a coordinate in the direction of the wave vector, shows that the response property of the magnetosphere changes greatly depending on whether $(\ell\omega/\pi V_A)^2 \lessgtr 1$. That is, if $\omega^2 << (\pi V_A/\ell)^2$, the left hand side of (4.18) balances with the second term on the right hand side and we obtain

$$\tilde{j}_{\parallel}^{I.S.} = i \frac{1}{\omega} \frac{\pi^2}{2\mu_o \ell} k^2 \tilde{\phi}^{I.S.} \tag{4.19}$$

This means that the negative field-aligned currens, namely the precipitation of electrons ($\tilde{j}_{\parallel} < 0$), lags $\pi/2$ in phase behind the positive potential perturbation. This phase relationship is in favor of the instability condition as we have seen in Figure 7. It should be noted that (4.19) implies that the closure current in the magnetosphere is substantially induction current flowing along the field line.

On the other hand, if $\omega^2 >> (\pi V_A/\ell)^2$, the left of (4.18) balances with the first term on the right. Therefore the response becomes

$$\tilde{j}_{\parallel}^{I.S.} = -i\omega \frac{\ell}{2\mu_o V_A^2} k^2 \tilde{\phi}^{I.S.} \tag{4.20}$$

Note the appearance of (-i) instead of i in (4.20), which means that the electron precipitation leads the positive potential perturbation $\pi/2$ in phase. In this case the closure current in the magnetosphere is substantially polarization current flowing across the field line. As we have seen in Figure 7, this phase relationship acts to damp an original density perturbation.

From the above physical consideration we expect that the feedback instability occurs for a perturbation with a frequency (in the reference frame of the magnetosphere)

$$\omega \lesssim \frac{\pi V_A}{\ell} \tag{4.21}$$

In other words, the unstable perturbation has a strong cutoff in a frequency regime

$$\omega \gtrsim \frac{\pi V_A}{\ell} \tag{4.22}$$

Since $\omega \propto k$ from (3.17), this means that only a perturbation with a wavelength larger than some cutoff value grows with time in the coupled system.

IV-3. Numerical models and procedures

In this section we shall construct a model for the numerical simulation of the global formation of auroral arcs. We discuss at first a model of the precipitation of auroral electrons, since the present simulation cannot clarify self-consistently the microscopic process responsible for precipitation of auroral electrons. As we have reviewed in III-2, many authors have suggested that current driven instability at the topside ionosphere is a key to the formation of auroral electrons [e.g., Swift, 1965; Kindel and Kennel, 1971]. In order to include the physics in the last paragraph of III-2, therefore, we assume that precipitation of auroral electrons begins once the field-aligned current exceeds some critical value j_{cr}, where j_{cr} is the critical value of the upward field-aligned current at 110 km height for current driven instability at the topside ionosphere. We employ a mathematical model of the ion pair production ratio $\gamma(j_{\parallel})$ such as

$$\gamma(j_{\parallel}) = \frac{1}{2}\gamma_o[-\tanh\left(\frac{j_{\parallel} - j_{cr}}{\Delta j}\right) + 1] \qquad (4.23)$$

where Δj is taken much smaller than $|j_{cr}|$. Furthermore, we assume that the upward perturbed field-aligned current ($\delta j_{\parallel} < 0$) is carried by hot electrons, i.e., $j_h = \delta j_{\parallel}$ for $\delta j_{\parallel} < 0$. It is evidently seen from the above expression that $\gamma(j_{\parallel})$ becomes nearly γ_o once the upward field-aligned current density exceeds the critical value j_{cr}. As we have seen in III-2, Kindel and Kennel [1971] have calculated a critical value of downward electron flux at the ionospheric height from critical electron drift speed at the topside ionosphere assuming the flux conservation along a flux tube. Therefore, following their results (Figure 6), we adopt

$$j_{cr} = -1.5 \ \mu A/m^2$$

in the numerical simulation.

Next, as we have seen in the previous section, the conjugate passive magnetosphere can be represented by a parallel circuit of an inductance $2\mu_o \ell/\pi^2$ and a capacitance $\ell/(2\mu_o V_A^2)$ in the low frequency regime, where ℓ is the field line length from the ionosphere to the magnetospheric equator at auroral latitudes and V_A is the average Alfvén speed along the field line. It is worth noting that the resonance frequency of the circuit is given by $V_A/(2\ell)$, which is equal to the reciprocal of the bounce time of Alfvén wave in the ionosphere-magnetosphere coupled system. In the reference frame fixed to the neutral ionosphere the response equation (4.18) must be written as

$$\left(\frac{2\mu_o \ell}{\pi^2} \right) \frac{d\tilde{j}_{\parallel}}{dt} = \left[\left(\frac{\ell}{\pi V_A} \right)^2 \frac{d^2}{dt^2} + 1 \right] \nabla_{\perp}^2 \tilde{\phi} \qquad (4.24)$$

where the convective derivative is written as

$$\frac{d}{dt} = \frac{\partial}{\partial t} + \vec{V} \cdot \vec{\nabla}$$

As was mentioned previously, the first term and the second term on the R.H.S. of (4.24) are ascribable to the polarization current across the magnetic field and the induction current along the field line, respectively. Since the response relation (4.18) is written in the reference frame co-moving with the field lines, we must use the drift velocity $\vec{E} \times \vec{B}/B_o^2$ in the velocity of the convective term $(\vec{V} \cdot \vec{\nabla})$.

We summarize here the basic equations for the numerical simulation:

Continuity of plasma

$$\frac{\partial n}{\partial t} + \frac{\vec{E} \times \vec{B}_o}{B_o^2} \cdot \vec{\nabla} n = - \frac{\gamma(j_{||})}{eh} j_h - \frac{1}{eh} j_{||} - \alpha(n^2 - n_o^2) \qquad (3.7)$$

where

$$\vec{E} = - \vec{\nabla}_\perp \phi \qquad (3.10)$$

$$\gamma(j_{||}) = \frac{1}{2} \gamma_o [-\tanh (\frac{j_{||} - j_{cr}}{\Delta j}) + 1] \qquad (4.23)$$

Continuity of current

$$\vec{\nabla}_\perp \cdot \vec{j}_\perp = \frac{j_{||}}{h} \qquad (3.8)$$

where

$$\vec{j}_\perp = -neM_H \frac{\vec{E} \times \vec{B}_o}{B_o} + neM_p \vec{E} \qquad (3.9)$$

Response equation

$$(\frac{2\mu_o \ell}{\pi^2}) \frac{d\tilde{j}_{||}}{dt} = [(\frac{\ell}{\pi V_A^2})^2 \frac{d^2}{dt^2} + 1] \nabla_\perp^2 \tilde{\phi} \qquad (4.24)$$

A closed set of above equations can be numerically simulated in the rest frame fixed to the neutral ionosphere if the unperturbed state of the ionosphere is specified. Since the development of auroral arcs is expected to depend importantly on the model of the auroral region ionosphere that we choose, it is required to choose as

realistic a model as possible. Therefore, we construct a numerical model of the auroral oval (in northern hemisphere) based on extensive observational results that we have reviewd in Chapter II.

Let us define a polar coordinate system described by θ, ψ and r, where θ and ψ denote a colatitude angle (in radian) and a longitudinal angle (in radian), respectively; $\psi = 0$ at noon and $\psi = \pi/2$ at 18:00 LT. The radius r is taken to be constant in our model and equal to the sum of R_E and the height of the E layer, where R_E is the radius of the earth.

On the basis of the forementioned statistical study of the auroral zone by Feldstein [1966], we simply assume that the auroral oval is a circular belt bounded at geomagnetic latitudes 67° and 70° as shown in Figure 2. For simplicity, we further assume that the ambient magnetic field is vertical to the ionosphere and the field-line length is constant within the oval considered. We take $B_o = 0.5$ G and hence the Hall mobility M_H is given by

$$M_H = 2 \times 10^4 m^2 sec^{-1} V^{-1}.$$

Following the observations of Brekke et al. [1974], we put $M_H/M_P = 2$, thus

$$M_P = 10^4 m^2 sec^{-1} V^{-1}$$

The electron density in the auroral region ionosphere varies considerably from condition to condition [Ogawa et al., 1978]. In order to model the large dependence of the density both on the local time and the magnetospheric condition, we assume the following unperturbed electron density distribution described by two variable parameters, namely, the noon density (N_{noon}) and the midnight density ($N_{midnight}$):

$$N_o(\theta,\psi) = N_{midnight} + \frac{1}{2}(N_{noon} - N_{midnight}) \times$$

$$[1 + \tanh\left(\frac{6|\pi - \psi|}{\pi} + 3\right)] \qquad (4.25)$$

We hereafter express the density model symbolically by $N_o = N_{midnight} - N_{noon}$.

On the basis of observed high latitude field-aligned currents [Iijima and Potemra, 1976 b] we employ a simple model of large-scale unperturbed field-aligned current distribution such that

$$J_{\parallel o}(\theta,\psi) = -J_{max}\sin\psi\cos\left[\frac{\theta - \theta_{min}}{\theta_{max} - \theta_{min}}\pi\right] \qquad (4.26)$$

where θ_{min} and θ_{max} are 20° and 23° (in degree), respectively, and J_{max} = 1 $\mu A/m^2$. Remember that we have chosen the sign of the current in such a way that the positive current represents the downward current. The Birkeland current distribution (4.26), schematically shown in Figure 8, is a rather bold simplification of the actual distribution; nevertheless, the simplified model would sufficiently preserve the essential features of the high latitude current system. It is further assumed that the unperturbed field-aligned current is carried by cold electrons, hence, there is no aurora in the unperturbed state.

We are now able to obtain the unperturbed electric field and the horizontal current in the auroral oval by solving the time independent differential equation (3.8), which, after substituting (3.9) and (3.10) into (3.8), takes the form of an elliptic partial differential equation for ϕ_o. This equation can be solved numerically by ADI (Alternating-Direction-Implicit) method under an appropriate boundary condition using

a 100 × 72 mesh system (100 for the latitudinal direction and 72 for the longitudinal direction). At the poleward current region, the observational results indicate that the maximum current region is roughly coincident with the foci of the S_q^p current system, namely the foci of the magnetospheric potential generator [Iijima and Potemra, 1976 a]. Therefore it may be a resonable assumption to specify a constant potential distribution at the poleward (polar cap) boundary of the auroral oval:

$$\phi_o(\theta_{min},\psi) = -0.5\ V_o \sin\psi \tag{4.27}$$

where V_o gives a total potential difference across the polar cap. According to the formentioned empirical relation between ΔV and K_p [Heppner, 1977] we adopt V_o = 50 kV in the actual numerical model. At the equatorward boundary of the oval without having such a clear physical meaning as the poleward boundary, we assume that the current across the equatorward boundary is zero and hence the horizontal current diverts along the field line. Hence we can put

$$j_\theta(\theta_{max},\psi)h = J_{\parallel o}(\theta_{max},\psi)\Delta \tag{4.28}$$

at $\theta = \theta_{max}$ where $j_\theta(\theta,\psi)$ is a latitudinal component of the horizontal current density and Δ is given in Table 1. Under the boundary conditions (4.27) and (4.28) and the periodic boundary condition imposed in the longitudinal direction, we can solve the current continuity equation (3.8) to get the unperturbed potential distribution $\phi_o(\theta,\psi)$.

Let us briefly discuss the numerical procedure for solving the temporal evolution of the whole oval system. The detail of the numerical procedures

are explained in Appendix B. In the actual calculation we use time T normalized by T_o, which corresponds to 20.2 sec. At T = 0, a small density perturbation, $\tilde{n}(\theta, \psi, T = 0)$, where the tilde denotes the time dependent term, is arbitrarily imposed upon the unperturbed density N_o. We assume without any loss of generality that an initial field-aligned current perturbation is zero. As a function of θ and ψ, $\tilde{n}(\theta, \psi, T = 0)$ is taken as

$$\tilde{n}(\theta, \psi, T = 0) = 0.05\, N_{midnight} \exp\left[- \frac{(\theta - \bar{\theta})^2}{2(\Delta\theta)^2} \right] \qquad (4.29)$$

where $\bar{\theta} = 21.5°$ and $\Delta\theta = 0.03$. The potential perturbation, $\tilde{\phi}(\theta, \psi, T = 0)$, associated with the density perturbation is then calculated from (3.8). Starting from these initial perturbations, the density at the next time step is calculated from (3.7) and then the field-aligned current is calculated from (4.24). The disturbances thus obtained then determine the potential disturbance at the same time step by (3.8). The elliptic differential equation (3.8) is solved numerically by the ADI scheme at each time step. In order to prevent a spurious numerical dispersion in integrating (3.7) and (4.24), an upstream-downstream difference scheme [Byers and Killeen, 1970] was employed. We give in Table 1 the value of any constant used in the present numerical simulation.

IV-4. Numerical Results and Their Physical Interpretation

Numerical simulations are performed for several ionospheric and magnetospheric parameters as tabulated in Table 3.

IV-4-1. Unperturbed states

Investigated in this subsection is the effect of the ionospheric electron density distribution on the global pattern of the unperturbed electric field and current.

We start with an electron density model of $N_o = 4 \times 10^{10} - 4 \times 10^{11} m^{-3}$. The upper two panels of Figure 9 show the ambient current (left panel) and the ambient electric ($\vec{E} \times \vec{B}$) drift (right panel) calculated for the model specified by (4.25) and (4.26). The electric drift is sunward along the oval; in other words the electric field is predominantly northward on the duskside and southward on the dawnside in good agreement with the observational results of Banks et al. [1973] and Horwitz et al. [1978]. The unit vector shown in the bottom part of the polar plot represents the electric drift of 4000 m/s, which corresponds to the electric field strength of 200 mV/m. The north-south electric field is maximized in the high latitude part on the duskside and reaches 107 mV/m. The east-west component of the electric field is directed from dawn to dusk in both day and night sectors and its peak value is 11 mV/m. This is consistent with the observation by Heppner [1972]. The left panel shows that the horizontal current is predominantly northeastward on the duskside and southwestward on the dawnside. The unit vector shown below represents the height integrated ionospheric current intensity of 1 A/m. The longitudinal component of the current, which is at almost all local

times nearly antiparallel to the direction of the electric drift, is primarily the electron Hall current driven by the large north-south electric field. The latitudinal current, on the other hand, turns out to be the ionospheric closure current of the large-scale Birkeland current shown in Figure 8. The closure current is carried mainly by the ion Pedersen current.

The lower two panels of Figure 9 show the ionospheric current (left panel) and the $\vec{E} \times \vec{B}$ drift (right panel) for a different ionospheric electron density model. In this model, the ambient electron density is smaller by 4 times than the previous model at all local times and all latitudes. The directions of the horizontal current and the electric field agree with those for the previous ionospheric model shown in the upper panels; however, some remarkable differences exist between the two models. First, as is shown in the bottom right panel, the electric drift is much larger than the previous model, and the maximum electric field reaches 138 mV/m. This intensification of the electric field for the smaller electron density model may be interpreted as follows: In our model, the ambient field-aligned current source is present in the magnetosphere independently of the ionospheric condition. Consequently, the latitudinal electric field responsible for the Pedersen current closing the ambient field-aligned current must be intensified when the ionospheric density, hence the Pedersen conductivity, is reduced. In contrast to this considerable change of the north-south electric field, the east-west electric field, especially its maximum value, remains nearly the same as that in the previous model; this indicates that the east-west electric field is almost independent of the field-aligned current intensity and the electron density distribution but is governed by the potential distribution given at the poleward boundary. Second, the lower left panel shows that the

current intensity becomes about 3 times smaller than that of the previous model. Furthermore, a more important change occurs in the current distribution; the current is more intense on the duskside than on the dawnside as is seen in the upper left panel, whereas any remarkable dawn-dusk asymmetry is not seen in the lower left panel. This dawn-dusk asymmetry in the current intensity in the upper left panel has a strong influence upon the global occurence of auroral arcs, as will be seen later. We note that the current direction changes along the midnight meridian from the east at low latitudes to the west at high latitudes which may be ascribed to the Harang discontinuity.

IV-4-2. Dynamic evolution of auroral arcs

Let us now examine how and where a broad, small-amplitude density disturbance given initially at the central latitude of the oval develops with time for the case of the unperturbed model given in the upper panels of Figure 9.

Figure 10 shows the temporal evolution of the peak amplitudes of the density (solid line), the field-aligned current (dotted line), and the potential (dot-dash) disturbances, for the magnetospheric parameter of $\ell = 10.6\ R_E$ (equal to the field line length of the dipole magnetic field at INV = 70°) and $V_A = 2000$ km sec. Since time is normalized by 20.2 sec, the temporal evolution in this figure convers the period of about 11 minutes. During the initial phase the density tends to decay with the recombination damping rate. In about 2 minutes, however, the disturbance starts to grow gradually. The initial damping implies that the arbitrarily imposed initial density disturbance could not meet the linear instability condition ; the gradual growth thereafter indicates that a perturbation of a spatial scale that has the maximum growth rate has grown, while other spatial components that cannot meet the instability condition have decayed. About 7 minutes later, as the maximum field-aligned current reaches the critical current which is chosen to be 1.5 $\mu A/m^2$, the density disturbance begins to grow rapidly owing to the precipitation of auroral electrons ($j_h \neq 0$). At the time corresponding to this sudden increase in the density disturbance, both the field-aligned current and potential disturbances begin to increase faster than the previous phase. The disturbances tend to saturate in the final portion of the simulation, when the peak density reaches as high as $3 \times 10^{11} m^{-3}$. Correspondingly, the peak of the induced field-aligned current at 110 km height reaches about

20 $\mu A/m^2$, and the induced potential attains about 150 V. The dashed horizontal line in this figure represents a saturation amplitude of the density disturbance $\tilde{n}_{sat}(>>n_o)$ evaluated by $\gamma_{gr}\tilde{n}_{sat} = \alpha\tilde{n}^2_{sat}$, where γ_{gr} is a growth rate determined by the slope of the density evolution following the precipitation of hot electrons; as is expected, γ_{gr} is seen to be approximately 10 (equal to the ion pair production rate) times larger than the growth rate in the initial linear stage. A good agreement between this amplitude and the amplitude of $\tilde{n}$ at the final state implies that the nonlinear saturation of the instability can be interpreted by the balance between the instability growth and the nonlinear recombination damping.

Shown in the first row of Figure 11 are the contour plots of the disturbance density normalized by its peak value at three consecutive times in the growing phase. At T = 20, when the precipitation of accelerated electrons does not yet occur, several small-amplitude density striations appear in the night sector. At T = 23 and T = 30, however, two distinct arclike enhancements develop and elongate in the east-west direction on the duskside (note that these contours do not reflect the realistic scale of the auroral arcs). One remarkable fact is that the initial disturbance damps out completely on the dayside and grows only in the nightside sector. This marked difference between the day sector and the night sector, which is also seen in the development of the field-aligned current (middle three panels) and potential (bottom three panels) disturbances, is due to a large difference of the recombination damping rate between the day and the night. Note also a marked contrast in the auroral occurrence between the dawn and the dusk, which can be attributed to the difference in the ambient current distribution shown in the upper left panel of Figure 9.

In Figure 12 (top panels) we show the contours of the intensity of the upward induced field-aligned current that exceeds the critical value j_{cr}. Since the optical aurora results from precipitation of hot (accelerated) electrons, it may be said that these sequential plots reflect the development of optical auroras. At T = 20 no arc is yet formed, since $|j_{\parallel}| < |j_{cr}|$, whereas at T = 25 two clear-cut arcs elongating in the east-west direction appear in the evening sector and develop into a more elongating form ($\sim$1500 km in the east-west direction) at T = 30 with another arc being generated on its poleward side.

Shown in the lower two panels of Figure 12 are the current (left panel) and electric drift (right panel) distributions at T = 30. Here we emphasize that the eastward electrojet is considerably enhanced but the electric drift is considerably reduced inside the auroral arcs. A closer comparison of the current vectors in this sector with the position of arcs in the upper panels discloses that the electrojet intensity inside the arcs becomes much stronger than the ambient component, whereas that between the arcs is substantially reduced from the ambient component. Furthermore, the northward electric field is reduced inside , but it is intensified in between. The reduction of the electric field can be attributed to the polarization field which develops southward inside the arcs in the evening sector and northward in the morning sector, thus reducing the total field. The large enhancement of the inside electrojet can be subject directly to the conductivity enhancement, not to the Cowling effect, since the electric field component along the auroral arcs is much smaller than the perpendicular component in our model (see Figure 9).

Since, as we have seen in Figure 7, the spatial relationship among the density, the field-aligned current and the potential disturbance is crucial for the feedback instability to take place, we shall examine

the relationship in detail in the following.

The left panel of Figure 13 shows the latitudinal profile of the density (solid line) and the potential (dotted line) disturbance at three consecutive times at 2200 LT. At T = 20, when the amplitude of the disturbance still remains small, the potential disturbance associated with the density disturbance has a positive peak on the poleward side and a negative peak on the equatorward side, and it becomes nearly zero at the peak of the density, since the latitudinal current is northward in this local time (see Figure 9). As time goes on, the disturbance drifts northward keeping the same phase relationship. This indicates that the potential disturbance in the ionosphere is primarily caused by the polarization charge associated with the density disturbance, although the field-aligned current acts to some extent to neutralize the polarization charge. At T = 30 a couple of pronounced density spikes are formed as a result of precipitation of hot electrons, the width of the poleward arc being about 18 km. The right panel of this figure shows another important relationship between the density disturbance (solid line) and the induced field-aligned current (dotted line). The negative field-aligned current moves poleward with a phase lag of nearly $\pi/2$ with respect to the positive potential disturbance, as is expected from the physical interpretation of the feedback instability given in Figure 7.

IV-4-3. Dependence of auroral arc development on the ionosphereic electron density distribution

We expect that the ambient electron density distribution would affect the evolution of quiet auroral arcs in two ways: First, the global unperturbed distribution of the ionospheric current, which plays a crucial role in the instability, depends strongly on the ambient electron density distribution. Since the growth rate of auroral arcs increases with J_{NS}/n_o (see (3.16)), the global distribution of auroral arcs is presumed to be greatly affected by the electron density distribution. Second, as the dispersion equation (3.16) says, the major damping mechanism of the instability is the recombination loss in the ionosphere. Judging from the fact that the recombination damping time is a few minutes for a typical ionospheric electron density and is comparable to the growth time, one can understand that the ambient electron density distribution plays an important role in the evolution of auroral arcs.

In order to examine above conjecture numerical simulations were performed for two other models with different ambient electron density distributions, keeping the magnetospheric parameters the same as those in the previous model. Shown first is the result of the case with the electron density model, $N_o = 10^{10} - 10^{11} m^{-3}$, whose ambient solutions were shown in the lower panels of Figure 9. The temporal evolution of the peak values of the density (solid), field-aligned current (dotted), and the potential (dot-dash) disturbances are shown in Figure 14. Comparing this figure with Figure 10, one can see that the growth of the disturbances is much faster than that in Figure 10. Note particularly a much smaller, initial recombination damping, which is attributable to a lower ambient

electron density model. Because of the large growth rate, the peak of the density disturbance reaches as high as $10^{12} m^{-3}$, the peak field-aligned current reaches 200 $\mu A/m^2$, and the potential becomes as high as 450 V. A rapid increase of the density disturbance occurs when the induced field-aligned current reaches the intensity of the order of 1 $\mu A/m^2$. It is interesting to observe that the induced field-aligned current becomes 10 times as large as that in the previous case, while the density and potential amplitudes remain only 3 times larger than those in the previous case. This suggests that the field-aligned current intensity is strongly dependent on the ambient electron density in the ionosphere. The contour plots of hot electron fluxes are shown in the upper three panels of Figure 15. In contrast to the previous result shown in Figure 12, several arcs have developed in the low latitude part of the midnight-morning sector, this indicating that the global occurence of auroral arcs is largely controlled by the ionospheric electron density distribution. The principal reason for this remarkable difference lies in the difference of the global ionospheric current pattern. More specifically, as is seen in the lower left panel of Figure 9, the current distribution in the present case is more symmetric with respect to the noon-midnight meridian than that in the previous case, which is shown in the upper left panel.

The current (left) and electric drift (right) distributions at T = 30 are shown in Figure 15. A remarkable intensification of the electrojet should be noted at the positions of the auroral arcs. In the most developed arc which is located on the duskside, the electrojet intensity becomes as high as about 20 kA. As is seen in Figure 12, the latitudinal electric field is considerably reduced inside the arcs and intensified between them. It is worth while to note that while the hot electron flux

contour appears to exhibit a similar pattern in both the high latitude part on the duskside and the low latitude part on the dawnside, the north-south component of the electric field is more strongly modified by the auroral arc on the duskside than on the dawnside as was the case in Figure 12. Here it should be reminded that because of the unrealistic, skewed polar coordinate system that was adopted, the auroral arcs on the dawnside are too much exaggerated.

Shown in the upper panel of Figure 16 are the latitudinal profiles of the density (solid line) and potential (dotted line) disturbances at 2200 LT at T = 30. The lower panel shows the latitudinal profiles of the density (solid line) and field-aligned current disturbances (dotted line). The intensity of each arc is very much enhanced compared with the previous case (note the difference of the scale), and the instability region is enlarged. Notwithstanding these differences, the arc width is roughly the same.

Temporal evolution of the disturbances for another model of the ambient electron density is shown in Figure 17. In this model the electron density is reduced further from $10^{10}\,m^{-3}$ to $5 \times 10^{9}\,m^{-3}$ at the midnight but it is kept equal to $10^{11}\,m^{-3}$ at the noon, which is the same as the previous one. In this choice of the density distribution the initial recombination damping becomes smaller, but the initial maximum growth rate remains almost unchanged, and hence the saturation amplitudes remain comparable to those in Figure 14. The resemblance of the overall development behavior between this case and the previous case indicates that if the ambient electron density is so low that the linear recombination damping is negligible, the temporal development of auroral arcs becomes almost independent of the ambient electron density.

Shown in Figure 18 are the latitudinal profiles of the density (solid line in both panels), potential (dotted line in the top panel), and field-aligned current (dotted line in the bottom panel) disturbances at 2200LT at T=30. These profiles resemble to those in the previous case (see Figure 16). Because of the small ambient electron density, however, the unstable region slightly expands latitudinally, so that an additional broad, faint arc appears in the polemost region of the arc system.

IV-4-4. Dependence of auroral arc development on magnetospheric conditions

In this subsection it is examined how the magnetosphere, represented by the field line length ℓ and the average Alfvén velocity V_A, affect the evolution of auroral arcs.

Figure 19 shows the temporal evolution of the peak amplitudes of the density, field-aligned current, and potential disturbances for the case in which the field line length ℓ is doubled, i.e., ℓ = 21.2 R_E, V_A = 2000 km/sec, and $N_o = 10^{10} - 10^{11} m^{-3}$. Since the magnetospheric inductance is given by $2\mu_o \ell/\pi^2$, it is expected from the linear analysis that the growth rate of the quiet auroral arc is substantially reduced (compare with Figure 14). Because of the decrease in the linear growth rate the rapid increase in the electron density by precipitation of hot electrons is delayed until about T = 13, although it happened at about T = 6 in Figure 14. The density, the field-aligned current, and the peak potential arrive at $4 \times 10^{11} m^{-3}$, $\sim 20 \mu A/m^2$, and $\sim$300 V, respectively. The field-aligned current is by about 10 times smaller than that in Figure 14, whereas the density and the potential do not differ considerably from those in Figure 14 (at most 2 times). As we have seen in Figure 10, a saturation amplitude of the density disturbance calculated from $\tilde{n}_{sat} = \gamma_{gr}/\alpha$ (dashed line) agrees well with the amplitude at the final state; this indicates that the nonlinear saturation of the instability is caused by the balance between the instability growth and the nonlinear recombination damping.

The contour plots of hot electron fluxes are shown in the upper three panels of Figure 20. It is important to note that although the unstable region remains almost unchanged, the number of arcs therein is decreased, and the arc width and spacing are remarkably broadened. The

lower two panels of Figure 20 show the current (left panel) and electric drift (right panel) distributions at T = 30. The auroral electrojets do not develop so markedly (about 10 kA for the most developed arc) as those seen in Figure 15. Likewise, the reduction and the intensification of the latitudinal electric field associated with the arcs are not so remarkable.

The variation of the arc width and the arc spacing with the change of the field line length can be seen more clearly in Figure 21, which shows the latitudinal profile of the density disturbance (solid line) and the induced field-aligned current (dotted line) at 2200 LT at T = 30. Three distinct arcs are observed, and the width of the most developed arc is about 27 km. Being consistent with the linear theory, the width and spacing of the arcs become broader and the growth rate becomes smaller with the increase in the field line length.

The results for the case in which the Alfvén speed V_A is reduced from 2000 km/s to 1500 km/s are shown in Figures 22 - 24. The other parameters are kept equal to $\ell = 10.6\ R_E$ and $N_o = 10^{10} - 10^{11} m^{-3}$. In Figure 22 we show the temporal evolution of the density, field-aligned current and potential disturbances. Since the magnetospheric capacitance is given by $\ell/2\mu_o V_A^2$, the capacitance in this case is approximately twice as large as that of the case shown in Figure 14. Although the overall evolution process is similar to that in Figure 14, the developing speed is somewhat slower and the peak field-aligned current is $\sim$80 $\mu A/m^2$, which is considerably smaller than $\sim$200 $\mu A/m^2$ in the previous case.

The contour plots of hot electron fluxes are shown in the upper three panels of Figure 23. In the lower two panels of Figure 23 we show currents (left panel) and electric drifts (right panel) at T = 30.

The overall pattern is very similar to that in Figure 15.

Figure 24 shows latitudinal profile of the density (solid line) and field-aligned current (dotted line) disturbances at 2200 LT at T = 30. Though not so clear, the arc width becomes slightly broader than that in Figure 16 and the amplitude of the disturbances becomes slightly less than that in Figure 16. It can be said therefore that the decrease in V_A acts to broaden the arc width. From this result, along with the result given in Figure 21, we can conclude that the width and the spacing of the auroral arc in the ionospheric level vary from 10 to 40 km for a reasonable range of the magnetospheric impedance specified by ℓ and V_A. In this respect one should note that the ionospheric ambient electron density plays no significant role in the determination of the width and the spacing of the arcs (cf. Figures 13, 16 and 18), since it does affect the development of auroral arcs primarily through the recombination damping.

V. DISCUSSION

V-1. Comparison of numerical results with observational results

Field-aligned currents and auroral electrojets associated with auroral arcs

The simulation results have shown that the field-aligned current at 110 km height becomes 10 - 200 $\mu A/m^2$ (see Figures 10, 14, 17, 19 and 22) and the intensity of auroral electrojets becomes 5 to 20 kA (see Figures 12, 15, 20 and 23), both depending on the ionospheric electron density distribution and on the magnetospheric impedance. These results are in excellent agreement with many of the experimental facts obtained by Cloutier and his colleagues [Park and Cloutier, 1971; Casserly and Cloutier, 1975; Sesiano and Cloutier, 1976] (see Table 1): A pair of upward and downward field-aligned current with the density of a few to several tens $\mu A/m^2$ develop associated with a quiet auroral arc with 10 to 40 km width and spacing, the upward current being coincident with the visual arc; an auroral electrojet develops associated with an auroral arc, the intensity of which is several to a few tens kA.

Electric field inside auroral arcs

Figures 12, 15, 20 and 23 show that the longitudinal component of the electric drift is considerably reduced inside the auroral arc owing to the development of the polarization field across the arc, which is reverse to the unperturbed electric field. This fact is consistent with the observational result of Aggson [1969], Wescott et al. [1969] and Maynard et al. [1973]. There is an experimental report that indicates no such decrease in the electric field inside the arc [Mozer and Fahleson, 1970; Carlson and Kelley, 1977; Beaujardiere et al., 1977]. This result

apparently disagrees with our simulation result. However, the disagreement can easily be resolved, if we remember the fact that in our model the east-west component of the unperturbed electric field was considerably smaller than the north-south component (see right panels of Figure 9), as was observed by Banks et al. [1973], Horwitz et al. [1978], and Wescott et al. [1969]. According to Mozer [1971], however, the large-scale electric field that is predominantly westward is often observed in the midnight sector prior to substorm onsets. Such an electric field configuration is in favor of the Cowling effect that can induce a strong polarization field across an auroral arc in excess of the unperturbed north-south electric field. Provided the unperturbed electric field along an auroral arc was greater than or comparable with the electric field across the arc during the experiment of Carlson and Kelley [1977] and Beaujardiere et al., [1977], the apparent puzzling observational fact can be reconciled.

Horizontal motion of auroral arcs

Shown in Figure 25 is a dynamic view of the growth of the density disturbance on the duskside [cf. Figure 13]. It is seen that the whole system of the auroral arcs moves poleward with a moderate speed of about 100 m/sec in the early phase and reaches an almost stationary state. Note that the arcs in the dawn sector move equatorward in the early phase as shown in Figures 15, 20 and 23. The arc motion in the early phase should be given by $V_{ph}^{I.S.}(E_q.(3.20))$. Since $|M_P E_{xo}| >> |M_H E_{yo}|$ and E_{xo} is poleward in the evening sector and equatorward in the morning sector, the poleward motion of the arcs in the evening sector and the equatorward motion in the morning sector are a reasonable consequence in our model. Figure 26 shows the latitudinal arc motion at 2200 LT for different ionospheric density distributions (left panel) and for different magnetospheric impedances (right panel). A remarkable fact is that regardless

of the electron density and the magnetospheric impedance, the latitudinal velocity of auroral arcs becomes almost zero in the fully developed state; this fact can be interpreted by the complete reduction of $M_P E_{xo} + M_H E_{yo}$ inside the arc. It is also remarkable that the velocity of the poleward arc motion in the early phase of the evolution (slope of the curve) increases with the growth rate of the auroral arcs (see, Figures 10, 14, 17, 19 and 22).

Effects of the ambient electron density distribution on the development of auroral arcs

Figure 27 shows a three-dimensional view of the density disturbance at T = 30 for two different density models shown in Figure 12 (upper panel) and Figure 15 (lower panel). In contrast with the upper panel corresponding to a denser ionospheric model the lower model shows the formation of far more enhanced multiple density arcs both on the dusk side and on the dawn side. This marked contrast is due to the strong dependence of the arc development on the ambient electron density distribution in the ionosphere. This figure also provides a convincing result that no perturbation develops in the day sector owing to the large recombination damping rate.

The effect of the ambient electron density distribution on the saturation amplitude of the density (cross), field-aligned current (circle), and potential (triangle) disturbances is summarized in Figure 28 (left panel). As can be seen, the field-aligned current intensity depends most strongly on the ambient electron density. As we have already noted in Figure 17, when the ambient electron density becomes so low that the recombination damping term becomes negligible, neither the growth rate nor the saturation amplitude of the disturbances becomes any more dependent on the ambient electron density distribution; this is because

the growth rate is then determined by J_{NS}/n_o and the impedance of the magnetosphere.

Effects of the magnetospheric impedance

The effect of the magnetospheric impedance, which plays a key role in the ionosphere-magnetosphere coupling, is summarized in the right panel of Figure 22. Shown here are the arc width (square) and the peak amplitudes of the density (cross), field-aligned current (circle), and potential (triangle) disturbances at T = 32 as a function of the bounce time of the Alfvén wave given by $4\ell/V_A$; the ambient electron density distribution is the same in these runs (No.3, 4 and 5 in Table 2). Of primary importance in this panel is the linear increase of the arc width with the bounce time, which is attributable to the fact that a disturbance with a latitudinal scale which is nearly resonant with the Alfvén wave with the bounce time of $4\ell/V_A$, grows with the largest growth rate and develops into an auroral arc. Another important fact deduced from the figure is that while the field-aligned current intensity decreases linearly with the bounce time, the potential amplitude remains almost constant irrespective of the magnetospheric impedance; this suggests that the auroral arc acts as a potential generator, the energy of which is continuously supplied by the large-scale ionospheric current flow (see Figures 7 and 13).

Effects of auroral electrojets on the ground magnetic perturbation

The MHD response of the magnetosphere in the present simulation model is too simple to discuss the effect of developed auroral electrojets on the ground magnetic perturbation; however, according to Biot-Savart law, a noticeable magnetic effect is produced on the ground due to the east-west auroral electrojets, which are developed in the present simulation model. The ground magnetic effect is estimated to be several hundred nT (depending, of course, on the current density and latitudinal width of the electrojets) below the center of the electrojet region, so that a moderate magnetic substorm is expected on the ground.

V-2. Global distribution of quiet auroral arcs

The simulation results have shown that the global occurence of auroral arcs has a strong dependence on the background structure of the auroral oval. The following three effects are of particular importance.

First, the relatively large electron density limits auroral arcs from developing in the day sector (recombination damping). Second, auroral arcs appear more intensely on the duskside due to the dawn-dusk asymmetry of the large-scale ionospheric current (Figure 9). The interrelationship between the auroral appearance and the current distribution is self-explanetory, because the linear growth rate γ_{Lin} increases with $|J_{NS}|/n_o$ (E_q.(3.18)) and the saturation amplitude of the disturbance is proportional to γ_{Lin}/α; auroral arcs develop more intensely in the place where $|J_{NS}|$ is large. To summarize, the remarkable dawn-dusk asymmetry of auroral appearance in the upper panel of Figure 27 is interpreted as follows: Given two pairs of large-scale Birkeland currents and the dawn to dusk polar cap electric field, then the closure ionospheric (Pedersen) current of the Birkeland currents becomes northward in the evening sector and southward in the morning sector, whereas the Hall current due to the westward electric field in the dark sector of auroral oval connecting to the polar cap electric field is northward both in the evening and morning sectors. Thus the Pedersen and Hall currents are both northward and add to each other in the evening sector, but they are opposite in the morning sector; thus, a dawn-dusk asymmetry of $|J_{NS}|$ is created.

The third effect is the preferential occurrence of auroral arcs in the region of 'ambient' upward Birkeland current (compare Figures 8 and 27). This may be understood as follows: The linear theory states that auroral

arcs develop while they drift in the north-south direction with the velocity $V_{ph}^{I.S.}$ given by (3.20). In the night sector of the auroral oval except the local time close to the midnight, $|M_P E_{xo}| >> |M_H E_{yo}|$, so that the direction of the drift is the same as that of the closure current of the large-scale Birkeland currents, namely, northward in the evening sector and southward in the morning sector. It is a natural consequence therefore that the auroral arcs develop more actively in the high latitude region of the auroral oval in the evening sector and in the low latitude region in the morning sector, the regions being coincident with the regions of the upward Birkeland current.

VI. SUMMARY AND CONCLUSION

The feedback theory of auroral arcs is extended to a realistic global model of auroral oval, which includes two pairs of large-scale Birkeland currents, polar cap electric field, and a day-night asymmetry of ionospheric electron density distribution. In the first place a quiet background model of auroral oval is constructed, so that it is consistent with the observed distributions of large-scale current and electric field [Banks et al., 1973; Brekke et al., 1974; Horwitz et al., 1978]. Then, a differential equation is derived that describes a three-dimentional magnetohydrodynamic coupling between the ionosphere and magnetosphere in terms of the magnetic field line length (ℓ) and the Alfvén speed (V_A). Combining this equation with the ionospheric equations, numerical simulations have been performed in the initially quiet auroral oval under several ionospheric and magnetospheric conditions.

The simulation results are summarized as follows: A small-scale field-aligned current can grow spontaneously from a small density perturbation that naturally exists in the ionosphere,especially the upward induced current corresponding to an auroral arc. The arc usually appears in multiples in the dark sector of the oval, more preferentially in the evening sector. The latitudinal width and spacing of an arc are 10 to 40 km and the length in the east-west direction is typically 2000 km. The small-scale, localized field-aligned current reaches 10 to 200 $\mu A/m^2$, and the electron density inside each auroral arc reaches $2 \times 10^{11} m^{-3} \sim 10^{12} m^{-3}$. This enormous enhancement in electron density leads to the development of an auroral electrojet in each arc, whose intensity reaches 5 to 20 kA. All of these small-scale features of auroral arcs are found to be in an excellent agreement with

observational results of Cloutier et al. [1973], Park and Cloutier [1971], Casserly and Cloutier [1975] and Sesiano and Cloutier [1976]. Each auroral arc is strongly polarized in the direction of the ambient latitudinal (north-south) current which is primarily carried by the Pedersen current; accordingly, the net electric field perpendicular to the arc is reduced inside the arc, while it is intensified outside, such a tendency being in agreement with results of Aggson [1969], Wescott et al. [1969], and Maynard et al. [1973]. The potential difference across an arc reaches 200 V to 1 kV,nearly independent of the magnetospheric condition. The essence of the whole process occurring in the feedback system may be summarized as follows: Being strongly polarized by the north-south component of the large-scale ionospheric current,the arc becomes a local voltage generator which in turn supplies a local field-aligned current into the magnetosphere. It is obvious that the energy source of the feedback mechanism is the large-scale ionospheric current (electric field), which is governed by the large-scale field-aligned current and the polar cap potential (see Appendix A).

It is found that both the ionospheric and magnetospheric conditions play equally crucial roles in the formation of quiet auroral arcs. Both the developing speed of auroral arcs and the field-aligned current intensity decrease as either the ambient electron density or the bounce time of the Alfvén wave ($4\ell/V_A$) increases. The width and the spacing of auroral arcs increase almost linearly with the increase of the bounce time; this reflects the fact that a perturbation nearly resonant with the Alfvén wave in the magnetosphere can grow into an auroral arc as a result of the three-dimensional ionosphere-magnetosphere feedback coupling.

Several other important results concerning the global distribution of auroral arcs have been found. First, auroral arcs appear only in the

night sector but not in the day sector because of the large recombination loss. Second, auroral arcs tend to appear more intensely on the duskside than on the dawnside. This can be attributed to the dawn-dusk asymmetry of the north-south ionospheric current in the night sector due to the large-scale dawn to dusk electric field. Third, auroral arcs appear predominantly in the region of 'ambient' upward field-aligned current, where the situation is more favorable for the growth of disturbances.

As we have seen in the above, the present numerical simulation is the first in demonstrating successfully the global formation of quiet arcs in the auroral region and the results are consistent with most of the existing observations. This success implies that the magnetohydrodynamic coupling between the ionosphere and the magnetopshere plays an important role in the formation of the so-called quiet auroral arcs, the associated energy being continuously supplied by the large-scale ionospheric current (electric field).

Appendix A. THE ENERGY SOURCE OF THE FEEDBACK INSTABILITY

In the first part of Appendix A, we shall derive the same dispersion equation as that given in III-5, by introducing a concept of the effective reflection coefficient of the Alfvén wave at the ionosphere. In the second part, energetics of instability as a result of the coupling between the ionospheric drift mode and the magnetospheric Alfvén wave will be examined. The instability can be interpreted in terms of the negative dissipation in the ionosphere under the presence of the stationary electric field.

A-1. Wave equations and boundary conditions

Ideal MHD equations (4.1) - (4.4) are solved in an ideal magnetospheric model, where the magnetic field is straight and homogeneous. We employ a coordinate system shown in Figure A.1; the ambient magnetic field is downward in the negative z direction, positive x and y axes direct equatorward and eastward, respectively. Note that this coordinate system is different from that used in III-5. The ionosphere and equator corresponds to $z = 0$ and $z = \ell$, respectively. Since we are interested in an arc-like perturbation which has a much larger extent in the east-west direction than in the north-south direction, we assume the uniform perturbation in the y direction, namely, $\partial/\partial y = 0$. Furthermore, in the following analysis, we treat only the Alfvén wave perturbation with δE_x and δB_y. Although actually the east-west Hall current driven by δE_x gives rise to a generation of the fast mode with δE_y and δB_x components, we neglect this effect. This is justified for the following energy consideration, since the fast mode is evanescent in the vertical direction for $k_\perp >> k_{||}$.

Taking y component of (4.2), δE_x and δB_y are related by

$$\frac{\partial \delta E_x}{\partial z} = - \frac{\partial \delta B_y}{\partial t} \qquad (A.1)$$

The x component of the current density associated with the Alfvén wave is expressed from (4.3) and (4.4) as

$$\delta j_x = \frac{\rho_o}{B_o^2} \frac{\partial \delta E_x}{\partial t} \tag{A.2}$$

If we set this equal to δj_x derived from (4.1) we obtain

$$\frac{\partial \delta B_y}{\partial z} = - \frac{1}{V_A^2} \frac{\partial \delta E_x}{\partial t} \tag{A.3}$$

where V_A is the Alfvén velocity defined by

$$V_A = \frac{B_o}{\sqrt{\mu_o \rho_o}}$$

Let us next consider boundary conditions for δE_x and δB_y, which should be specified at both ionospheres. If we assume that both ionospheres are symmetrically conjugate, a boundary condition at one ionosphere is replaced by the condition $\delta j_z = 0$ at the equator. This condition can be written from (4.1) as

$$\delta B_y = 0 \text{ at } z = \ell \tag{A.4}$$

Another boundary condition at the ionosphere is the jump condition of δB_y by the ionospheric surface current. If we assume $\delta B_y = 0$ just below the E layer and denote the x component of the height-integrated ionospheric current by δJ_x, the jump condition can be written as

$$-\delta B_y(z = 0_+) = \mu_o \delta J_x(z = 0) \tag{A.5}$$

If $\delta J_x(z = 0)$ is expressed by the Alfvén wave quantities at $z = 0_+$ using the continuity of δE_x, (A.4) and (A.5) provide necessary boundary conditions for the guided Alfvén wave described by (A.1) and (A.3).

A-2. Ionospheric equations

In this section we shall consider in detail the contribution of the large-scale dc electric field to the horizontal perturbation current in the ionosphere.

The ionospheric horizontal current density $\vec{j}_\perp$ is expressed as

$$\vec{j}_\perp = -neM_H \frac{\vec{E} \times \vec{B}_o}{B_o} + neM_p \vec{E} \tag{A.6}$$

where $M_H \simeq \mu_H^{-1} \simeq B_o^{-1}$, $M_p \simeq \mu_p^{+}$ and contribution from the neutral wind is ignored in this expression. If we multiply (A.6) by h, the effective height range of the E layer, and linearize it, the height-integrated horizontal current δJ_x can be written as

$$\delta J_x = \Sigma_p \delta E_x + he(M_H E_{yo} + M_p E_{xo})\delta n \tag{A.7}$$

where E_{xo} and E_{yo} are the x-(southward) and the y-(eastward) component of the large-scale dc electric field, respectively. The second term in (A.7) is the perturbation current arising from the density perturbation and the large-scale dc electric field. In order to express δn by the Alfvén wave quantities at $z = 0_+$, we use the continuity equation of the plasma in the ionosphere:

$$\frac{\partial n}{\partial t} + \frac{\vec{E} \times \vec{B}_o}{B_o^2} \cdot \vec{\nabla} n = \frac{j_z}{eh} - \alpha(n^2 - n_o^2) \tag{A.8}$$

where α is the recombination coefficient. In (A.8) we have assumed that the field-aligned current j_z, defined positive for upward current, is carried by cold electrons. Making use of (4.1), δj_z at $z = 0_+$ is related to δB_y at $z = 0_+$ as

$$\delta j_z(Z = 0_+) = - i\frac{k_x \delta By(Z = 0_+)}{\mu_o} \tag{A.9}$$

If we linearize (A.8) on the assumption that all the perturbation in the ionosphere takes the form of $\exp[i(\omega_I t - k_x x)]$ and use (A.9), δn can be expressed by δB_y as

$$\delta n = - \frac{k_x \delta B_y}{\mu_o eh(\omega_I + k_x V_H - i2\alpha n_o)} \tag{A.10}$$

where V_H is the Hall velocity defined by $V_H = E_{yo}/B_o$. Note that ω_I is the frequency of the perturbation seen in the rest frame of the neutral ionosphere. Substitution of (A.10) into (A.7) enables us to express the perturbation current δJ_x by the Alfvén wave quantities above the ionosphere ($z = 0_+$) as

$$\delta J_x = \Sigma_p \delta E_x - \beta \delta B_y/\mu_o \tag{A.11}$$

where β is defined by

$$\beta = \frac{k_x(M_H E_{yo} + M_p E_{xo})}{\omega_I + k_x V_H - i2\alpha n_o}$$

(A.11) can be rewritten by using (A.5) as

$$\delta J_x = \Sigma_p \delta E_x + \beta \delta J_x \tag{A.12}$$

This relation means the existence of an important feedback loop in the ionosphere-magnetosphere coupled system: A perturbation current arising from δE_x generates a perturbation magnetic field δB_y above the ionosphere. The induction current δj_z associated with δB_y in turn

gives rise to a density perturbation in the ionosphere. If the large-scale dc electric field exists in the ionosphere, the density perturbation contributes to the perturbation current, in addition to the original perturbation current $\Sigma_p \delta E_x$. The total surface current δJ_x resulting from this feedback effect is therefore expressed from (A.12) as

$$\delta J_x = \frac{\Sigma_P}{1 - \beta} \delta E_x \tag{A.13}$$

Let us introduce an effective height-integrated Pedersen conductivity of the ionosphere defined by

$$\Sigma_{Peff} = \frac{\Sigma_p}{1 - \beta} = \frac{\omega_I + k_x V_H - i2\alpha n_o}{\omega_I - k_x V_p - i2\alpha n_o} \Sigma_p \tag{A.14}$$

where V_p is the Pedersen velocity defined by $V_p = M_p E_{xo}$. Using Σ_{Peff}, (A.13) is expressed as

$$\delta J_x = \Sigma_{Peff} \delta E_x \tag{A.15}$$

If we use the characteristic impedance of the magnetospheric medium Z_M seen from the ionosphere, which is given by

$$Z_M = - \frac{\mu_o \delta E_x}{\delta B_y} \bigg|_{z = 0} \tag{A.16}$$

the boundary condition at the ionosphere (A.15) can be expressed as

$$Z_M = \Sigma_{Peff}^{-1} \tag{A.17}$$

This relationship exhibits that the impedance of the magnetosphere seen

from the ionosphere matches the effective Pedersen resistivity of the ionosphere.

A-3. Standing Alfvén mode and reflection coefficient at the ionosphere

The guided Alfvén wave in the magnetosphere is reflected, back and forth, between two ionospheres and form a standing Alfvén mode. Thus, δE_x and δB_y associated with the Alfvén wave can be written as [see, for example, Nishida, 1978]

$$\delta E_x = \delta E_{xd}\, e^{i(\omega_M t + k_z z - k_x x)} + \delta E_{xu}\, e^{i(\omega_M t - k_z z - k_x x)} \tag{A.18}$$

$$\delta B_y = \delta B_{yd}\, e^{i(\omega_M t + k_z z - k_x x)} + \delta B_{yu}\, e^{i(\omega_M t - k_z z - k_x x)} \tag{A.19}$$

where the suffixes d and u denote the downward and upward propagating components, respectively, and ω_M is the frequency seen in the rest frame of the magnetosphere, which is equal to $\omega_I + k_x V_H$. In the above expressions we have assumed the perturbation of the sinusoidal form in the x-coordinate over the ionospheric boundary. Amplitudes of the upward and downward propagating components in (A.18) and (A.19) satisfy

$$\delta B_{yd} = -\frac{1}{V_A}\,\delta E_{xd} \tag{A.20}$$

$$\delta B_{yu} = \frac{1}{V_A}\,\delta E_{xu} \tag{A.21}$$

where

$$\frac{\omega_M}{k_z} = V_A$$

Note that k_z is in general complex, since ω_M is a complex quantity.

Once the ratio of δB_{yu} to δB_{yd} is determined, (A.18) and (A.19) can specify the amplitude and phase distributions of the standing Alfvén

mode along the field line. If we express the ratio by Ref, i.e.,

$$\mathrm{Ref} = \frac{\delta B_{yu}}{\delta B_{yd}} \tag{A.22}$$

the magnetospheric impedance seen at the ionosphere Z_M can be written from (A.18) and (A.21) as

$$Z_M = -\left.\frac{\mu_o \delta E_x}{\delta B_y}\right|_{z=0} = \mu_o V_A \frac{1 - \mathrm{Ref}}{1 + \mathrm{Ref}} \tag{A.23}$$

Substituting this into (A.17) and solving for Ref, the boundary (matching) condition at the ionosphere becomes

$$\mathrm{Ref} = -\frac{1 - \mu_o \Sigma_{peff} V_A}{1 + \mu_o \Sigma_{peff} V_A} \tag{A.24}$$

Since this is reduced, in the case of $\vec{E}_o = 0$, to the ordinary reflection coefficient of the Alfvén wave at the ionosphere [see, for example, Tamao, 1964; Hughes and Southwood, 1976]

$$\mathrm{Ref} = -\frac{1 - \mu_o \Sigma_p V_A}{1 + \mu_o \Sigma_p V_A}$$

(A.24) can be interpreted to give the general reflection coefficient of the Alfvén wave at the ionosphere including the feedback effect by the large-scale ionospheric dc electric field.

A-4. Dispersion equation and eigen-values for limited cases

We shall now consider the boundary condition at the equator (A.4), which is required from the assumption of the symmetrically conjugate ionospheres. Substitution of (A.19) into (A.4) yields

$$\mathrm{Ref} = -e^{2ik_z\ell} \tag{A.25}$$

If we substitute this into (A.23), we obtain

$$Z_M = i\mu_o V_A \cot k_z\ell, \tag{A.26}$$

Then, the dispersion equation is obtained from (A.17) as

$$\frac{k_x(M_H E_{yo} + M_p E_{xo})}{\omega_I + k_x V_H - i2\alpha n_o} = 1 - i\mu_o V_A \Sigma_p \cot(k_z\ell) \tag{A.27}$$

Note that this is equivalent to (3.16) derived from (3.7) - (3.11) except the difference of signs introduced by the use of a different coordinate system, since (3.8) and the jump condition (A.5) are equivalent. In terms of the reflection coefficient (A.25), the definite form of the amplitude distributions of the standing Alfvén mode is given from (A.18) and (A.19) as

$$\delta E_x = 2\delta E_{xd} \frac{\cos k_z(z - \ell)}{} e^{i(\omega_M t - k_x x + k_z\ell)} \tag{A.28}$$

$$\delta B_y = 2i\delta B_{yd} \frac{\sin k_z(z - \ell)}{} e^{i(\omega_M t - k_x x + k_z\ell)} \tag{A.29}$$

Let us consider the growth (damping) rate γ for three important cases, i.e., (a) $|\gamma| \ll \mathrm{Re}(\omega_M)$ and $\vec{E}_o = 0$, (b) $|\gamma| \ll 2\alpha n_o, \mathrm{Re}(\omega_M)$, and (c) $2\alpha n_o \leq |\gamma| \leq \mathrm{Re}(\omega_M)$.

(a) $|\gamma| \ll \mathrm{Re}(\omega_M)$ and $\vec{E}_o = 0$

In this case, it is more convenient to start from the dispersion relation in the form of (A.24). Making use of (A.25), (A.24) can be rewritten as

$$e^{2ik_z\ell} = \frac{1 - \mu_o\Sigma_p V_A}{1 + \mu_o\Sigma_p V_A} \tag{A.30}$$

where k_z is a complex quantity and is expressed as

$$k_z = \frac{\omega_M}{V_A} = \mathrm{Re}(\omega_M)/V_A + i\gamma/V_A \tag{A.31}$$

Then, taking the absolute value of (A.30), we obtain

$$\exp(-2\,\frac{\ell\gamma}{V_A}) = \left|\frac{1 - \mu_o\Sigma_p V_A}{1 + \mu_o\Sigma_p V_A}\right| \tag{A.32}$$

If we square this and then expand the L.H.S. for $\ell\gamma/V_A = O(\gamma/\mathrm{Re}(\omega_M)) << 1$, we obtain

$$\frac{\ell}{V_A}\gamma = \frac{\mu_o\Sigma_p V_A}{(1 + \mu_o\Sigma_p V_A)^2} \tag{A.33}$$

From the above we see that γ is inversely proportional to $\mu_o V_A \Sigma_p$ for $\mu_o V_A \Sigma_p >> 1$, but is proportional to $\mu_o V_A \Sigma_p$ for $\mu_o V_A \Sigma_p << 1$, and has a maximum for $\mu_o V_A \Sigma_p = 1$. This dependence of γ on $\mu_o V_A \Sigma_p$ is an important result when one wishes to consider the local time dependence of the damping rate γ, as was discussed by Newton et al.[1978].

(b) $|\gamma| << 2\alpha n_o$, $\mathrm{Re}(\omega_M)$

On the assumption that the growth or damping is weak, we expand $\cot(k_z\ell)$ on the R.H.S. of (A.27) for $|\mathrm{Im}(k_z)| << \mathrm{Re}(k_z)$ and then separate the real and imaginary parts of (A.27) to obtain

$$\frac{kx(V_p + V_H)Re(\omega_M)}{Re^2(\omega_M) + (\gamma - 2\alpha n_o)^2} = 1 - \mu_o \Sigma_p \ell\gamma \mathrm{cosec}^2(\frac{\ell}{V_A} Re(\omega_M)) \qquad (A.34)$$

$$\frac{kx(V_p + V_H)(\gamma - 2\alpha n_o)}{Re^2(\omega_M) + (\gamma - 2\alpha n_o)^2} = \mu_o V_A \Sigma_p \cot(\frac{\ell}{V_A} Re(\omega_M)) \qquad (A.35)$$

Upon deviding (A.34) by (A.35) we obtain

$$\frac{Re(\omega_M)}{\gamma - 2\alpha n_o} = \frac{1}{\mu_o V_A \Sigma_p} \tan \frac{\ell}{V_A} Re(\omega_M)$$

$$\times [1 - \mu_o \Sigma_p \ell\gamma \ \mathrm{cosec}^2(\frac{\ell}{V_A} Re(\omega_M))] \qquad (A.36)$$

Thus, $Re(\omega_M)$ is determined in the limit of $\gamma \to 0$ from the intersection of two curves (see Figure A.2) for given values of $2\alpha n_o$, $\mu_o V_A \Sigma_p$ and ℓ. As can be seen from Figure A.2, for sufficiently large values of $\mu_o V_A \Sigma_p / 2\alpha n_o$, the linear curve intersects the tangent curve near $Re(\omega_M) = \pi V_A/(2\ell)$; this corresponds to the case, in which $\delta E_x \tilde{=} 0$ holds at the ionosphere.

On the other hand, γ should be determined from (A.34) as

$$\frac{\ell}{V_A}\gamma = \frac{1}{\mu_o V_A \Sigma_p} \sin^2(\frac{\ell}{V_A} Re(\omega_M))[1 - \frac{k_x(V_p + V_H)Re(\omega_M)}{Re^2(\omega_M) + (2\alpha n_o)^2}] \qquad (A.37)$$

Substitution of (A.36) in the limit of $\gamma \to 0$ into (A.37) yields

$$\frac{\ell}{V_A}\gamma = \frac{1}{\mu_o V_A \Sigma_p} \sin^2(\frac{\ell}{V_A} Re(\omega_M))[1 + \frac{k_x(V_p + V_H)2\alpha n_o}{Re^2(\omega_M) + (2\alpha n_o)^2} \frac{1}{\mu_o V_A \Sigma_p} \tan(\frac{\ell}{V_A} Re(\omega_M))] \qquad (A.38)$$

Thus, the instability occurs when the following two conditions are satisfied:

$$\tan(\frac{\ell}{V_A} Re(\omega_M)) < 0 \qquad (A.39)$$

$$\left|\frac{k_x(V_p + V_H)2\alpha n_o}{Re^2(\omega_M) + (2\alpha n_o)^2} \quad \frac{1}{\mu_o V_A \Sigma_p} \tan\left(\frac{\ell}{V_A} Re(\omega_M)\right)\right| > 1 \qquad (A.40)$$

Physical meaning of (A.39) is such that the magnetosphere is inductive as is expressed by (A.26) or alternatively,

$$\left.\frac{\delta\phi}{\delta j_z}\right|_{z=0} = -i \frac{\mu_o^2 V_A}{k_x^2} \cot k_z \ell \qquad (A.41)$$

This condition for the positive feedback is in agreement with that obtained from the physical intuition in III - 3.

(C) $2\alpha n_o \leq |\gamma| \leq Re(\omega_M)$

(A.27) can be written as

$$\frac{k_x (V_H + V_p)[Re(\omega_M) - i(\gamma - 2\alpha n_o)]}{Re^2(\omega_M) + (\gamma - 2\alpha n_o)^2} = 1 - i\mu_o V_A \Sigma_P \cot(k_z \ell) \qquad (A.42)$$

We concern here the large growth rate γ , which arises as a result of the appearance of γ on the L.H.S. of (A.42). Therefore, we take k_z real on the right of (A.42); this is allowed as far as the condition $|\gamma| \leq Re(\omega_M)$ is satisfied for calculated eigenvalues. Then, taking real and imaginary parts of (A.42), we obtain

$$\frac{k_x(V_H + V_p)Re(\omega_M)}{Re^2(\omega_M) + (\gamma - 2\alpha n_o)^2} = 1 \qquad (A.43)$$

$$\gamma = 2\alpha n_o + \frac{Re^2(\omega_M) + (\gamma - 2\alpha n_o)^2}{k_x(V_H + V_p)} \mu_o V_A \Sigma_p \cot(Re(k_z)\ell) \qquad (A.44)$$

Combining (A.43) and (A.44) yields

$$\gamma = \mu_o V_A \Sigma_p Re(\omega_M) \cot(Re(k_z)\ell) + 2\alpha n_o \qquad (A.45)$$

Therefore, the instability arises for $\cot(\mathrm{Re}(k_z)\ell) < 0$, which means that the magnetospheric response to the ionospheric potential perturbation is inductive. Since the condition $|\gamma| \leq \mathrm{Re}(\omega_M)$ is imposed, we expect from (A.45) that the peak of $|\gamma|$, which is nearly equal to $\mathrm{Re}(\omega_M)$, occurs when

$$\mu_o V_A \Sigma_p \cot(\mathrm{Re}(k_z)\ell) = -1$$

It is natural that this condition for the maximum growth agrees with that obtained in III - 5 from (3.18), i.e., $|X| = 1$, since (3.18) can be derived from (A.27) based on the same assumption that $\cot(k_z\ell)$ is pure real. When the above condition is met, we find from (A.45) and (A.43) that

$$\gamma = -\mathrm{Re}(\omega_M) + 2\alpha n_o$$

$$\mathrm{Re}(\omega_M) = \frac{1}{2} kx(V_H + V_P)$$

in agreement with (3.19).

A-5. Energetic consideration

The energy source of the feedback instability is discussed in this subsection. Let us express ionospheric perturbations as

$$\begin{bmatrix} \delta E_x \\ \delta B_y \\ \delta J_x \\ \delta n \end{bmatrix} = \begin{bmatrix} \tilde{E}_x \\ \tilde{B}_y \\ \tilde{J}_x \\ \tilde{n} \end{bmatrix} e^{i\omega_I t} \tag{A.46}$$

If we define a time average $\langle AB \rangle$ by

$$\langle AB \rangle = \frac{1}{T} \int_o^T Re(A)Re(B)dt \tag{A.47}$$

where $T = 2\pi/Re(\omega_I)$, the ionospheric power dissipation $\langle \delta J_x \delta E_x \rangle$ is calculated from (A.7) as

$$\langle \delta J_x \delta E_x \rangle = \frac{1}{4} e^{-2\gamma t}[2\Sigma_p |\tilde{E}_x|^2 + he(M_H E_{yo} + M_p E_{xo})(\tilde{E}_x^* \tilde{n} + \tilde{E}_x \tilde{n}^*)] \tag{A.48}$$

where the star over the quantity denotes the complex conjugate. In deriving (A.48) we have assumed $|\gamma| = |Im(\omega_I)| << Re(\omega_I)$. The first term on the R.H.S. of (A.48) represents the usual Joule dissipation loss by the finite Pedersen conductivity and is always positive. The sign of the second term, however, depends importantly on the phase relationship between $\tilde{E}_x$ and $\tilde{B}_y$, since (A.48) is rewritten, making use of (A.11), as

$$\langle \delta J_x \delta E_x \rangle = \frac{1}{2} e^{-2\gamma t} \Sigma_p |\tilde{E}_x|^2 [1 - \frac{1}{\mu_o \Sigma_p} Re(\beta \frac{\tilde{B}_y}{\tilde{E}_x})] \tag{A.49}$$

That is, if $\mathrm{Re}(\beta\tilde{B}y/\tilde{E}x) > 0$, the second term, which originates from the large scale dc electric field (current), becomes a negative dissipation term. (A.49) is further reduced to

$$< \delta J_x \delta E_x > = \frac{1}{2} e^{-2\gamma t} \Sigma_p |\tilde{E}_x|^2$$

$$\times [1 + \frac{k_x(M_H E_{yo} + M_p E_{xo})}{\mu_o V_A \Sigma_p} \frac{2\alpha n_o}{(\mathrm{Re}(\omega_I) + k_x V_H)^2 + (2\alpha n_o)^2} \tan \mathrm{Re}(k_z)\ell] \quad (A.50)$$

where we have neglected terms of $O(\gamma/2\alpha n_o)$ and $O(\gamma\ell/V_A)$. Since $k_x(M_H E_{oy} + M_p E_{ox}) > 0$, we find from (A.50) that the condition (A.39) tells us that the Joule dissipation of the perturbation current arising from a combination of the stationary electric field and the density perturbation is negative.

Let us calculate the total energy of the Alfvén oscillation in the magnetosphere averaged over one time period. Making use of dielectric constant ε_A for the Alfvén wave, which is nearly equal to $\varepsilon_o c^2/V_A^2$, the energy W_M in a flux tube with length ℓ and unit cross section at the ionosphere becomes

$$W_M = \int_o^\ell dz (\frac{1}{2}\varepsilon_A <\delta E_x^2> + \frac{1}{2\mu_o} <\delta B_y^2>) \quad (A.51)$$

where the quantity <AB> is averaged for $T = 2\pi/\mathrm{Re}(\omega_M)$. If we substitute (A.18) and (A.19) into (A.51) and use (A.22) and (A.25),

$$W_M = \frac{\ell}{2\mu_o V_A^2} \exp(-2\gamma t) |\delta E_{xd}|^2 \quad (A.52)$$

where the terms of $O(\gamma/\mathrm{Re}(\omega_M))$ is neglected.

Since the ionosphere is assumed to be inifinitely thin, the ionosphere becomes only sink or source of the Alfvén wave in the magnetosphere,

the energy reservoir in the coupled system. Therefore it is required from the energy conservation that

$$\frac{\partial W_M}{\partial t} = <\delta B_y \delta E_x>_{z=0_+} / \mu_o \tag{A.53}$$

Since the relationship

$$< \delta J_x \delta E_x >_{z=0} = - < \delta B_y \delta E_x >_{z=0_+} / \mu_o$$

holds in the ionosphere, (A.53) becomes

$$\frac{\partial W_M}{\partial t} = - <\delta J_x \delta E_x>_{z=0} \tag{A.54}$$

Substitution of (A.52) and (A.50) into (A.54) yields

$$\gamma = \frac{\mu_o V_A^2 \Sigma_p}{4\ell} \left| \frac{\tilde{E}_x}{\delta E_{xd}} \right|^2$$

$$\times \left[1 + \frac{k_x (M_H E_{yo} + M_p E_{xo})}{\mu_o V_A \Sigma_p} \frac{2\alpha n_o - \gamma}{(\mathrm{Re}(\omega_I) + k_x V_H)^2 + (2\alpha n_o)^2} \tan(\mathrm{Re}(k_z)\ell)\right] \tag{A.55}$$

If there is no stationary convection field, (A.55) is reduced to

$$\frac{\ell}{V_A}\gamma = \frac{\mu_o V_A \Sigma_p}{4} \left|1 + \mathrm{Ref}\right|^2 \tag{A.56}$$

Substituting (A.24) into (A.56), we obtain

$$\frac{\ell}{V_A}\gamma = \frac{\mu_o V_A \Sigma_p}{(1 + \mu_o \Sigma_p V_A)^2} \tag{A.57}$$

Since this is the same damping rate as that given in (A.33), the damping rate derived from the dispersion relation represents the damping

of the standing Alfvén mode in the magnetosphere by the Joule dissipation in the ionosphere.

It is easily shown by using (A.23) and (A.26) that

$$\left|\frac{\tilde{E}_x}{\delta E_{xd}}\right|^2 = 4\left|\cos k_z \ell\right|^2 \left[1 + O\left(\frac{\gamma \ell}{V_A}\right)\right]$$

$$= 4\left|\frac{\sin k_z \ell}{\mu_o \Sigma_{peff} V_A}\right|^2 \left[1 + O\left(\frac{\gamma \ell}{V_A}\right)\right] \qquad (A.58)$$

The growth rate γ obtained by substituting (A.58) into (A.55) agrees with (A.38) except the appearance of Σ_{peff} instead of Σ_p. This agreement is a necessary consequence, since both (A.38) and (A.55) are derived on the same assumption of the weak instability. Thus, the previously derived instability condition that the R.H.S. of (A.38) is negative is equivalent to the condition of $<\delta j_x \delta E_x> < 0$ in the ionosphere.

It is difficult to discuss the growth rate given by (A.45) in terms of the expression of (A.55), which was obtained under the weak instability limit. However, we should point out that (A.45) can be obtained by the procedure in which we put the R.H.S. of (A.50) to be zero after replacing $2\alpha n_o$ by $(2\alpha n_o - \gamma)$. This means $<\delta j_x \delta E_x> \lesssim 0$ in the ionosphere and corresponds to the case, in which the ionospheric energy production rate is so large that the magnetosphere can store only the small part of the energy produced in the ionosphere.

Appendix B Numerical Procedures

Elliptic equation for the electrostatic potential $\phi(\theta, \psi, t)$

The electrostatic potential $\phi(\theta, \psi, t)$ in the ionosphere can be obtained by numerically solving the three-dimensional current continuity equation (2) under a proper boundary condition.

Substitution of (3) into (2) yields an elliptic equation of the form

$$A(\theta,\psi,t)\frac{\partial\phi}{\partial\psi} + B(\theta,\psi,t)\frac{\partial\phi}{\partial\theta} + C(\theta,\psi,t)\frac{\partial^2\phi}{\partial\psi^2} + D(\theta,\psi,t)\frac{\partial^2\phi}{\partial\theta^2} = E(\theta,\psi,t) \tag{B.1}$$

For the ambient state ($t = 0$), (B.1) is written as

$$A_o(\theta,\psi)\frac{\partial\phi_o}{\partial\psi} + B_o(\theta,\psi)\frac{\partial\phi_o}{\partial\theta} + C_o(\theta,\psi)\frac{\partial^2\phi_o}{\partial\psi^2} + D_o(\theta,\psi)\frac{\partial^2\phi_o}{\partial\theta^2} = E_o(\theta,\psi) \tag{B.2}$$

where $\phi_o(\theta, \psi)$ is the ambient component of the electrostatic potential $\phi(\theta, \psi, t)$ and A_o, B_o, C_o, D_o and E_o (suffix o denotes the ambient state) are expressed as

$$A_o(\theta,\psi) = -\frac{e}{r^2\sin\theta}\left[\frac{M_p}{\sin\theta}\frac{\partial N_o}{\partial\psi} + M_H\frac{\partial N_o}{\partial\theta}\right]$$

$$B_o(\theta,\psi) = \frac{e}{r^2\sin\theta}\left[M_H\frac{\partial N_o}{\partial\psi} - M_p\left(\frac{\partial N_o}{\partial\theta}\sin\theta + N_o\cos\theta\right)\right]$$

$$C_o(\theta,\psi) = -\frac{eM_pN_o}{r^2\sin^2\theta} \tag{B.3}$$

$$D_o(\theta,\psi) = -\frac{eM_p N_o}{r^2}$$

$$E_o(\theta,\psi) = \frac{J_{\parallel o}}{h}$$

where $N_o(\theta, \psi)$ and $J_{\parallel o}(\theta, \psi)$ are the ambient ionospheric electron density and the ambient field-aligned current density given by (9) and (10), respectively.

For the disturbed state ($t > 0$), we express the potential $\phi(\theta, \psi, t)$, the density $n(\theta, \psi, t)$ and the field-aligned current density $j_{\parallel}(\theta, \psi, t)$ in terms of the sum of the ambient component and the time dependent component, namely,

$$\begin{aligned} \phi(\theta,\psi,t) &= \phi_o(\theta,\psi) + \tilde{\phi}(\theta,\psi,t) \\ n(\theta,\psi,t) &= N_o(\theta,\psi) + \tilde{n}(\theta,\psi,t) \\ j_{\parallel}(\theta,\psi,t) &= J_{\parallel o}(\theta,\psi) + \tilde{j}_{\parallel}(\theta,\psi,t) \end{aligned} \qquad \text{(B.4)}$$

where $\tilde{\phi}$, $\tilde{n}$ and $\tilde{j}_{\parallel}$ denote time dependent components of ϕ, n and $j_{\parallel}$, respectively. Substitution of (B.4) into (B.1) and then subtracting (B.2) from the resulting equation give an elliptic equation for $\tilde{\phi}$, namely

$$A(\theta,\psi,t)\frac{\partial\tilde{\phi}}{\partial\psi} + B(\theta,\psi,t)\frac{\partial\tilde{\phi}}{\partial\theta} + C(\theta,\psi,t)\frac{\partial^2\tilde{\phi}}{\partial\psi^2} + D(\theta,\psi,t)\frac{\partial^2\tilde{\phi}}{\partial\theta^2} = E(\theta,\psi,t) \qquad \text{(B.5)}$$

where the coefficients are written as

$$A(\theta,\psi,t) = -\frac{e}{r^2\sin\theta}\left(\frac{M_p}{\sin\theta}\frac{\partial n}{\partial\psi} + M_H\frac{\partial n}{\partial\theta}\right)$$

$$B(\theta,\psi,t) = \frac{e}{r^2\sin\theta}\left[M_H\frac{\partial n}{\partial\psi} - M_p\left(\frac{\partial n}{\partial\theta}\sin\theta + n\cos\theta\right)\right]$$

$$C(\theta,\psi,t) = -\frac{eM_p n}{r^2\sin^2\theta} \qquad \text{(B.6)}$$

$$D(\theta,\psi,t) = -\frac{eM_p n}{r^2}$$

$$E(\theta,\psi,t) = \frac{\tilde{j}_{\parallel}}{h} - \left(\tilde{A}\frac{\partial\phi_o}{\partial\psi} + \tilde{B}\frac{\partial\phi_o}{\partial\theta} + \tilde{C}\frac{\partial^2\phi_o}{\partial\psi^2} + \tilde{D}\frac{\partial^2\phi_o}{\partial\theta^2}\right)$$

where $\tilde{A}$, $\tilde{B}$, $\tilde{C}$ and $\tilde{D}$ are calculated by (B.3) using $\tilde{n}$ instead of N_o.

The equation (B.2) is solved under the boundary condition given by (11) and (12). On the other hand, (B.5) is solved under a boundary condition specified as

$$\tilde{\phi}(\theta_{min},\ \psi,\ t) = 0 \qquad \text{(B.7)}$$

$$\tilde{j}_\theta(\theta_{max},\ \psi,\ t) = 0 \qquad \text{(B.8)}$$

where $\tilde{j}_\theta$ is a latitudinal component of the perturbed current density. Although we have not mentioned, we impose a periodic boundary condition in the ψ direction. In numerically solving these equations, we have employed an ADI code [Birkoff et al., 1962] which was newly developed for an elliptic equation with a general boundary condition (see Appendix C).

Continuity equation

The time evolution of the electron density $n(\theta,\psi,t)$ is governed by the continuity equation (1). Subtracting the equilibrium equation from (1) yields

$$\frac{\partial \tilde{n}}{\partial t} + \frac{\vec{E} \times \vec{B}_o}{B_o^2} \cdot \vec{\nabla}\tilde{n} = - \frac{\tilde{\vec{E}} \times \vec{B}_o}{B_o^2} \cdot \vec{\nabla} n_o - \frac{\tilde{j}_{\parallel}}{eh} - \gamma(j_{\parallel}) \frac{j_h}{eh}$$

$$- \alpha(2n_o\tilde{n} + \tilde{n}^2) + \alpha'\left(\frac{|\tilde{n}| - \tilde{n}}{2}\right)^2 \qquad \text{(B.9)}$$

where $\tilde{\vec{E}}$ denotes the time dependent component of the electric field. The last term in (B.9) is introduced to prevent an unphysical large electron density depletion. Since this term vanishes for a positive density perturbation ($\tilde{n} > 0$) and negligibly small when $|\tilde{n}|$ is small, the introduction of this term does not importantly affect the present numerical result.

In integrating (B.9) we use a boundary condition specified as

$$\tilde{n}(\theta_{min}, \psi, t) = \tilde{n}(\theta_{max}, \psi, t) = 0 \qquad \text{(B.10)}$$

as well as the boundary condition for $\tilde{j}_{\parallel}$

$$\tilde{j}_{\parallel}(\theta_{min}, \psi, t) = \tilde{j}_{\parallel}(\theta_{max}, \psi, t) = 0 \qquad \text{(B.11)}$$

As we have mentioned, the hyperbolic equation (B.9) is numerically integrated using an upstream-downstream difference scheme to prevent a spurious numerical dispersion.

Appendix C. An alternating-direction implicit scheme for the general elliptic partial differential equation

In this appendix, a numerical scheme is developed for solving the elliptic partial differential equation, which is subject to the general boundary condition. The numerical scheme constitutes an important part of the present numerical simulation, since it is necessary to solve the elliptic differential equation at each time step of the temporal evolution. The numerical scheme is composed of two steps: First, a simultaneous linear equation is derived systematically from a difference form of the elliptic equation. The detail of this procedure under the general boundary condition is discussed in the first half of this appendix. Second, the large-scale matrix equation obtained is solved by alternating-direction implicit methods, which constitute powerful techniques for solving elliptic and parabolic differential equations. ADI methods are rapid and accurate iterative methods, which allow to use the solution of the last time step as a "good guess" of the solution of the next time step. The latter half of this appendix is devoted to the detail of the ADI scheme and the solution of the tridigonal equation.

C-1. A prescription of the elliptic differential equation

A general form of the elliptic differential equation is

$$A(x,y)\frac{\partial\phi}{\partial y} + B(x,y)\frac{\partial\phi}{\partial x} + C(x,y)\frac{\partial^2\phi}{\partial y^2} + D(x,y)\frac{\partial^2\phi}{\partial x^2} = E(x,y) \qquad (C.1)$$

Let us consider a case, in which the solution of (C.1) is to be sought in the rectangular region R defined by $x_1 \le x \le x_M$, $y_1 \le y \le y_N$ (see Figure C.1-a). In order to specify the general boundary condition of (C.1), we introduce two integer variables IBCX and IBCY. The possible boundary conditions are then given by:

IBCX = 1. The potential ϕ satisfies mixed boundary conditions of the form

$$P\frac{\partial\phi}{\partial y} + Q\frac{\partial\phi}{\partial x} + R\phi = S \qquad (C.2)$$

at $x = x_1$ and $x = x_M$.

IBCX = 2. All variables are periodic in x. That is to say,

$$\phi(x_1,y) = \phi(x_M,y). \qquad (C.3)$$

There are similar definitions for IBCY = 1, 2. From these definitions of IBCX, IBCY, any boundary condition on the boundary of the rectangular region R is expressed by a combination of IBCX = 1, 2 and IBCY = 1, 2.

C-2. Finite difference form of the elliptic equation and the boundary condition

In order to approximate the elliptic equation (C.1) by a finite difference equation, we use a mesh system composed of M × N meshes (M meshes in the x direction and N meshes in the y direction; see Figure C.1-b). A five-point difference approximation of the elliptic equation (C.1) is then written as

$$A_{ij}\frac{\phi_{ij+1} - \phi_{ij-1}}{2\Delta y} + B_{ij}\frac{\phi_{i+ij} - \phi_{i-ij}}{2\Delta x} + C_{ij}\frac{\phi_{ij+1} - 2\phi_{ij} + \phi_{ij-1}}{(\Delta y)^2} + D_{ij}\frac{\phi_{i+1j} - 2\phi_{ij} + \phi_{i-1j}}{(\Delta x)^2} = E_{ij} \qquad (C.4)$$

where Δx and Δy are mesh sizes in the x and y directions, respectively, and i and j take $1 \sim M$ and $1 \sim N$, respectively. Note that when i = 1, M or j = 1, N, (C.4) contains 'virtual meshes' or 'virtual potentials' with i = 0, M + 1 and j = 0, N + 1, which belong exterior to the region R. These meshes are necessary for keeping the second order accuracy of difference approximation in the entire solution region. When the periodic boundary condition is imposed (IBCX = 2 or IBCY = 2), however, these virtual meshes can be removed by replacing them by equivalent meshes near the opposite boundaries. Multiplying (C.4) by $\Delta x \cdot \Delta y$ yields

$$a_{ij}\phi_{i-ij} + b_{ij}\phi_{ij} + c_{ij}\phi_{i+1j} + d_{ij}\phi_{ij-1} + g_{ij}\phi_{ij} + e_{ij}\phi_{ij+1} = f_{ij} \quad (i = 1 \sim M,\ j = 1 \sim N) \qquad (C.5)$$

where

$$
\begin{aligned}
a_{ij} &= -\left(\frac{\Delta y}{\Delta x} D_{ij} - \frac{\Delta y}{2} B_{ij}\right) \\
b_{ij} &= 2 \frac{\Delta y}{\Delta x} D_{ij} \\
c_{ij} &= -\left(\frac{\Delta y}{\Delta x} D_{ij} + \frac{\Delta y}{2} B_{ij}\right) \\
d_{ij} &= -\left(\frac{\Delta x}{\Delta y} C_{ij} - \frac{\Delta x}{2} A_{ij}\right) \\
g_{ij} &= 2 \frac{\Delta x}{\Delta y} C_{ij} \\
e_{ij} &= -\left(\frac{\Delta x}{\Delta y} C_{ij} + \frac{\Delta x}{2} A_{ij}\right) \\
f_{ij} &= -\Delta x \Delta y E_{ij}
\end{aligned}
\qquad (i = 1 \sim M,\ j = 1 \sim M) \qquad (C.6)
$$

We show in Figure C.2-a a mnemonic diagram of the difference equation (C.5).

Next, the five-point difference approximation of the boundary condition (C.2) (IBCX = 1 or IBCY = 1) is expressed as

$$
P_{k\ell} \frac{\phi_{k\ell+1} - \phi_{k\ell-1}}{2\Delta y} + Q_{k\ell} \frac{\phi_{k+1\ell} - \phi_{k-1\ell}}{2\Delta x} + R_{k\ell}\phi_{k\ell} = S_{k\ell} \qquad (C.7)
$$

where symbolically expressed by (k,ℓ) are $(1, j)$ $(M, j)(j = 1 \sim N)$ when IBCX = 1 and $(i, 1)$, $(i, N)(i = 1 \sim M)$ when IBCY = 1. Multiplying (C.7) by $(\Delta x \Delta y)^{1/2}$ yields

$$
\begin{aligned}
&a'_{k\ell}\phi_{k-1\ell} + b'_{k\ell}\phi_{k\ell} + c'_{k\ell}\phi_{k+1\ell} + d'_{k\ell}\phi_{k\ell-1} + g'_{k\ell}\phi_{k\ell} + e'_{k\ell}\phi_{k\ell+1} \\
&\qquad = f'_{k\ell} \qquad (C.8)
\end{aligned}
$$

where

$$
\begin{aligned}
a'_{k\ell} &= -\frac{1}{2}\left(\frac{\Delta y}{\Delta x}\right)^{1/2} Q_{k\ell} \\
b'_{k\ell} &= \frac{1}{2}(\Delta x \Delta y)^{1/2} R_{k\ell} \\
c'_{k\ell} &= \frac{1}{2}\left(\frac{\Delta y}{\Delta x}\right)^{1/2} Q_{k\ell} \\
d'_{k\ell} &= -\frac{1}{2}\left(\frac{\Delta x}{\Delta y}\right)^{1/2} P_{k\ell} \\
g'_{k\ell} &= \frac{1}{2}(\Delta x \Delta y)^{1/2} R_{k\ell} \\
e'_{k\ell} &= \frac{1}{2}\left(\frac{\Delta x}{\Delta y}\right)^{1/2} P_{k\ell} \\
f'_{k\ell} &= (\Delta x \Delta y)^{1/2} S_{k\ell}
\end{aligned}
\qquad \text{(C.9)}
$$

Note that when IBCX = 1 and IBCY = 1, (C.9) defines two different groups of $a'_{11} \sim f'_{11}$, $a'_{M1} \sim f'_{M1}$, $a'_{1N} \sim f'_{1N}$, $a'_{MN} \sim f'_{MN}$, which are expressed by the same symbols. The mnemonic representation of the boundary condition (C.8) is shown in Figure C.2-b. Although (C.8) includes virtual meshes when IBCX = 1 or IBCY = 1, they are eliminated by combining, (C.8) and (C.5).

C-3. General boundary conditions

The possible combinations of the boundary conditions in x and y direction are as follows:

(a) IBCX = 2, IBCY = 2 (doubly periodic case)

(b) IBCX = 1, IBCY = 2 or IBCX = 2, IBCY = 1

(c) IBCX = 1, IBCY = 1

Since the case of IBCX = 2 and IBCY = 1 does not differ essentially from the case of IBCX = 1 and IBCY = 2, only the case of IBCX = 1 and IBCY = 2 is considered in (b). The mesh system and the procedure of removing the virtual meshes are shown schematically in Figure C.3 for above three different cases. When IBCX = 2 and IBCY = 2 (Figure C.3-a), the virtual meshes exterior to the closed region R can be replaced, making use of the boundary condition (C.3), by meshes with i = 2, M - 1, j = 2, N - 1. In this case, therefore, there is no need of removing virtual meshes. In cases (b) and (c), however, substantial virtual meshes exist and they cannot be replaced by equivalent meshes. We thus have to remove these virtual meshes to make the difference equations (C.4) - (C.9) amenable to a large-scale matrix equation including only unknown potentials at real meshes. The underlying mathematics for removing the virtual meshes (potential) is to eliminate them from simultaneous linear equations (C.5) and (C.8)[Smith, 1965]. The resultant mesh system after this removal is shown in Figure C.4.

C-4. Alternating-direction implicit method for the solution of the elliptic equation

A difference form of the elliptic equation (C.1) can be written as a vector equation of the form

$$(H + V)u = k \tag{C.10}$$

where u is an approximate solution of the boundary value problem (C.1) - (C.3). H and V are difference operators of the form

$$Hu(x,y) = a(x,y)u(x - \Delta x,y) + b(x,y)u(x,y) + c(x,y)u(x + \Delta x,y) \tag{C.11}$$

$$Vu(x,y) = d(x,y)u(x,y - \Delta y) + g(x,y)u(x,y) + e(x,y)u(x,y + \Delta y) \tag{C.12}$$

where a, b, c, d, g, e are given by (C.6). Alternating - direction implicit scheme is a method of rapidly solving the vector equation (C.10) for large mesh networks. (C.10) is clearly equivalent, for any ρ (a scalar constant) and I(unit matrix), to each of the two vector equations

$$(H + \rho I)u = k - (V - \rho I)u \tag{C.13}$$

$$(V + \rho I)u = k - (H - \rho I)u \tag{C.14}$$

Peaceman and Rachford [1955] proposed solving (C.10) by choosing an approximate sequence of positive numbers ρ_n, and calculating the sequence

of vectors u_n, $u_{n+\frac{1}{2}}$ defined from the sequence of matrices $\rho_n I$, by the formulas

$$(H + \rho_n I)u_{n+\frac{1}{2}} = k - (V - \rho_n I)u_n \tag{C.15}$$

$$(V + \rho_n I)u_{n+\frac{1}{2}} = k - (H - \rho_n I)u_{n+\frac{1}{2}} \tag{C.16}$$

The approximate solution of u at sequential step can be written explicitly as

$$u_{n+\frac{1}{2}} = (H + \rho_n I)^{-1}[k - (V - \rho_n I)u_n] \tag{C.17}$$

$$u_{n+1} = (V + \tilde{\rho}_n I)^{-1}[k - (V - \tilde{\rho}_n I)u_{n+\frac{1}{2}}] \tag{C.18}$$

An approximate solution of (C.10) is then obtained by iterating (C.17) and (C.18) starting from a trial vector u_o. Since H and V become similar to tridiagonal matrix by ordering the mesh-points by rows or by columns for the general boundary condition, (C.17) and (C.18) can be rapidly solved by Gauss elimination method. The rate of convergence will depend strongly on the choice of the iteration parameters ρ_n, $\tilde{\rho}_n$ [Birkhoff et al., 1962].

C-5. Removal of the virtual meshes and matrix equations from the finite difference equation

Let us obtain a concrete form of the sparse matrices H and V for three different cases of boundary condition.

(a) IBCX = 2, IBCY = 2 (doubly periodic case)

In this case, there is no need of removing virtual meshes since they can be replaced by equivalent mesh points interior to the region R. There are (M - 1) × (N - 1) unknown potentials at discretized mesh points. The boundary condition (C.3) says $\phi_{Mj} = \phi_{1j} (j = 1 \sim N)$ and $\phi_{iN} = \phi_{il} (i = 1 \sim M)$. By ordering the mesh points by rows, the matrix H can then be written as

$$H = \begin{bmatrix} H_1 & & & & \\ & H_2 & & \mathbf{O} & \\ & & \ddots & & \\ & & & H_j & \\ & \mathbf{O} & & & \ddots \\ & & & & & H_{N-1} \end{bmatrix} \qquad \text{(C.19)}$$

where

$$H_j = \begin{bmatrix} b_{1j} & c_{1j} & & & & & a_{1j} \\ a_{2j} & b_{2j} & c_{2j} & & & \mathbf{O} & \\ & \ddots & \ddots & \ddots & & & \\ & & a_{ij} & b_{ij} & c_{ij} & & \\ & & & \ddots & \ddots & \ddots & \\ & \mathbf{O} & & & a_{M-2j} & b_{M-2j} & c_{M-2j} \\ c_{M-ij} & & & & & a_{M-1j} & b_{M-1j} \end{bmatrix} \qquad \text{(C.20)}$$

$(j = 1 \sim N)$

Note that H_j is not simply tridiagonal owing to the periodic boundary condition imposed in the x direction. On the other hand, by ordering mesh points by columns, the matrix V can be expressed as

$$V = \begin{bmatrix} V_1 & & & & \\ & V_2 & & \text{O} & \\ & & \ddots & & \\ & & & V_i & \\ & \text{O} & & & \ddots \\ & & & & & V_{M-1} \end{bmatrix} \qquad \text{(C.21)}$$

where

$$V_i = \begin{bmatrix} g_{i1}e_{i1} & & & & & d_{i1} \\ d_{i2}g_{i2}e_{i2} & & & & & \\ & d_{i3}g_{i3}e_{i3} & & \text{O} & & \\ & & \ddots & & & \\ & & & d_{ij}g_{ij}e_{ij} & & \\ & & & & \ddots & \\ & \text{O} & & & d_{iN-2}g_{iN-2}e_{iN-2} & \\ & & & & & d_{iN-1}g_{iN-1} \\ e_{iN-1} & & & & & \end{bmatrix} \qquad \text{(C.22)}$$

$$(i = 1 \sim M - 1)$$

Since H and V are block diagonal matrices and are thus partioned into independent pseudo-tridiagonal matrices, (C.17) and (C.18) can be solved rapidly by the Gauss elimination method, which will be discussed in the next subsection.

(b) IBCX = 1, IBCY = 2

In this case, there are M × (N - 1) unknown potentials at discretized mesh points and 2 × (N - 1) virtual meshes with i = 0, M + 1 exterior to the region R (see Figure C.3-b). They can be removed by using 2 × (N -1) boundary conditions expressed by (C.8). That is, by putting i = 1 in (C.5) and (C.8), we obtain two simultaneous linear equations

$$a_{1j}\phi_{oj} + b_{1j}\phi_{1j} + c_{1j}\phi_{2j} + d_{1j}\phi_{1j-1} + g_{1j}\phi_{1j} + e_{1j}\phi_{1j+1} = f_{1j} \tag{C.23}$$

$$a'_{1j}\phi_{oj} + b'_{1j}\phi_{1j} + c'_{1j}\phi_{2j} + d'_{1j}\phi_{1j-1} + g'_{1j}\phi_{1j} + e'_{1j}\phi_{1j+1} = f'_{1j} \qquad (j = 1 \sim N - 1) \tag{C.24}$$

If we eliminate ϕ_{oj} from above two equations, we obtain

$$b''_{1j}\phi_{1j} + c''_{1j}\phi_{2j} + d''_{1j}\phi_{1j-1} + g''_{1j}\phi_{1j} + e''_{1j}\phi_{1j+1} = f''_{1j} \qquad (j = 1 \sim N - 1) \tag{C.25}$$

where

$$\begin{bmatrix} b''_{1j} \\ c''_{1j} \\ d''_{1j} \\ g''_{1j} \\ e''_{1j} \\ f''_{1j} \end{bmatrix} = a_{1j} \begin{bmatrix} b'_{1j} \\ c'_{1j} \\ d'_{1j} \\ g'_{1j} \\ e'_{1j} \\ f'_{1j} \end{bmatrix} - a'_{1j} \begin{bmatrix} b_{1j} \\ c_{1j} \\ d_{1j} \\ g_{1j} \\ e_{1j} \\ f_{1j} \end{bmatrix} \tag{C.26}$$

Next, putting i = M in (C.5) and (C.8) yields

$$a_{Mj}\phi_{M-1j} + b_{Mj}\phi_{Mj} + c_{Mj}\phi_{M+1j} + d_{Mj}\phi_{Mj-1} + g_{Mj}\phi_{Mj} + e_{Mj}\phi_{Mj+1} = f_{Mj} \tag{C.27}$$

$$a'_{Mj}\phi_{M-1j} + b'_{Mj}\phi_{Mj} + c'_{Mj}\phi_{M+1j} + d'_{Mj}\phi_{Mj-1} + g'_{Mj}\phi_{Mj} + e'_{Mj}\phi_{Mj+1} = f'_{Mj} \tag{C.28}$$

$$(j = 1 \sim N - 1)$$

We eliminate ϕ_{M+1j} from above two equations to obtain

$$a''_{Mj}\phi_{M-1j} + b''_{Mj}\phi_{Mj} + d''_{Mj}\phi_{Mj-1} + g''_{Mj}\phi_{Mj} + e''_{Mj}\phi_{Mj+1} = f''_{Mj} \tag{C.29}$$

$$(j = 1 \sim N - 1)$$

where

$$\begin{bmatrix} a''_{Mj} \\ b''_{Mj} \\ d''_{Mj} \\ g''_{Mj} \\ e''_{Mj} \\ f''_{Mj} \end{bmatrix} = c_{Mj} \begin{bmatrix} a'_{Mj} \\ b'_{Mj} \\ d'_{Mj} \\ g'_{Mj} \\ e'_{Mj} \\ f'_{Mj} \end{bmatrix} - c'_{Mj} \begin{bmatrix} a_{Mj} \\ b_{Mj} \\ d_{Mj} \\ g_{Mj} \\ e_{Mj} \\ f_{Mj} \end{bmatrix} \tag{C.30}$$

Thus, making use of (C.5) for i = 2 ∿ M - 1, j = 1 ∿ N - 1, (C.25), and (C.29), we can express the matrix H as

$$H = \begin{bmatrix} H_1 & & & \\ & H_2 & & \\ & & \ddots & \\ & & & H_{N-1} \end{bmatrix} \qquad \text{(C.31)}$$

where

$$H_j = \begin{bmatrix} b''_{1j} & c''_{1j} & & & \\ a_{2j} & b_{2j} & c_{2j} & & \\ & \ddots & \ddots & \ddots & \\ & & a_{ij} & b_{ij} & c_{ij} \\ & & & \ddots & \ddots \\ & & & a_{M-1j} & b_{M-ij} \quad c_{M-ij} \\ & & & & a''_{Mj} \quad b''_{Mj} \end{bmatrix} \qquad \text{(C.32)}$$

$$(j = 1 \sim N - 1)$$

Owing to the periodic boundary condition imposed in the y direction, the matrix V can be expressed as

$$V = \begin{bmatrix} V_1 & & & \\ & V_2 & & \\ & & \ddots & \\ & & & V_M \end{bmatrix} \qquad \text{(C.33)}$$

where V_i is defined by the same matrix as (C.22).

(C) IBCX = 1, IBCY = 1

In this case, there are M × N unknown potentials at discretized mesh points and 2(M + N) virtual meshes (potentials) exterior to the region R. Removing of virtual meshes is performed by the similar procedure as is used for case (b), i.e., elimination of virtual meshes from (C.5) and (C.8). However, special attention must be paid to four mesh points at the corner of the rectangular region R, since (C.5) and (C.8) differs from those in case (b) in that they include two virtual mesh points at each corner mesh point. Let us consider, without loss of generality, a corner mesh point of i = j = 1. Three equations, which hold at the corner mesh points, are given by putting i = j = 1 in (C.5) and (C.8) as

$$a_{11}\phi_{01} + b_{11}\phi_{11} + c_{11}\phi_{21} + d_{11}\phi_{10} + g_{11}\phi_{12} + e_{11}\phi_{12} = f_{11} \quad \text{(C.34)}$$

$$a^x_{11}\phi_{01} + b^x_{11}\phi_{11} + c^x_{11}\phi_{21} + d^x_{11}\phi_{10} + g^x_{11}\phi_{11} + e^x_{11}\phi_{12} = f^x_{11} \quad \text{(C.35)}$$

$$a^y_{11}\phi_{01} + b^y_{11}\phi_{11} + c^y_{11}\phi_{21} + d^y_{11}\phi_{10} + g^y_{11}\phi_{11} + e^y_{11\ 12} = f^y_{11} \quad \text{(C.36)}$$

Note that (C.35) and (C.36) were derived from the boundary condition at $x = x_1$ and $y = y_1$, respectively. We eliminate ϕ_{01} from (C.34) and (C.35) to obtain

$$b^{x'}_{11}\phi_{11} + c^{x'}_{11}\phi_{21} + d^{x'}_{11}\phi_{10} + g^{x'}_{11}\phi_{11} + e^{x'}_{11}\phi_{12} = f^{x'}_{11} \quad \text{(C.37)}$$

where $b^{x'}_{11} \sim f^{x'}_{11}$ are given by the analogous formula as (C.26). Elimination of Φ_{01} from (C.34) and (C.36), on the other hand, yields

$$b^{y'}_{11}\phi_{11} + c^{y'}_{11}\phi_{21} + d^{y'}_{11}\phi_{10} + g^{y'}_{11}\phi_{11} + e^{y'}_{11}\phi_{12} = f^{y'}_{11} \quad \text{(C.38)}$$

where $b_{11}^{y'} \sim f_{11}^{y'}$ are given by the analogous formula as (C.26). We obtain by eliminating ϕ_{10} from (C.37) and (C.38)

$$b''_{11}\phi_{11} + C''_{11}\phi_{21} + g''_{11}\phi_{11} + e''_{11}\phi_{12} = f''_{11} \tag{C.39}$$

This is the final form of the linear equation without any virtual potential. The coefficients $b''_{11} \sim f''_{11}$ in (C.39) are given by

$$\begin{bmatrix} b''_{11} \\ c''_{11} \\ g''_{11} \\ e''_{11} \\ f''_{11} \end{bmatrix} = d_{11}^{x'} \begin{bmatrix} b_{11}^{y'} \\ c_{11}^{y'} \\ g_{11}^{y'} \\ e_{11}^{y'} \\ f_{11}^{y'} \end{bmatrix} - d_{11}^{y'} \begin{bmatrix} b_{11}^{x'} \\ c_{11}^{x'} \\ g_{11}^{x'} \\ e_{11}^{x'} \\ f_{11}^{y'} \end{bmatrix} \tag{C.40}$$

Correspondingly, by the same procedure, we obtain three other linear equations at three other corner points, namely

$$a''_{M1}\phi_{M-1} + b''_{M1}\phi_{M1} + g''_{M1}\phi_{M1} + e''_{M1}\phi_{M2} = f''_{M1} \tag{C.41}$$

$$b''_{1N}\phi_{1N} + c''_{1N}\phi_{2N} + d''_{1N}\phi_{1N-1} + g''_{1N}\phi_{1N} = f''_{1N} \tag{C.42}$$

$$a''_{MN}\phi_{M-1} + b''_{MN}\phi_{MN} + d''_{MN}\phi_{MN-1} + g''_{MN}\phi_{MN} = f''_{MN} \tag{C.43}$$

where the coefficients above are given by the analogous formula as (C.40). At mesh points on the boundary except four corner points, only

one virtual potential (mesh) is included in linear equations (C.5) and (C.8). Therefore at these mesh points, the same operation used in the case (b) is adopted to remove the virtual meshes with i = 0, M + 1. The result is

$$b''_{1j}\phi_{1j} + c''_{1j}\phi_{2j} + d''_{1j}\phi_{1j-1} + g''_{1j}\phi_{1j} + e''_{1j}\phi_{1j+1} = f''_{1j} \qquad (C.44)$$

$$a''_{Mj}\phi_{M-1j} + b''_{Mj}\phi_{Mj} + d''_{Mj}\phi_{Mj-1} + g''_{Mj}\phi_{Mj} + e''_{Mj}\phi_{Mj+1} = f''_{Mj} \qquad (C.45)$$

$$(j = 2 \sim N - 1)$$

where the coefficients are given by (C.26) and (C.30). Note that j varies from 2 to N-1, since the equation at the corner point is already given by (C.39) - (C.43). By the same procedure we can remove the virtual meshes with j = 0, N + 1 to obtain

$$a''_{i1}\phi_{i-11} + b''_{i1}\phi_{i1} + c''_{i1}\phi_{i+11} + g''_{i1}\phi_{i1} + e''_{i1}\phi_{i2} = f''_{i1} \qquad (C.46)$$

$$a''_{iN}\phi_{i-1N} + b''_{iN}\phi_{iN} + c''_{iN}\phi_{i+1N} + d''_{iN}\phi_{iN-1} + g''_{iN}\phi_{iN} = f''_{iN} \qquad (C.47)$$

where

$$\begin{bmatrix} a''_{i1} \\ b''_{i1} \\ c''_{i1} \\ g''_{i1} \\ e''_{i1} \\ f''_{i1} \end{bmatrix} = d_{i1} \begin{bmatrix} a'_{i1} \\ b'_{i1} \\ c'_{i1} \\ g'_{i1} \\ e'_{i1} \\ f'_{i1} \end{bmatrix} - d'_{i1} \begin{bmatrix} a_{i1} \\ b_{i1} \\ c_{i1} \\ g_{i1} \\ e_{i1} \\ f_{i1} \end{bmatrix} \qquad (C.48)$$

and

$$\begin{bmatrix} a''_{iN} \\ b''_{iN} \\ c''_{iN} \\ d''_{iN} \\ g''_{iN} \\ f''_{iN} \end{bmatrix} = e_{iN} \begin{bmatrix} a'_{iN} \\ b'_{iN} \\ c'_{iN} \\ d'_{iN} \\ g'_{iN} \\ f'_{iN} \end{bmatrix} - e'_{iN} \begin{bmatrix} a_{iN} \\ b_{iN} \\ c_{iN} \\ d_{iN} \\ g_{iN} \\ f_{iN} \end{bmatrix} \qquad \text{(C.49)}$$

Note that suffix i varies from 2 to M-1 in (C.46) - (C. 49).

From the above equations, the matrix H can be expressed as

$$H = \begin{bmatrix} H_1 & & & & \\ & H_2 & & \text{O} & \\ & & \ddots & & \\ & & & H_j & \\ & \text{O} & & & \ddots \\ & & & & & H_N \end{bmatrix} \qquad \text{(C.50)}$$

where

$$H_j = \begin{bmatrix} b''_{ij} c''_{ij} & & & & \\ a_{2j} b_{2j} c_{2j} & & & \text{O} & \\ & \ddots & & & \\ & & a_{ij} b_{ij} c_{ij} & & \\ & & & \ddots & \\ & \text{O} & & & a_{M-1j} b_{M-1j} c_{M-1j} \\ & & & & a''_{Mj} \quad b''_{Mj} \end{bmatrix} \qquad \text{(C.51)}$$

$(j = 1 \sim N)$

It should be noted that $b''_{11}, c''_{11}, a''_{M1}, b''_{M1}$ and $b''_{1N}, c''_{1N}, a''_{MN}, b''_{MN}$ are given by (C.40) and the analogous formula associated with (C.41) - (C.43).

The matrix V can be expressed as

$$V = \begin{bmatrix} V_1 & & & \\ & V_2 & & \\ & & \ddots & \\ & & & V_M \end{bmatrix} \qquad \text{(C.52)}$$

where

$$V_i = \begin{bmatrix} g''_{i1} & e''_{i1} & & & & \\ d''_{i1} & g''_{i1} & e''_{i1} & & & \\ & \ddots & \ddots & \ddots & & \\ & & d''_{ij} & g''_{ij} & e''_{ij} & \\ & & & \ddots & \ddots & \ddots \\ & & & & d''_{iN-1} & g''_{iN-1} & e''_{iN-1} \\ & & & & & d''_{iN} & g''_{iN} \end{bmatrix} \qquad \text{(C.53)}$$

C-6. Recurrence solution of the tridiagonal matrix equation

Now that we have obtained a concrete form of H and V, we can obtain an approximate solution of ϕ from (C.17) and (C.18). The Gauss elimination method is used to solve the tridiagonal matrices, which appear in (C.17) and (C.18). As we have seen in the previous subsection, H and V are composed of two types of tridiagonal or pseudo-tridiagonal matrices. Namely, when IBCX = 1 or IBCY = 1, the next matrix equation must be solved:

$$\begin{bmatrix} \beta_1\gamma_1 & & & & & \\ \alpha_2\beta_2\gamma_2 & \ddots & & & & \\ & \ddots & \ddots & & & \\ & & \alpha_j\beta_j\gamma_j & \ddots & & \\ & & & \ddots & \ddots & \\ & & & & \alpha_{N-1}\beta_{N-1}\gamma_{N-1} & \\ & & & & \alpha_N & \beta_N \end{bmatrix} \begin{bmatrix} u_1 \\ u_2 \\ \\ u_j \\ \\ u_{N-1} \\ u_N \end{bmatrix} = \begin{bmatrix} \delta_1 \\ \delta_2 \\ \\ \delta_j \\ \\ \delta_{N-1} \\ \delta_N \end{bmatrix} \qquad \text{(C.54)}$$

When IBCX = 2 or IBCY = 2, the solution of the next equation is required:

$$\begin{bmatrix} \beta_1\gamma_1 & & & & \alpha_1 \\ \alpha_2\beta_2\gamma_2 & \ddots & & & \\ & \ddots & \ddots & & \\ & & \alpha_j\beta_j\gamma_j & \ddots & \\ & & & \ddots & \\ \gamma_N & & & & \alpha_N\beta_N \end{bmatrix} \begin{bmatrix} u_1 \\ u_2 \\ \\ u_j \\ \\ u_N \end{bmatrix} = \begin{bmatrix} \delta_1 \\ \delta_2 \\ \\ \delta_j \\ \\ \delta_N \end{bmatrix} \qquad \text{(C.55)}$$

By the Gauss elimination method, the solution of (C.5$_4$) is reduced to

the next recurrence formula [e.g., Potter, 1973]:

$$u_N = \frac{\delta''_N}{\beta''_N} \tag{C.56}$$

$$u_i = \frac{\delta''_i - \gamma_i u_{i+1}}{\beta''_i} \quad (i = N-1, N-2, \cdots, 1) \tag{C.57}$$

where the coefficients are given by

$$\beta''_1 = \beta_1 \; ; \quad \beta''_i = \beta_i - \frac{\alpha_i}{\beta''_{i-1}}\gamma_{i-1} (i = 2, 3, \cdots, N) \tag{C.58}$$

$$\delta''_1 = \delta_1 \; ; \quad \delta''_i = \delta_i - \frac{\alpha_i}{\beta''_{i-1}}\delta''_{i-1} (i = 2, 3, \cdots, N) \tag{C.59}$$

It is not difficult to show by the Gauss elimination method that the solution of (C.55) is given by the next recurrence formula

$$u_N = \frac{\delta_N^{(N-1)}}{\beta_N^{(N-1)}} \tag{C.60}$$

$$u_{N-1} = \frac{\delta'_{N-1} - \gamma'_{N-1} u_N}{\beta'_{N-1}} \tag{C.61}$$

$$u_i = \frac{\delta'_i - \gamma_i u_{i+1} - \alpha'_i u_N}{\beta'_i} \tag{C.62}$$

$$(i = N-2, N-1, \cdots\cdots, 2, 1)$$

where the coefficients are given by

$$\begin{cases} \alpha'_1 = \alpha_1 \\ \beta'_1 = \beta_1 \\ \delta'_1 = \delta_1 \end{cases} \tag{C.63}$$

$$\begin{cases} \beta'_i = \beta_i - \dfrac{\alpha_i \gamma_{i-1}}{\beta'_{i-1}} \; ; \; \gamma_N^{(i-1)} = - \dfrac{\gamma_N^{(i-2)} \gamma_{i-1}}{\beta'_{i-1}} \\ \alpha'_i = - \dfrac{\alpha_i \alpha'_{i-1}}{\beta'_{i-1}} \; ; \; \beta_N^{(i-1)} = \beta_N^{(i-2)} - \dfrac{\gamma_N^{(i-2)} \alpha'_{i-1}}{\beta'_{i-1}} \quad (i = 2, 3, \cdots, N-2) \\ \delta'_i = \delta_i - \dfrac{\alpha_i \gamma'_{i-1}}{\beta'_{i-1}} \; ; \; \delta_N^{(i-1)} = \delta_N^{(i-2)} - \dfrac{\gamma_N^{(i-2)} \delta'_{i-1}}{\beta'_{i-1}} \end{cases} \tag{C.64}$$

$$\begin{cases} \beta'_{N-1} = \beta_{N-1} - \dfrac{\alpha_{N-1} \gamma_{N-2}}{\beta'_{N-2}} \; ; \; \alpha_N^{(N-2)} = \alpha_N - \dfrac{\gamma_N^{(N-3)} \gamma_{N-2}}{\beta'_{N-2}} \\ \gamma'_{N-1} = \gamma_{N-1} - \dfrac{\alpha_{N-1} \alpha'_{N-2}}{\beta'_{N-2}} \; ; \; \beta_N^{(N-2)} = \beta_N^{(N-3)} - \dfrac{\gamma_N^{(N-3)} \alpha'_{N-2}}{\beta'_{N-2}} \\ \delta'_{N-1} = \delta_{N-1} - \dfrac{\alpha_{N-1} \delta'_{N-2}}{\beta'_{N-2}} \; ; \; \delta_N^{(N-2)} = \delta_N^{(N-3)} - \dfrac{\gamma_N^{(N-3)} \delta'_{N-2}}{\beta'_{N-2}} \end{cases} \tag{C.65}$$

$$\begin{cases} \beta_N^{(N-1)} = \beta_N^{(N-2)} - \dfrac{\alpha_N^{(N-2)} \gamma'_{N-1}}{\beta'_{N-1}} \\ \delta_N^{(N-1)} = \delta_N^{(N-2)} - \dfrac{\alpha_N^{(N-2)} \delta'_{N-1}}{\beta'_{N-1}} \end{cases} \tag{C.66}$$

References

Aggson, T.L., Probe measurements of electric fields in space, in Atmospheric emissions, edited by B.M. McCormac and A. Omholt, D. Reidel, Hingham, Mass, 1969.

Akasofu, S.-I., Physics of magnetospheric substorms, B.M. McCormac(ed)., D. Reidel Publ. Co., Dordrecht-Holland., 1977.

Armstrong, J.C., S.-I., Akasofu, and G. Rostoker, A comparison of satellite observations of Birkeland currents with ground observations of visible aurora and ionospheric currents, J. Geophys. Res., 80, 575-586, 1975.

Armstrong, J.C. and A.J. Zmuda, Field-aligned current at 1100 km in the auroral region measured by satellite, J. Geophys. Res., 75, 7122-7127. 1970.

Arnoldy, R.L., P.B. Lewis and P.O. Isaacson, Field-aligned auroral electron fluxes, J. Geophys. Res., 79, 4208-4221, 1974.

Atkinson, G., Auroral arcs: Result of the interaction of a dynamic magnetosphere with the ionosphere, J. Geophys. Res., 75, 4746-4755, 1970.

Banks, P.M., J.R. Doupnik, and S.-I. Akasofu, Electric field observations by incoherent scatter radar in the auroral zone, J. Geophys Res., 78, 6607-6622, 1973.

Beaujardiere, O., R. Vondrak, and M. Baron, Radar observations of electric fields and currents associated with auroral arcs, J. Geophys. Res., 82, 5051-5062, 1977.

Belon, A.E., J.E. Maggs, T.N. Davis, K.B. Mather, N.W. Glass, and G.F. Hughes, Conjugacy of visual auroras during magnetically quiet periods, J. Geophys. Res., 74, 1-28, 1969.

Birkoff, G., R.S. Varga, and D. Young, Alternating direction implicit methods. Advances in Computers, 189-273, Academic Press, 1962.

Block, L.P., Potential double layers in the ionosphere, Cosmic Electrodynamics, 3, 346, 1972.

Boström, R. , A model of the auroral electrojets, J. Geophys. Res., 69, 4983-4999, 1964.

Brekke, A., J.R. Doupnik, and P.M. Banks, Incoherent scatter measurements of E region conductivities and currents in the auroral zone, J. Geophys. Res., 79, 3773, 1974.

Byers, J.A., and J. Killeen, Finite-difference methods for collisionless plasma models, Methods in computational physics, 9, B. Alder(ed.), Adacemic Press, New York, 1970.

Carlson, C.W., and M.C. Kelley, Observation and interpretation of particle and electric field measurements inside and adjacent to an active auroral arc, J. Geophys. Res., 82, 2349-2360, 1977.

Casserly R.T., and P.A. Cloutier, Rocket-based magnetic observations of auroral Birkeland currents in associateion with a structured auroral arc, J. Geophys. Res., 80, 2165-2168, 1975.

Cloutier, P.A., B.R. Sandel, H.R. Anderson, P.M. Pazich, and R.J. Spiger, Measurement of auroral Birkeland currents and energetic particles, J. Geophys. Res., 78, 640-647, 1973.

Davis, T.N., Observed characteristics of auroral forms, Space Sci. Rev., 22, 77-113, 1978.

Dewitt, R.N., Polarization of the auroral electrojet, J. Geophys. Res., 73, 6307-6311, 1968.

Evans, D.S., The observations of a near monoenergetic flux of auroral electrons, J. Geophys. Res., 73, 2315-2324, 1968.

Feldstein, Y.I., Peculiarities in the auroral distribution and magnetic disturbance distribution in high latitudes caused by the asymmetrical form of the magnetosphere, Planet. Space Sci., 14, 121-130, 1966.

Hasegawa, A., Particle acceleration by MHD surface wave and formation of aurora, J. Geophys. Res., 81, 5083-5090, 1976.

Heppner, J.P., Electric field variations during substorms: Ogo 6 measurements, Planet Space Sci., 20, 1475-1498, 1972.

Heppner, J.P., Empirical models of high-latitude electric fields, J. Geophys. Res., 82, 1115-1125, 1977.

Holzer, T.E., and T. Sato, Quiet auroral arcs and electrodynamic coupling between the ionosphere and the magnetosphere, 2, J. Geophys. Res., 78, 7330-7339, 1973.

Horwitz, J.L., J.R. Doupnik, and P.M. Banks, Chatanika radar observations of the latitudinal distributions of auroral zone electric fields, conductivities, and currents, J. Geophys. Res., 83, 1463-1481, 1978.

Hubbard, R.F. and G. Joyce, Simulation of auroral double layers, J. Geophys. Res., 84, 4294-4304, 1979.

Hughes W.J. and D.J. Southwood, The screening of micropulsation signals by the atmosphere and ionosphere, J. Geophys. Res., 81, 3234-3240, 1976.

Iijima, T., and T.A. Potemra, The amplitude distribution of field-aligned currents at northern high latitudes observed by Triad, J. Geophys. Res., 81, 2165, 1976 a.

Iijima, T., and T.A. Potemra, Field-aligned currents in the dayside cusp observed by Triad, J. Geophys. Res., 81, 5971-5979, 1979 b.

Kamide, Y., and S.-I. Akasofu, The location of the field-aligned currents with respect to discrete auroral arcs, J. Geophys. Res., 81, 3999-4003, 1976.

Kan, J.R., and S.-I. Akasofu, Energy source and mechanism for accelerating the electrons and driving the field-aligned currents of the discrete auroral arc, J. Geophys. Res., 81, 5123-5130, 1976.

Kindel, J.M., and C.F. Kennel, Topside current instabilities, J. Geophys. Res., 76, 3055-3078, 1971.

Lassen K. and C. Danielsen, Quiet time pattern of auroral arcs for different directions of the interplanetary magnetic field in the Y-Z plane, J. Geophys. Res., 83, 5277-5284, 1978.

Maynard, N.C., A. Bahnsen, P. Christophersen, A. Egeland, and R. Lundin, An example of anticorrelation of auroral particles and electric fields, J. Geophys. Res., 78, 3976-3980, 1973.

Mozer, F.S., Origin and effects of electric fields during isolated magnetospheric substorms, J. Geophys, Res., 76, 7595-7608, 1971.

Mozer, F.S., and U.V. Fahleson, Parallel and perpendicular electric fields in an aurora, Planet. Space Sci., 18, 1563-1571, 1970.

Newton, R.S., D.J. Southwood, and W.J. Hughes, Damping of geomagnetic pulsations by the ionosphere, Planet. Space Sci., 26, 201-209,1978

Nishida, A., Geomagnetic diagnosis of the magnetosphere, J.G. Roederer(ed.), Springer-Verlag, New York, 1978.

Ogawa, T., H. Mori, and S. Miyazaki, Electron density and temperature profiles in the antarctic auroral ionosphere observed by sounding rockets, J. Radio Research Laboratories, 25, 73-94, 1978.

Ogawa, T., and T. Sato, New mechanism of auroral arcs, Planet. Space Sci., 19, 1393-1412, 1971.

Oguti, T., Observations of rapid auroral fluctuations, J. Geomag. Geoelectr., 30, 299-314, 1978.

Papadopoulos, K., A review of anomalous resistvity for the ionosphere, Rev. Geophys. Space Phys., 15, 113-127, 1977.

Park, R.J. and P.A. Cloutier, Rocket-based measurement of Birkeland currents related to an auroral arc and electrojet, J. Geophys. Res., 7714-7733, 1971.

Paulikas, G.A., The patterns and sources of high-latitude particle precipitation, Rev. Geophys. Space Phys., 9, 659, 1971.

Pazich, P.M. and H.R. Anderson, Rocket measurements of auroral electron fluxes associated with field-aligned currents, J. Geophys. Res., 80, 2152-2160, 1975.

Peacemen, D.W. and H.H. Rachford Jr., The numerical solution of parabolic and elliptic differential equations, J. Soc. Ind. and Appl. Math. 3, 28-41, 1955.

Potter, D., Computational physics, John Wiley & Sons, 1973.

Rees, M.H., Auroral electrons, Space Sci. Rev., 10, 413, 1969.

Rudakov L.I. and R.Z. Sagdeev, On the instability of a nonuniforn rarefied plasma in a strong magnetic field, Soviet Physics-Doklady, 6, 415-417, 1961.

Sato, T., A theory of quiet auroral arcs, J. Geophys. Res., 83, 1042-1048, 1978.

Sato, T., and T.E. Holzer, Quiet auroral arcs and electrodynamic coupling between the ionosphere and the magnetosphere, I.J. Geophys, Res., 78, 7314-7329, 1973.

Sato. T., and H. Okuda, Ion acoustic double layers, preprint, Plasma Physics Laboratory, Princeton University, 1979.

Sesiano, J., and P.A. Cloutier, Measurements of field-aligned currents in a multiple auroral arc system, J. Geophys. Res., 81, 116-122, 1976.

Smith, G.D., Numerical solution of partial differential equations, Oxford University Press, 1965.

Spiger, R.J., and H.R. Anderson, Electron currents associated with an auroral band, J. Geophys. Res., 80, 2161-2164, 1975.

Swift, D.W., A mechanism for energizing electrons in the magnetosphere, J. Geophys. Res., 70, 3061-3174, 1965.

Swift, D.W., Turbulent generation of electrostatic fields in the magnetosphere, J. Geophys. Res., 82, 5143-5154, 1977.

Tamao, T., The structure of three-dimensional hydromagnetic waves in a uniform cold plasma, J. Geomag. Geoelec., 16, 89-114, 1964

Vondrak, R.R., H.R. Anderson, and R.J. Spiger, Rocket-based measurement of particle fluxes and currents in an auroral arc, J. Geophys. Res., 76, 7701-7713, 1971.

Wescott, E.M., J.D. Stolarik, and J.P. Heppner, Electric fields in the vicinity of auroral forms from motions of barium vapor releases, J. Geophys. Res., 74, 3469, 1969.

Westerlund, L.H., The auroral electron energy spectrum extended to 45 eV, J. Geophys. Res., 74, 351-354, 1969

Table captions

Table 1. Summary of the important observational results by the rocket-borne experiments of the Rice university group.

Table 2. Physical and numerical constants for simulation runs

Table 3. Physical parameters for simulation runs

	Park and Cloutier [1971]	Casserly and Cloutier [1975]	Sesiano and Cloutier [1976]
Condition	Quiet		$K_p = 2_+$
Meridional Electric field (mV/m)			15
Unperturbed Current	Westward		
Number of Arcs	1	Multiple	Multiple
Arc Width (km)	16	36	10 - 30
Arc Spacing (km)			20 - 40
Electrojet Intensity (A)	6×10^3	1. 3×10^3 2. 4×10^3	$10^3 \sim 2 \times 10^3$
Electrojet Direction		Eastward × 2	Eastward × 2 Eastward × 1
F.A. Current Density ($\mu A/m^2$)	20	23 ↓ 33 ↑	10 ∿ 90
Current Sheet Intensity (A/m)	0.16		0.08
Coincidence of J↑ with Visual Arcs	YES	YES	YES
Coincidence of J↑ with Electrojet	YES		YES
Coincidence of J↑ with Downward Electrons	YES	YES	
Major Carrier of $J_{\parallel}$		< 0.5 keV Electrons	

Table 1

Constant	R_E km	r km	h km	Δ km	θ_{max} rad	θ_{min} rad	$\bar{\theta}$ rad	$\Delta\theta$ rad	T_o SEC	
Equation		(B.3)	(1)	(12)			(13)	(13)		
	6370	6480	20	50	$\frac{23}{180}\pi$	$\frac{20}{180}\pi$	$\frac{21.5}{180}\pi$	$\frac{0.03}{180}\pi$	20.2	
Constant	α m^3S^{-1}	α' m^3S^{-1}	M_H $m^2S^{-1}V^{-1}$	M_p $m^2S^{-1}V^{-1}$	B_o G	γ_o	j_{cr} μAm^{-2}	Δj μAm^{-2}	J_{max} μAm^{-2}	V_o kV
Equation	(1)	(B.9)	(3)	(3)	(3)	(7)	(7)	(7)	(10)	(11)
	3.0×10^{-13}	5.0×10^{-12}	2×10^4	10^4	0.5	10.0	-1.5	0.05	1.0	50.0

Table 2

Run	$N_{midnight}$ m^{-3}	N_{noon} m^{-3}	ℓ R_E	V_A $kmSEC^{-1}$	τ_b^* SEC	Figure
1	4×10^{10}	4×10^{11}	10.6	2000	137	4-7, 19, 20, 21
2	4×10^{10}	10^{11}	10.6	2000	137	22
3	10^{10}	10^{11}	10.6	2000	137	8-10, 20, 21, 22
4	10^{10}	10^{11}	21.2	2000	275	13-15, 20, 22
5	10^{10}	10^{11}	10.6	1500	183	16-18, 20, 22
6	5×10^{9}	10^{11}	10.6	2000	137	11-12, 20, 22

* Bounce time of the Alfvén wave

Table 3

Figure Captions

Fig. 1. The left panel: Frequency of auroral appearances in zenith in coordinates ϕ' and local time, for the period 1957 - 59, in the northern hemisphere, in the course of day-to-day observations. Numbers denote the frequency of auroral appearances in percentages [from Feldstein, 1966]. The right panel: A summary of the distribution and flow directions of large-scale field-aligned currents determined from data obtained on 493 passes of Triad during weakly disturbed conditions ($|AL| < 100\ \gamma$). The 'hatched' area shown between 1130 and 1230 MLT in the polar cusp region indicates that the current flow directions are often confused [from Iijima and Potemra, 1976 a]. Note that a good spatial coincidence between the so-called auroral oval (hatched area in the left panel) and the region of large-scale Birkeland current flows (right panel).

Fig. 2. Electric field vectors at auroral latitudes for three different days, plotted in invariant latitude-magnetic local time coordinates K_p indices are 2, 4-, and 5 at 2400 - 0300 (UT) from the left [from Horwitz et al., 1978].

Fig. 3. A schematic view of the background distribution of large-scale electric fields in the auroral oval and their spatial relationship with the large-scale field-aligned current.

Fig. 4. Height-integrated current distributions at auroral latitudes for the same three disturbed days as shown in Fig. 2. Local midnight is located near at 1100 UT in these panels. [from Horwitz et al., 1978].

Fig. 5. Local time distribution of height-integrated Hall (plus) and Pedersen (square) conductivities in the auroral region ionosphere for a quiet day (upper panel). Conductivity ratio Σ_H/Σ_p vs. local

time; the ratio is almost constant and nearly equal to 2 for almost all local times in the auroral region ionosphere (lower panel) [Brekke et al., 1974].

Fig. 6. Comparison of critical current profiles and field-aligned currents. Represented by solid curves are the critical current for the O^+ cyclotron wave assuming the plasma were O^+ (lowest solid curve), the pure H^+ cyclotron wave (middle solid curve), and the ion acoustic wave (top solid curve). T_e/T_i was chosen to 1. The dotted lines represent the current densities for total field-aligned current fluxes (at 200 km) of 10^8, 10^9, 10^{10} and 10^{11} electrons/cm^2sec as a function of height assuming $L \simeq 8$ and that the current is conserved. For this ionosphere, 10^8 el $cm^{-2}s^{-1}$ is stable, 10^9 el $cm^{-2}s^{-1}$ excites cyclotron waves, 10^{10} el $cm^{-2}s^{-1}$ may excite ion acoustic waves. As the current increases, the unstable region moves to lower altitude. [from Kindel and Kennel (1971)].

Fig. 7. Physical picture of the ionosphere-magnetosphere feedback instability. The left side corresponds to the north, and the magnetic field is downward. For the feedback instability to occur, namely, for downward electron fluxes and upward electron fluxes to coincide with a peak and a valley of the density disturbance δn, respectively, it is required that the magnetosphere respond to the ac potential perturbation (see from the reference system moving with the field lines) at the foot of the field line as an inductive load (middle portion of this figure).

Fig. 8. Schematic representation of a numerical model of the auroral oval with a latitudinal range 67° - 70° and with a large-scale ambient field-aligned current distribution described by (10) [cf.

Iijima and Potemra, 1976 b, Figure 6].

Fig. 9. Ambient horizontal current distribution (left panels) and electric ($\vec{E} \times \vec{B}$) drift velocity distribution (right panels) in the ionosphere calculated for the field-aligned current model given by (4.26) and a denser ionospheric model with $N_{midnight} = 4 \times 10^{10} m^{-3}$ and $N_{noon} = 4 \times 10^{11} m^{-3}$ (upper two panels) and for the same ambient field-aligned current distribution and $N_{midnight} = 10^{10} m^{-3}$ and $N_{noon} = 10^{11} m^{-3}$ (lower two panels). Represented by the unit arrows below the polar plots are the height integrated current of 1 A/m (left panels) and the electric drift of 4 km/sec (right panels), which corresponds to the electric field of 200 mV/m. The current and electric drift vectors direct antisunward and sunward, respectively. Note particularly in the upper left panel that the current vector takes the largest value at the higher-latitude portion on the dusk side.

Fig. 10. Temporal evolutions of the peak amplitudes of the density (solid line), the field-aligned current (dotted line), and the potential (dot-dash) disturbances, for the ambient ionospheric model shown in the upper two panels of Figure 9, $\ell = 10.6\ R_E$ and $V_A = 2000$ km/s, corresponding to the bounce time of the Alfvén wave ($4\ell/V_A$) of 137 s. Time is normalized by 20.2 s. Note that the density disturbance (solid line) grows rapidly when the field-aligned current disturbance reaches about 1 $\mu A/m^2$ and the precipitation of hot electrons begins. The dashed horizontal line represents a saturation level of the density disturbance $n_{sat} (>> n_o)$ determined by $\gamma_{gr} \tilde{n}_{sat} = \alpha \tilde{n}^2_{sat}$, where γ_{gr} is a growth rate calculated from the slope of the density evolution following the precipitation of hot electrons.

Fig. 11. Sequential contour plots of the density (top three panels), the field-aligned current (middle three panels) and the potential (bottom three panels) disturbances in the growing phase in Figure 10. Since these contours are drawn after normalizing the amplitudes by their peak values, they to not reflect the actual size of the auroral arcs. Note a marked contrast in their evolution between the day sector and the night sector and another contrast between the dawnside and the duskside.

Fig. 12. Sequential contour plots of auroral electron fluxes, i.e., contours of $j_h (< 0)$ carried by auroral electrons in the growing phase in Figure 10 (upper three panels), the ionospheric current distribution (lower left panel), and the electric drift velocity distribution (lower right panel) at T = 30. Since these contours cover the whole range of j_h from zero to its peak value by five contour lines, they are considered to reflect the real size of the optical aurora caused by precipitation of auroral electrons. Note a development of auroral electrojets (north-eastward) in the evening sector and a reduction of the latitudinal electric field component inside auroral arcs.

Fig. 13. Sequential latitudinal profiles of the density (solid line in both panels), the potential (dotted line in the left panel), and the field-aligned current (dotted line in the right panel) disturbances in the growing phase in Figure 10 at 2200 LT. Field-aligned current is defined as negative for the upward current. Note a good coincidence of the spatial relationship among the disturbances with that inferred from the physical intuition shown in Figure 7.

Fig. 14. Same as Figure 10 but for a different ionospheric model with $N_{midnight} = 10^{10} m^{-3}$ and $N_{noon} = 10^{11} m^{-3}$, the electric drift and

current distributions of which are shown in the lower two panels of Figure 9. Note the much faster evolution of the disturbance than that in Figure 10 and much larger amplitudes of the disturbance at the final state than those in Figure 10.

Fig. 15. Same as Figure 12 but for the growing phase in Figure 14. Note the appearance of auroral arcs on the dawnside as well as on the duskside, this being a remarkable difference from Figure 12. Auroral electrojets (eastward on the duskside and southwestward on the dawnside) develop much more intensely than those in Figure 12.

Fig. 16. Latitudinal profiles of the density (solid line in both panels), the potential (dotted line in the upper panel), and the field-aligned current (dotted line in the lower panel) disturbances at 2200 LT at T = 30. Note much more pronounced disturbances than those in Figure 13 (the scale is different from that of Figure 13).

Fig. 17. Same as Figure 10 but for different ionospheric model with $N_{midnight} = 5 \times 10^{9} m^{-3}$ and $N_{noon} = 10^{11} m^{-3}$.

Fig. 18. Same as Figure 16 but for the disturbance at 2200 LT and T = 30 in Figure 17. Note that an extra broad faint arc which did not appear in Figure 16 appears in the polemost region of the arc system.

Fig. 19. Same as Figure 14 but for a different magnetospheric model with $\ell = 21.2\ R_E$ and $V_A = 2000$ km/s, corresponding to the bounce time of the Alfvén wave of 275. Note that the development of the disturbances is slower than that of Figure 14 and amplitudes of the disturbance are smaller than those in Figure 14 at the final state.

Fig. 20. Same as Figure 15 but for the growing phase in Figure 19. Note that the arc width is broader than that in Figure 15 and auroral electrojets do not deve p so markedly as those in Figure 15.

Fig. 21. Latitudinal profiles of the density (solid line) and the field-aligned current (dotted line) disturbances at 2200 LT and T = 30 in Figure 19. Note that the arc width of the most developed arc is about 27 km in this model, being nearly twice as large as that in Figure 16.

Fig. 22. Same as Figure 14 but for different magnetospheric model with $\ell = 10.6\ R_E$ and $V_A = 1500$ km/sec, corresponding to the bounce time of the Alfvén wave of 183 sec.

Fig. 23. Same as Figure 15 but for the growing phase in Figure 22.

Fig. 24. Same as Figure 21 but for the disturbance at T = 30 in Figure 22. Note that the arc widths are slightly larger than those in Figure 16, though not so remarkable as Figure 21.

Fig. 25. A dynamic view of the density disturbance at 2200 LT for parameters of $N_{midnigh} = 4 \times 10^{10} m^{-3}$, $N_{noon} = 4 \times 10^{11} m^{-3}$, $\ell = 10.6\ R_E$, and $V_A = 2000$ km/sec, corresponding to the bounce time of the Alfvén wave of 137 sec (cf. Figure 13). Note that the density enhancement becomes almost stationary in the final phase.

Fig. 26. Plot of the latitudinal position of the initial density peak at 2200 LT versus time for different ionospheric ambient electron density distributions (left panel) and for different magnetospheric impedances (right panel). In the left panel the dotted, the solid, and the dot-dash curves represent the plot for $N_{midnight} = 4 \times 10^{10} m^{-3}$ and $N_{noon} = 4 \times 10^{11} m^{-3}$, $N_{midnight} = 10^{10} m^{-3}$ and $N_{noon} = 10^{11} m^{-3}$, and $N_{midnight} = 5 \times 10^{9} m^{-3}$ and $N_{noon} = 10^{11} m^{-3}$, respectively, the magnetospheric parameters being the same for these plots ($\ell = 10.6\ R_E$ and $V_A = 2000$ km/s). In the right panel the dotted, the solid, and the dot-dash curves represent the plot for $\ell = 21.2\ R_E$ and $V_A = 2000$km/sec,

ℓ = 10.6 R_E and V_A = 2000 km/s, and ℓ = 10.6 R_E and V_A= 1500 km/s, the ionospheric electron density distribution being the same for these plots ($N_{midnight} = 10^{10} m^{-3}$ and $N_{noon} = 10^{11} m^{-3}$); τ_b is the bounce time of the Alfvén wave ($4\ell/V_A$). Note that regardless of the ionospheric and the magnetospheric parameters, the velocity of auroral arcs in the north-south direction becomes almost zero in the final saturation stage.

Fig. 27. Perspective views of the density disturbance at the saturation stage for two different ambient ionospheric electron density distributions, upper and lower panels corresponding to Figure 12 and Figure 15, respectively. Note the remarkable difference between the two panels, indicating the strong dependence of the arc development on the ambient electron density distribution in the ionosphere. Note that no perturbation grows in the day sector.

Fig. 28. Peak amplitudes of the density (cross), the potential (triangle) and the field-aligned current (circle) disturbances at T = 32 for the fixed parameters of $N_{noon} = 10^{11} m^{-3}$, ℓ = 10.6 R_E, and V_A = 2000 km/sec as a function of $N_{midnight}$ (left panel). The same plot as the left panel but for the fixed ionospheric electron density distribution of $N_{midnight} = 10^{10} m^{-3}$ and $N_{noon} = 10^{11} m^{-3}$, as a function of the bounce time of the Alfvén wave (right panel), the arc width at T = 32 being plotted by a square. Note in both panels that the field-aligned current disturbance is the most variable quantity among the three disturbances. Note furthermore in the right panel that the arc width increases with the bounce time of the Alfvén wave.

Figure Captions in Appendices

Fig. A.1. A coordinate system adopted in the energy consideration of the feedback instability. The magnetic field is assumed to be straight and homogeneous.

Fig. A.2. In the limit of $\gamma \to 0$, $\mathrm{Re}(\omega_M)$ is determined from the intersection of two curves as denoted by circle. Note that for sufficiently large values of $\mu_o V_A \Sigma_p / 2\alpha n_o$, $\mathrm{Re}(\omega_M)$ is nearly equal to $\pi V_A/(2\ell)$.

Fig. C.1. (a) A rectangular region R defined by $x_1 \le x \le x_M$, $y_1 \le y \le y_N$, where the solution of the boundary value problem (C.1) - (C.3) is to be sought.

(b) The rectangular region R is approximated by a finite difference mesh system composed of M × N meshes denoted by circle (M meshes in the x direction and N meshes in the y direction).

Fig. C.2. (a) A mnemonic diagram of the five-point difference approximation of the elliptic equation expressed by (C.5).

(b) A mnemonic diagram of the five-point difference approximation of the boundary condition expressed by (C.8). Note that on the boundary, above two mnemonic representations include 'virtual mesh' or 'virtual potential', which belongs exterior to the region R. The virtual mesh must be removed by combining (C.5) and (C.8).

Fig. C.3. (a) Mesh system for a boundary condition in case (a). Since the periodic condition is imposed in both directions, the five-point difference approximation of the elliptic equation (C.5) includes essentially no virtual meshes exterior to the region R and the potentials with i = M and j = N can be replaced by equivalent potentials with i = 1 and j = 1.

(b) Mesh system for a boundary condition expressed by IBCX = 1 and IBCY = 2. Since the mixed boundary condition (C.2) is imposed in the x direction, virtual meshes or virtual potentials denoted by

cross are necessary for keeping the second order accuracy of the difference approximation in the entire region inside R.

(c) Mesh system for a boundary condition in case (c). Since the mixed boundary condition is imposed along the entire boundary in x and y directions, virtual meshes are necessary so as to surround the whole region as denoted by cross. Note especially that at each corner of the rectangular region R, the linear equations (C.5) and (C.8) include two virtual meshes.

Fig. C.4. (a) A resultant mesh system after removing the equivalent meshes using the periodic boundary condition (C.3). In this case there is $(M - 1) \times (N - 1)$ unknown potentials at discretized mesh points denoted by arcle.

(b) A resultant mesh system for case (b) after removing the virtual meshes in Fig. C.3-b from (C.23) and (C.24). In this case there is $M \times (N - 1)$ unknown potentials at discretized mesh points denoted by circle.

(c) A resultant mesh system after removing the virtual meshes in Fig. C.3-c by combining (C.5) and (C.8). In this case there is $M \times N$ unknown potentials at discretized mesh points denoted by circle.

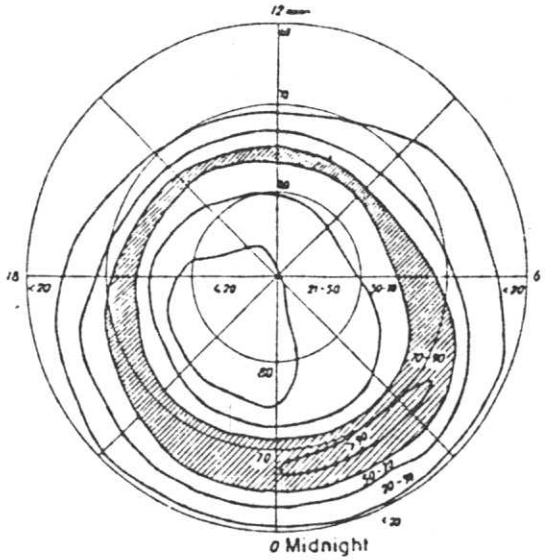

FIG. 2. FREQUENCY OF AURORAL APPEARANCES IN ZENITH IN COORDINATES ϕ' AND LOCAL TIME, FOR THE PERIOD 1957–59, IN THE NORTHERN HEMISPHERE, IN THE COURSE OF DAY-TO-DAY OBSERVATIONS. NUMBERS DENOTE THE FREQUENCY OF AURORAL APPEARANCES IN PERCENTAGES.

[Feldstein, 1966]

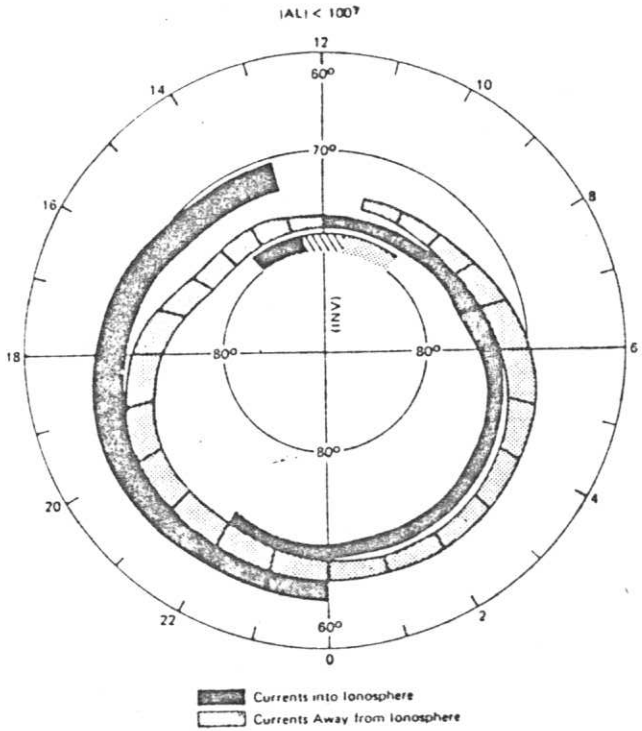

Fig. 6. A summary of the distribution and flow directions of large-scale field-aligned currents determined from data obtained on 493 passes of Triad during weakly disturbed conditions ($|AL| < 100\ \gamma$). The 'hatched' area shown between 1130 and 1230 MLT in the polar cusp region indicates that the current flow directions are often confused.

[Iijima and Potemra, 1976a]

Fig. 1

Fig. 2

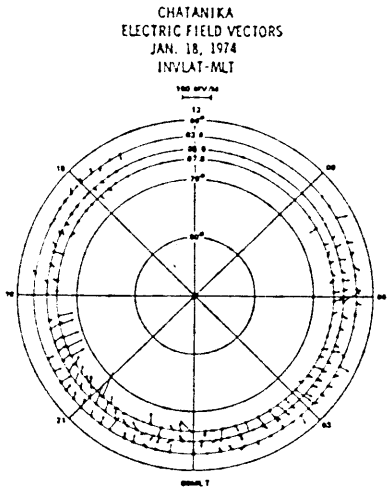

Fig. 4. Electric field vectors for January 18, 1974, plotted in invariant latitude-magnetic local time coordinates for Λ = 67.0°, 65.6°, and 63.6°. Note the Harang discontinuity slanted from northwest to the southeast near midnight.

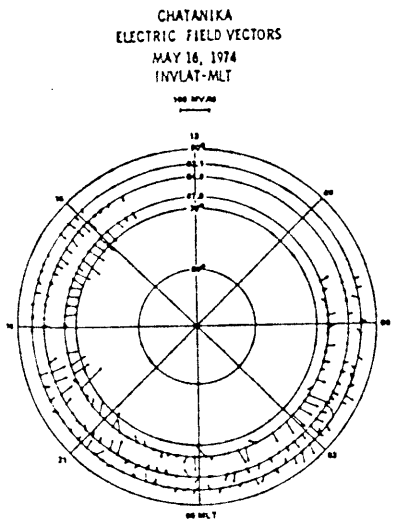

Fig. 8. Electric field vectors for May 16, 1974, plotted in invariant latitude-magnetic local time coordinates for Λ = 67.9°, 64.9°, and 63.1°.

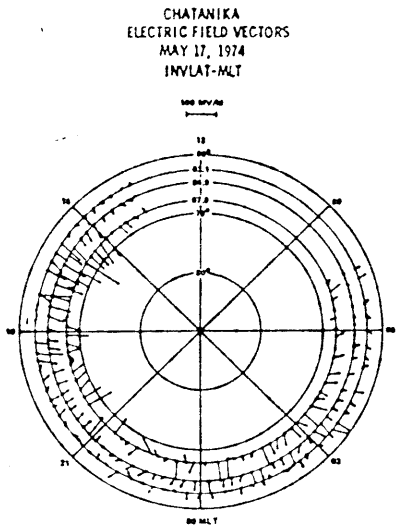

Fig. 11. Electric field vectors for May 17, 1974, plotted in invariant latitude-magnetic local time coordinates for Λ = 67.9°, 64.9°, and 63.1°.

[Horwitz et al., 1978]

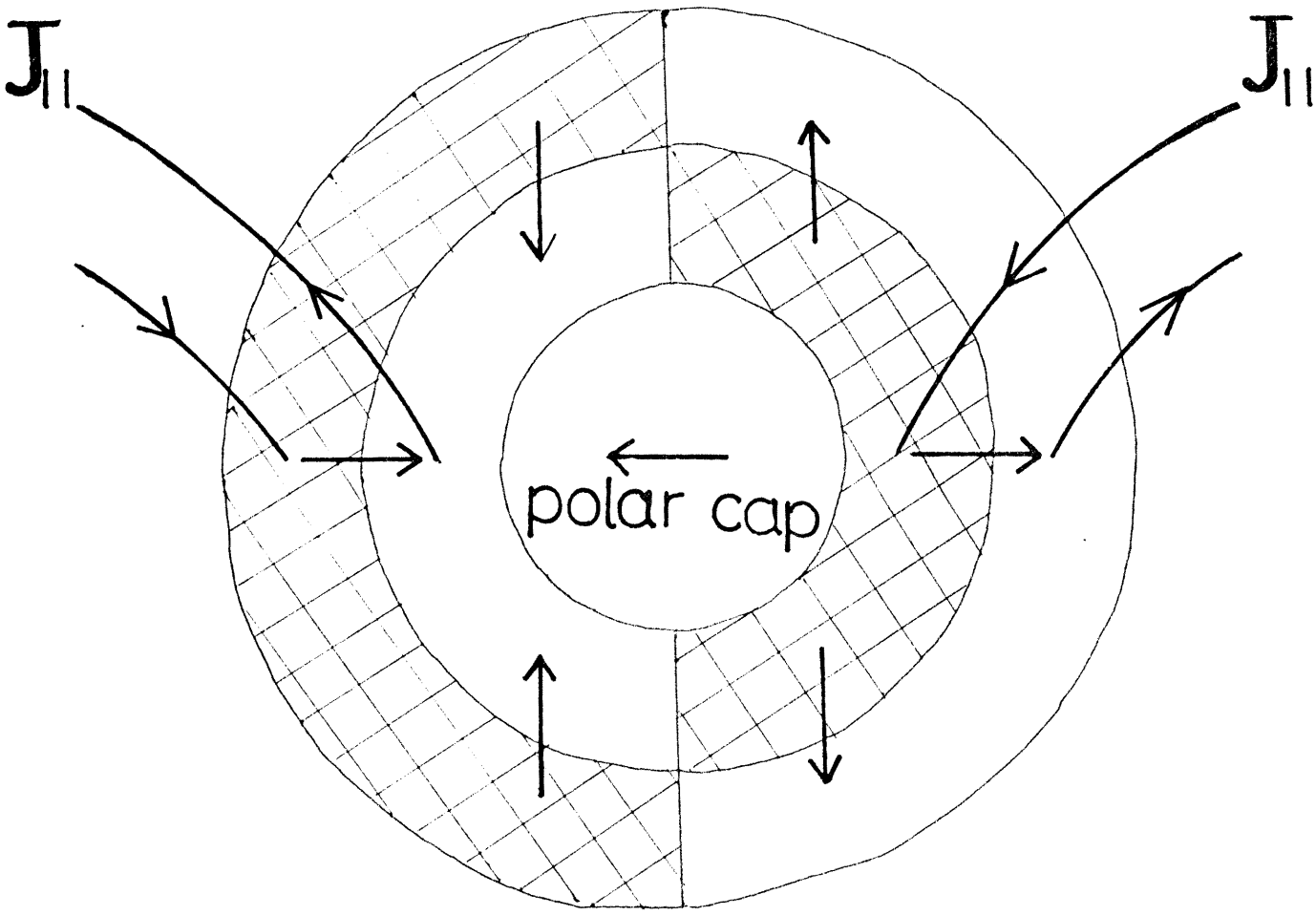
$J_{\parallel}$
$J_{\parallel}$
polar cap
Currents into Ionosphere
Electric field

Fig. 3

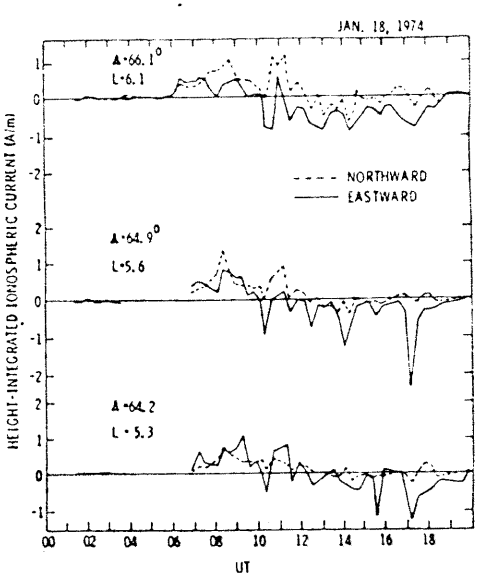

Fig. 5. Height-integrated currents for Λ = 64.2°, 64.9°, and 66.1° on January 18, 1974. Note the ~1-A/m northwestward current near midnight at 1100 UT.

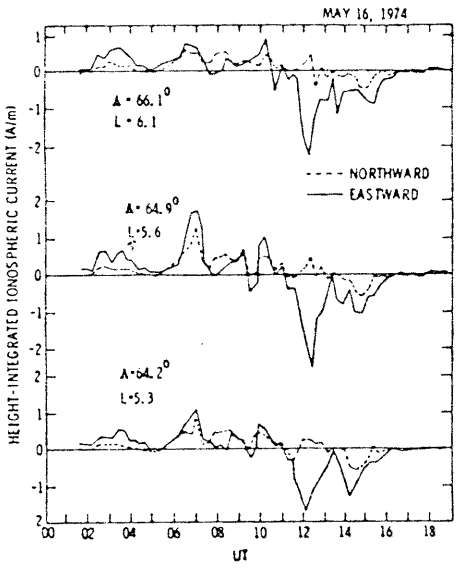

Fig. 9. Height-integrated currents at Λ = 64.2°, 64.9°, and 66.1° on May 16, 1974.

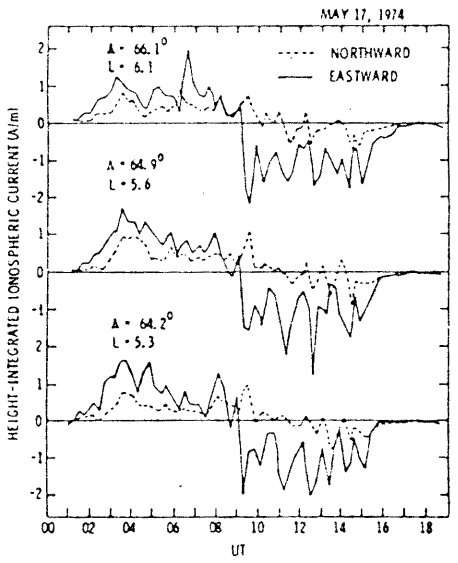

Fig. 12. Height-integrated currents at Λ = 64.2°, 64.9°, and 66.1° on May 17, 1974.

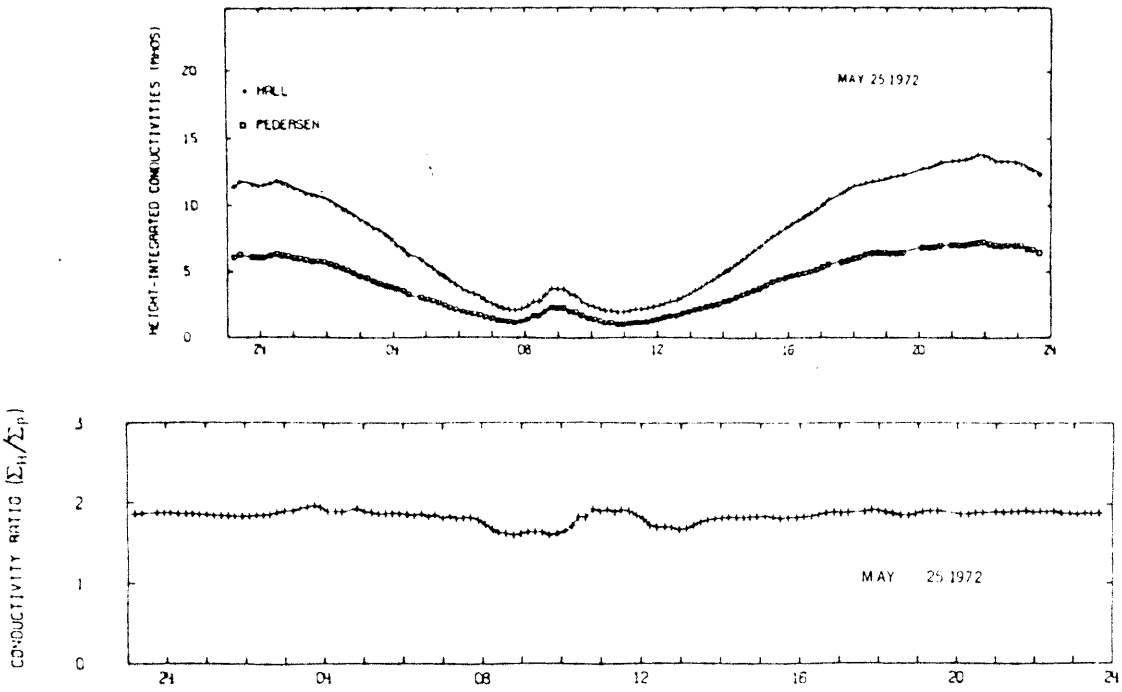
HEIGHT-INTEGRATED CONDUCTIVITIES (mhos)
HALL
PEDERSEN
MAY 25 1972
0
5
10
15
20
24
04
08
12
16
20
24
CONDUCTIVITY RATIO (Σ_H/Σ_P)
0
1
2
3
MAY 25 1972
24
04
08
12
16
20
24

Fig. 5

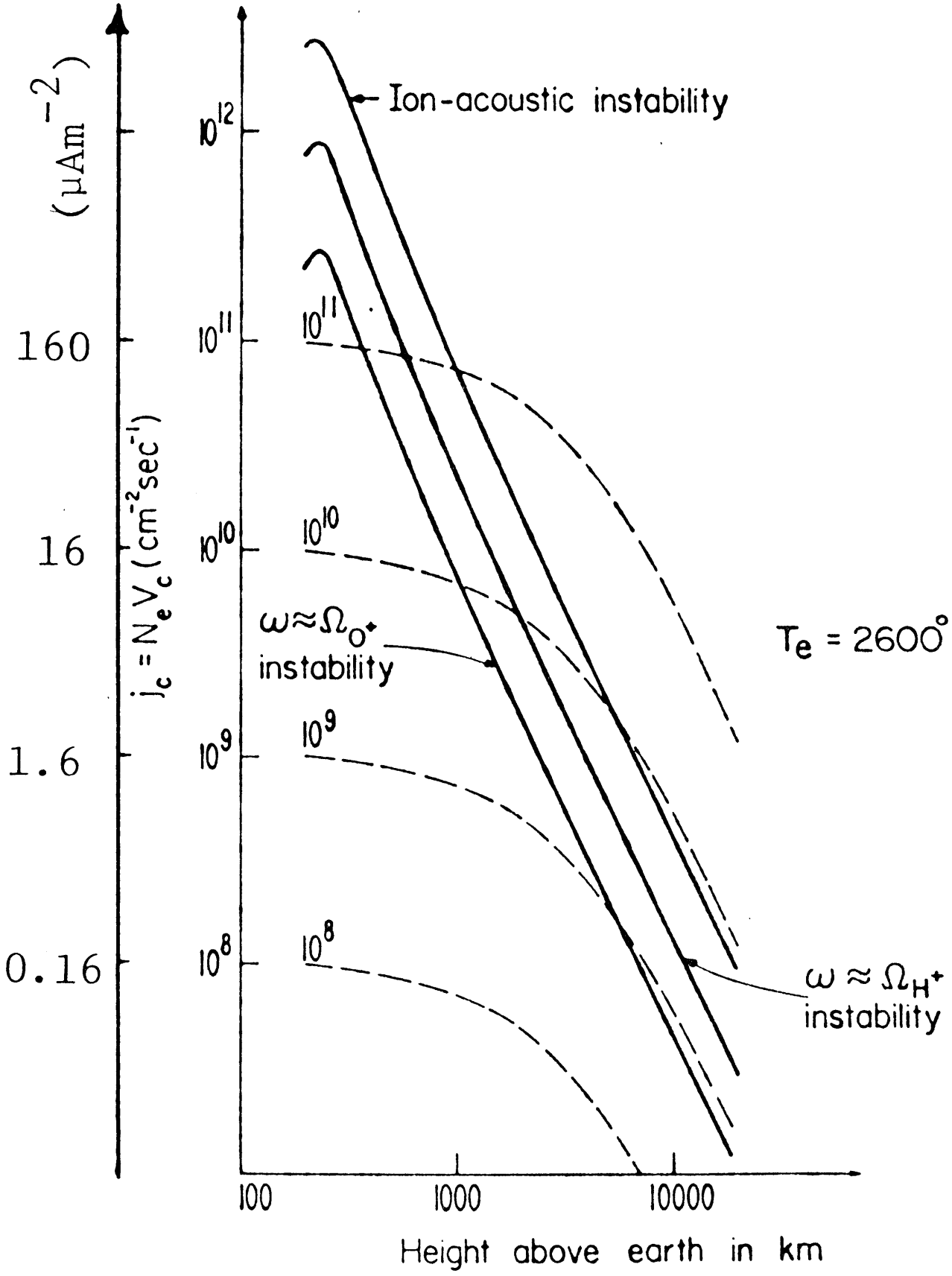
Ion-acoustic instability
10^{12}
10^{11}
10^{10}
10^{9}
10^{8}
$\omega \approx \Omega_{O^+}$ instability
$T_e = 2600°$
$\omega \approx \Omega_{H^+}$ instability
160
16
1.6
0.16
(μAm^{-2})
$j_c = N_e V_c (cm^{-2} sec^{-1})$
100
1000
10000
Height above earth in km

Fig. 6

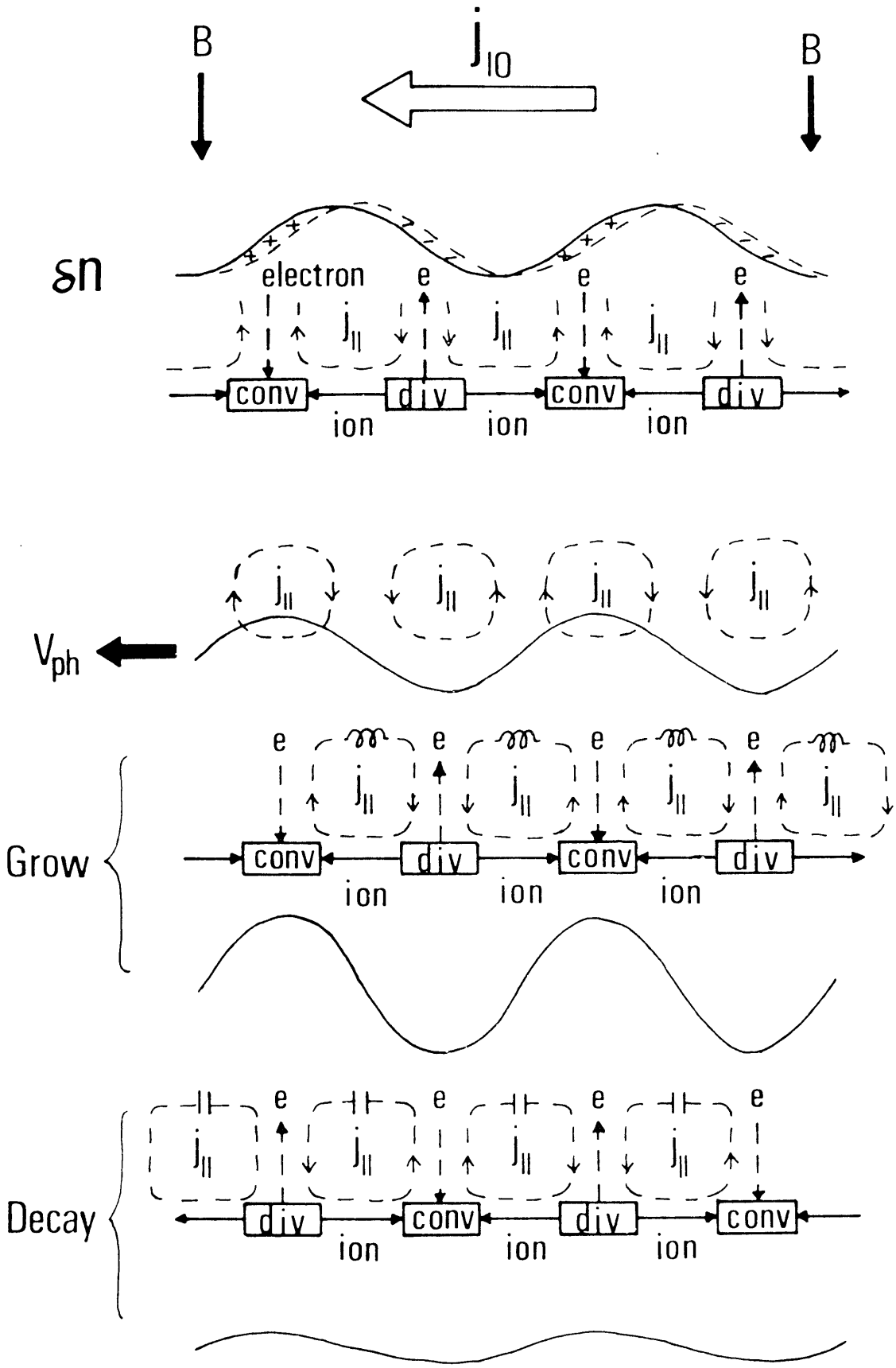
B
$j_{\parallel 0}$
B
δn
electron
e
e
e
$j_{\parallel}$
$j_{\parallel}$
$j_{\parallel}$
conv
div
conv
div
ion
ion
ion
V_{ph}
$j_{\parallel}$
$j_{\parallel}$
$j_{\parallel}$
$j_{\parallel}$
Grow
e
e
e
e
conv
div
conv
div
ion
ion
ion
Decay
e
e
e
e
div
conv
div
conv
ion
ion
ion

Fig. 7

Model A
of the Auroral Oval

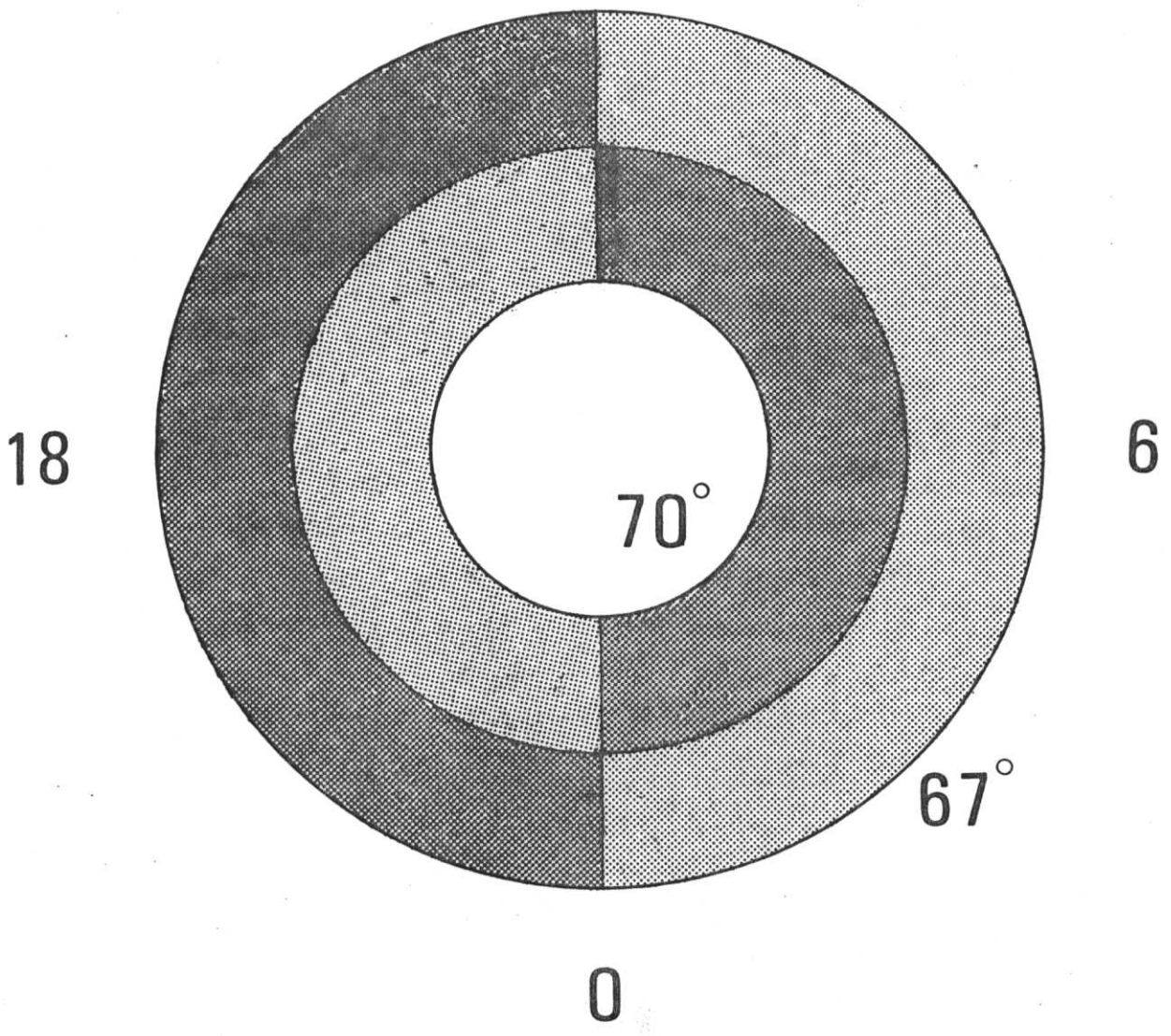

Fig. 8

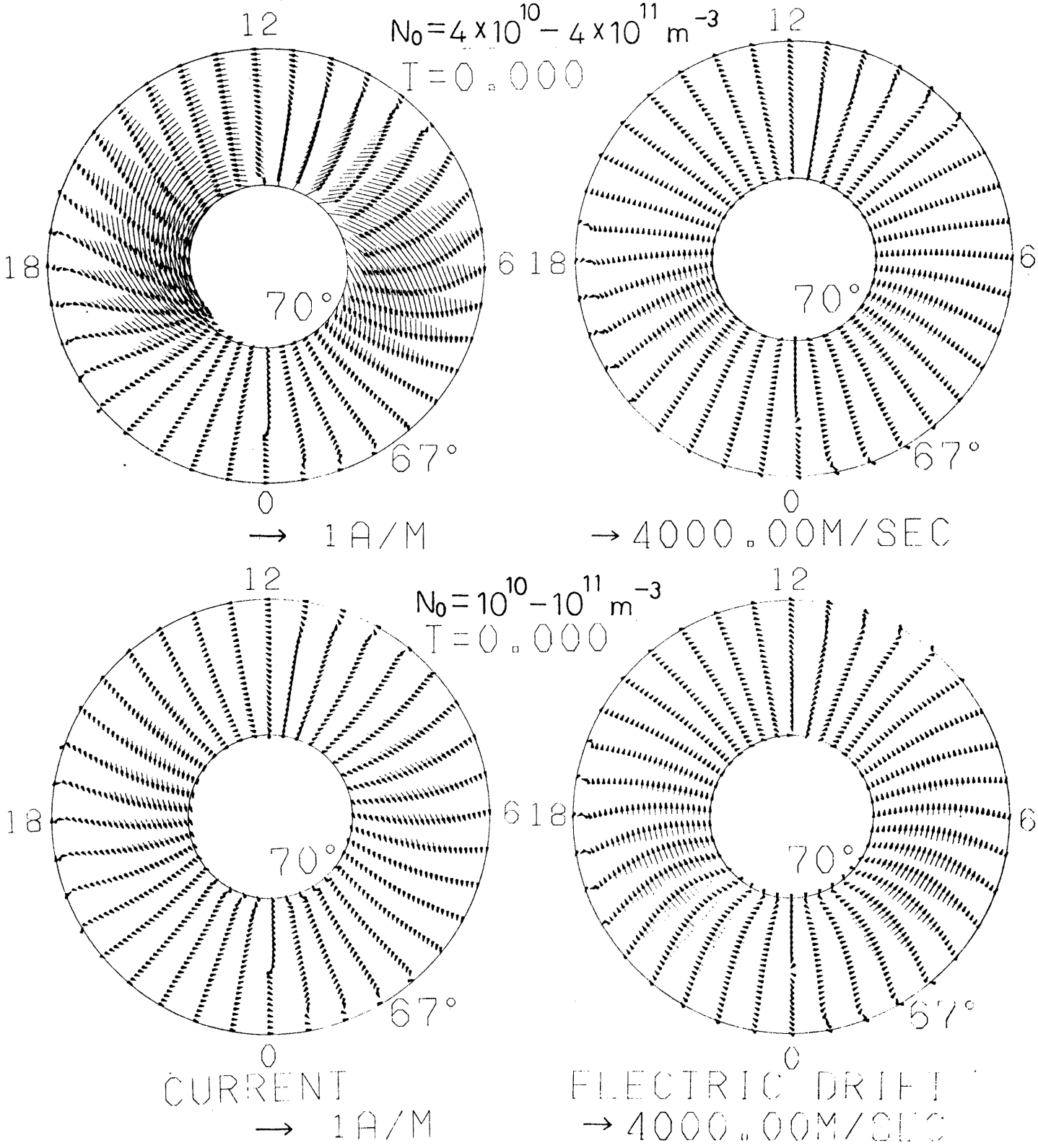
$N_0 = 4 \times 10^{10} - 4 \times 10^{11}\ m^{-3}$
T=0.000
12
18
6
0
70°
67°
→ 1A/M
→ 4000.00M/SEC
$N_0 = 10^{10} - 10^{11}\ m^{-3}$
T=0.000
CURRENT
→ 1A/M
→ 4000.00M/SEC

Fig. 9

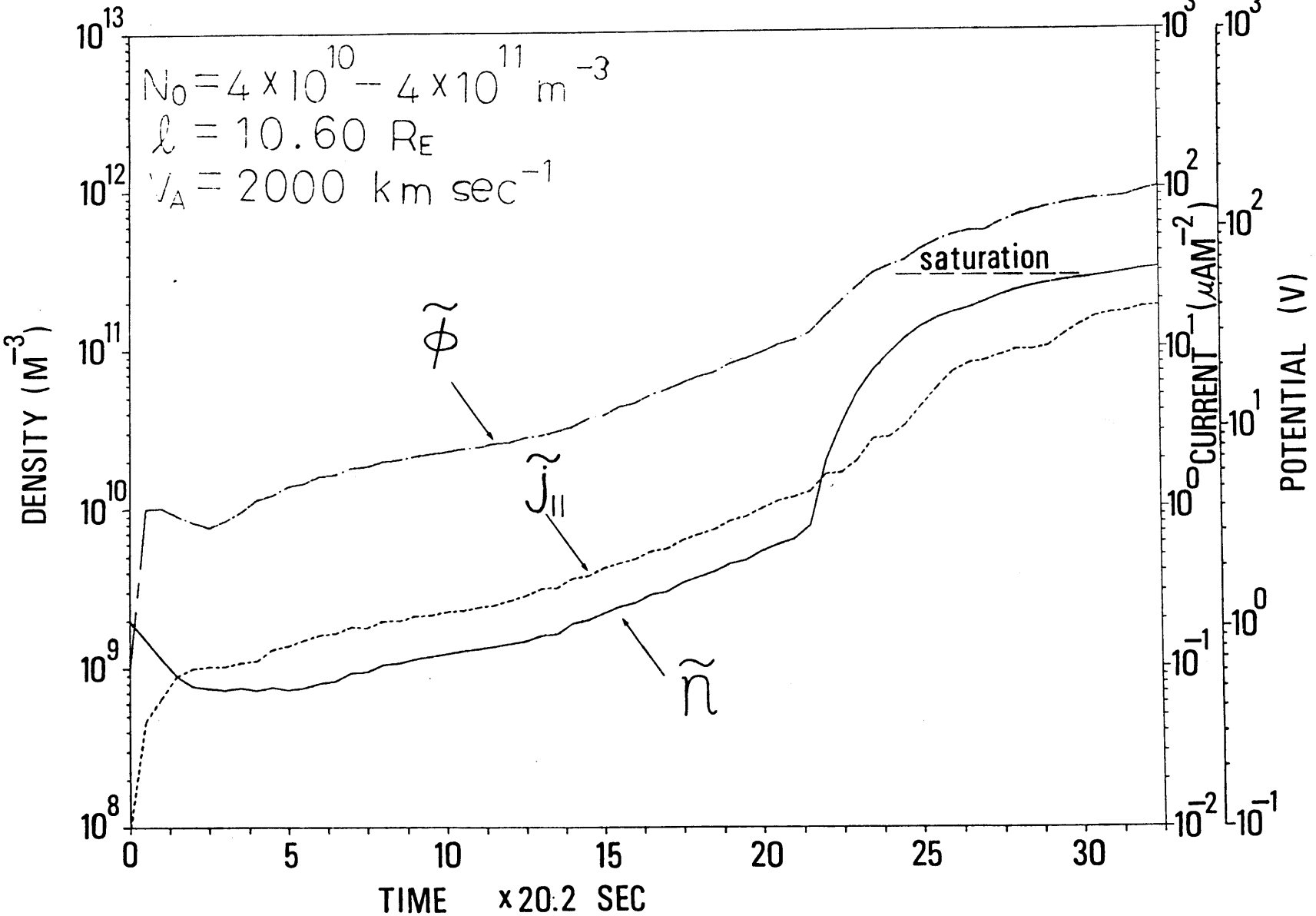
$N_0 = 4 \times 10^{10} - 4 \times 10^{11}\ m^{-3}$
$\ell = 10.60\ R_E$
$V_A = 2000\ km\ sec^{-1}$
saturation
$\tilde{\phi}$
$\tilde{J}_{||}$
$\tilde{n}$
DENSITY (M^{-3})
CURRENT (μAM^{-2})
POTENTIAL (V)
TIME x20.2 SEC
10^{13}
10^{12}
10^{11}
10^{10}
10^{9}
10^{8}
10^{3}
10^{2}
10^{1}
10^{0}
10^{-1}
10^{-2}
0
5
10
15
20
25
30

Fig. 10

$N_0 = 4 \times 10^{10} - 4 \times 10^{11}\ m^{-3}$

$L = 10.80\ R_E$

$V_A = 2000\ km\ sec^{-1}$

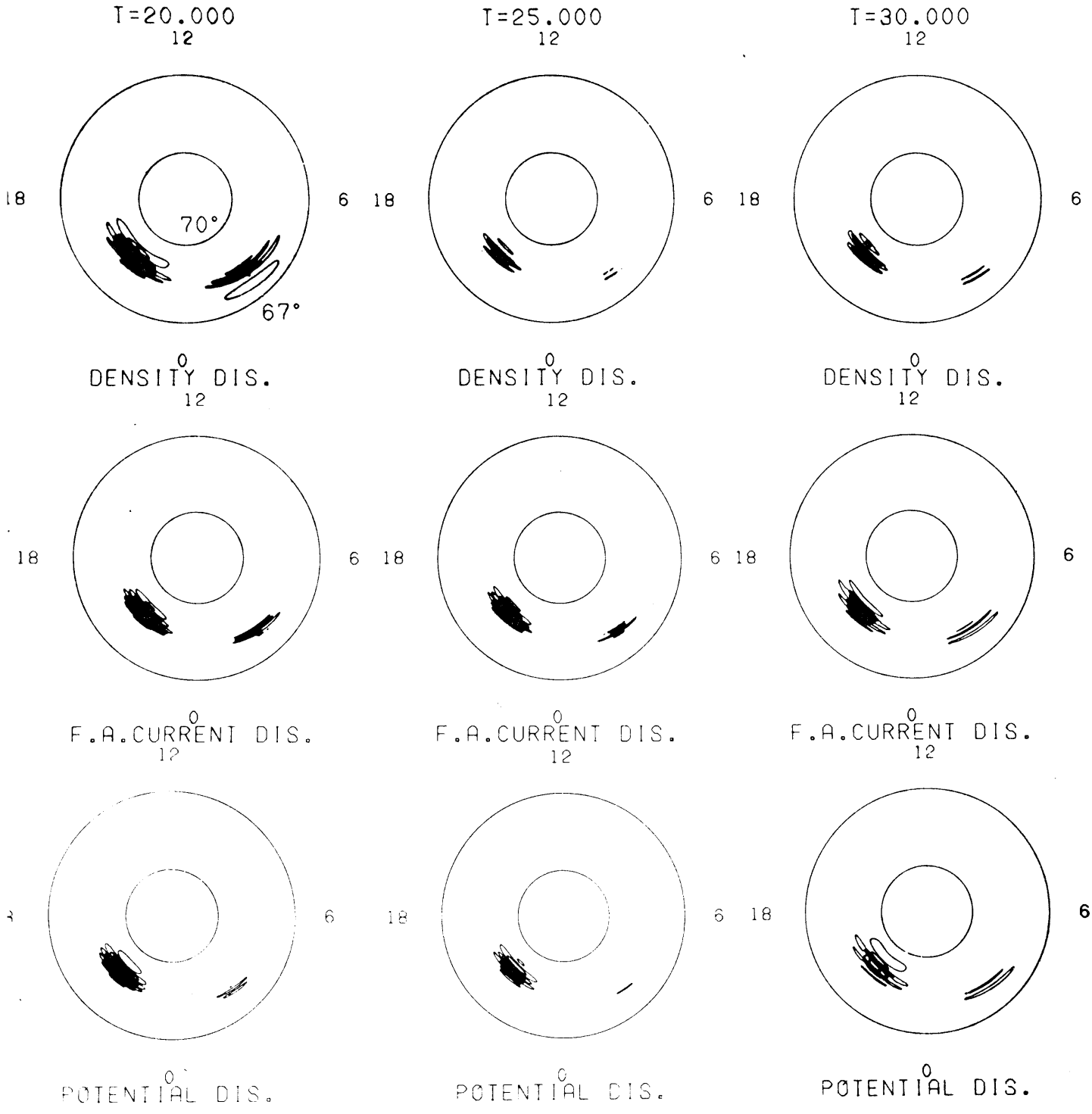

Fig. 11

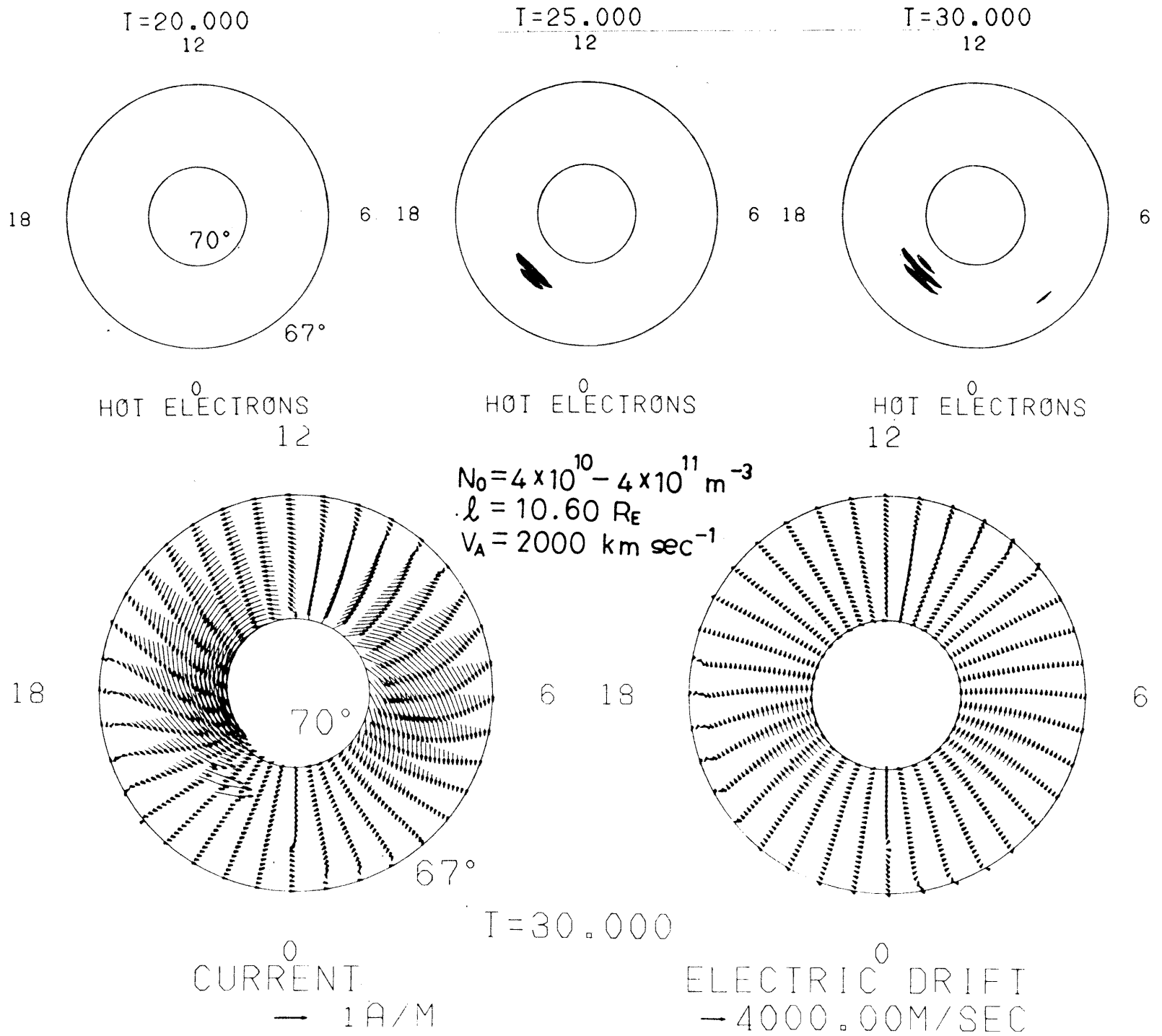
T=20.000
12
18
70°
6
67°
0
HOT ELECTRONS
T=25.000
12
18
6
0
HOT ELECTRONS
T=30.000
12
18
6
0
HOT ELECTRONS
$N_0 = 4 \times 10^{10} - 4 \times 10^{11}\ m^{-3}$
$\ell = 10.60\ R_E$
$V_A = 2000\ km\ sec^{-1}$
T=30.000
0
CURRENT
— 1A/M
0
ELECTRIC DRIFT
—4000.00M/SEC

Fig. 12

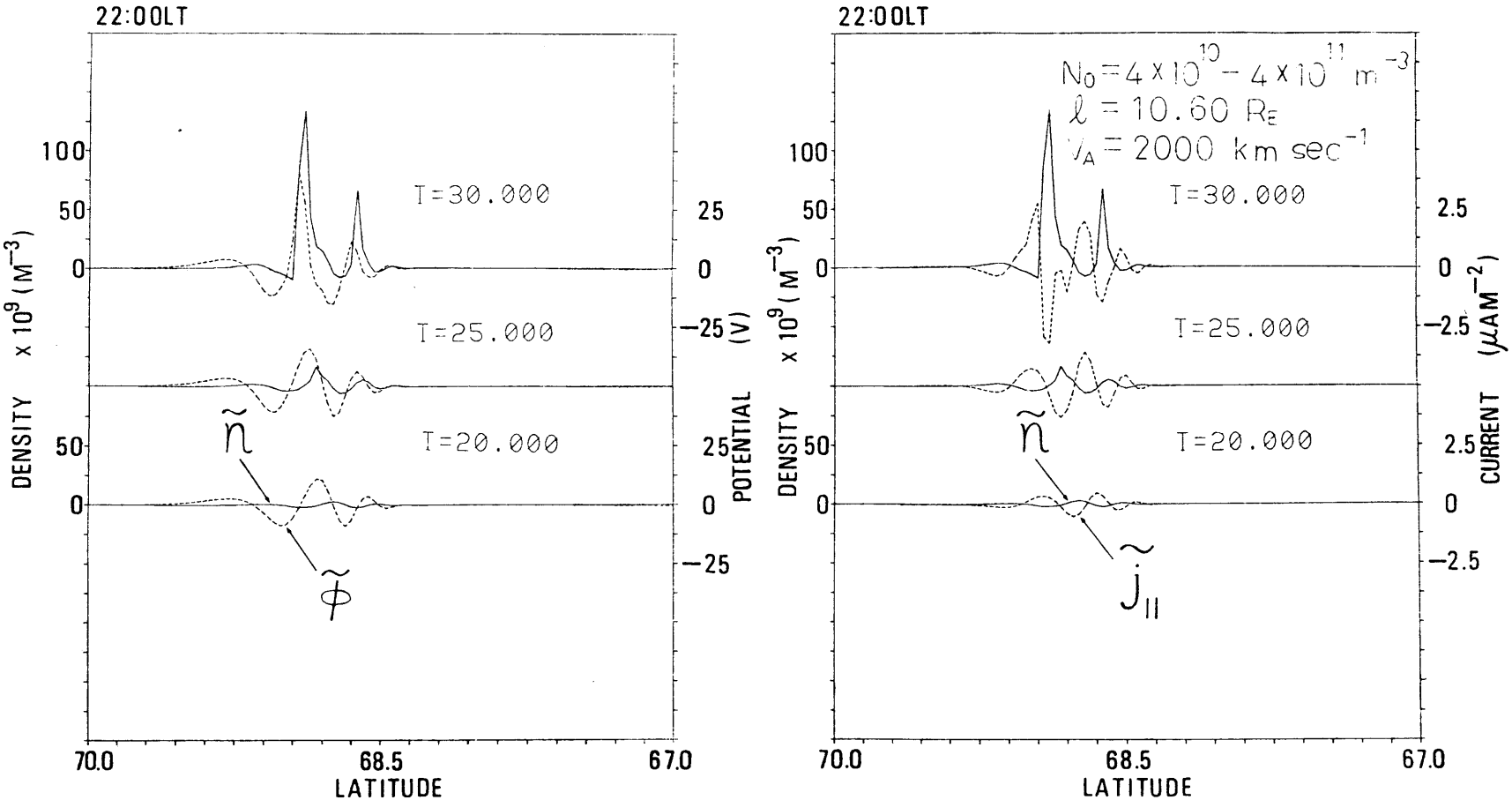
22:00LT
T=30.000
T=25.000
T=20.000
$\tilde{n}$
$\tilde{\phi}$
DENSITY x 10^9 (M^{-3})
POTENTIAL (V)
100
50
0
50
0
25
0
−25
25
0
−25
70.0
68.5
67.0
LATITUDE
22:00LT
$N_0 = 4 \times 10^{10} - 4 \times 10^{11}$ m^{-3}
$\ell = 10.60\ R_E$
$V_A = 2000$ km sec^{-1}
T=30.000
T=25.000
T=20.000
$\tilde{n}$
$\tilde{j}_{||}$
DENSITY x 10^9 (M^{-3})
CURRENT ($\mu A M^{-2}$)
100
50
0
50
0
2.5
0
−2.5
2.5
0
−2.5
70.0
68.5
67.0
LATITUDE

Fig. 13

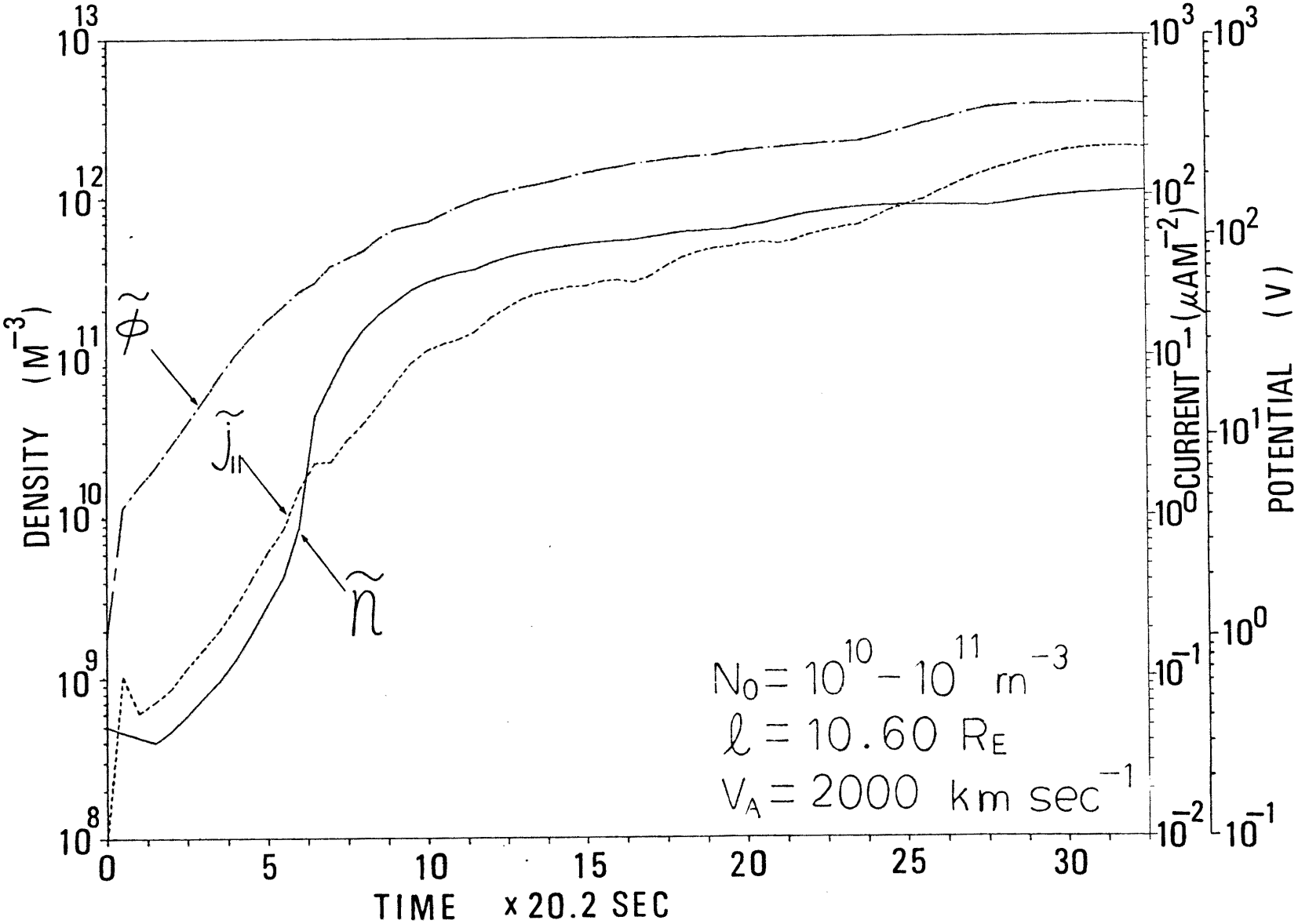
DENSITY (M^{-3})
CURRENT (μAM^{-2})
POTENTIAL (V)
$\tilde{\phi}$
$\tilde{j}_{\parallel}$
$\tilde{n}$
$N_0 = 10^{10} - 10^{11}$ m^{-3}
$\ell = 10.60$ R_E
$V_A = 2000$ km sec^{-1}
TIME x 20.2 SEC

Fig. 14

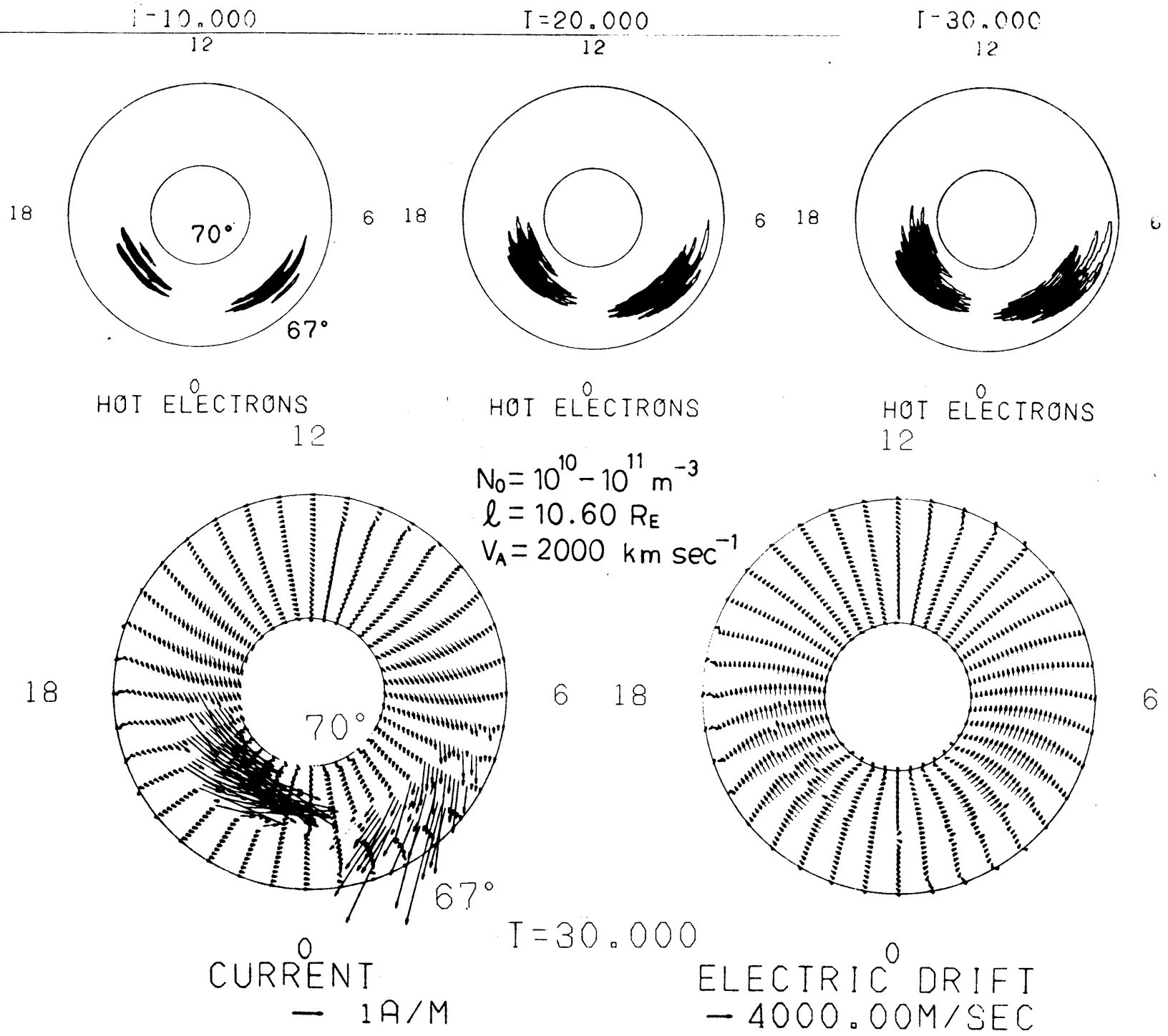
T=10.000
12
18
6
70°
67°
0
HOT ELECTRONS
T=20.000
12
18
6
0
HOT ELECTRONS
T=30.000
12
18
6
0
HOT ELECTRONS
$N_0 = 10^{10} - 10^{11}\ m^{-3}$
$\ell = 10.60\ R_E$
$V_A = 2000\ km\ sec^{-1}$
T=30.000
0
CURRENT
— 1A/M
0
ELECTRIC DRIFT
— 4000.00M/SEC

Fig. 15

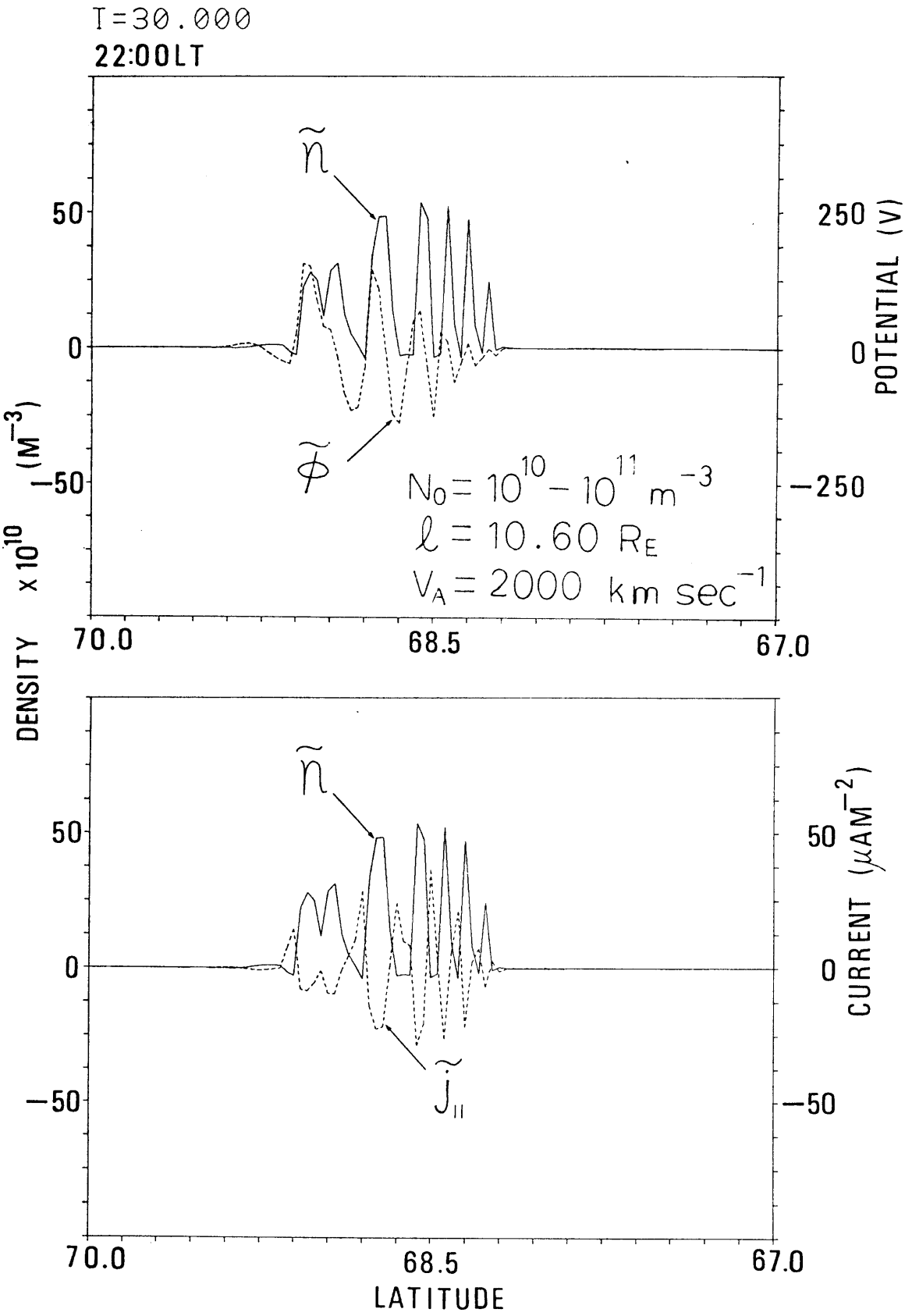
T=30.000
22:00LT
$\tilde{n}$
$\tilde{\phi}$
$N_0 = 10^{10} - 10^{11}\ m^{-3}$
$\ell = 10.60\ R_E$
$V_A = 2000\ km\ sec^{-1}$
50
0
−50
250
0
−250
POTENTIAL (V)
DENSITY $\times 10^{10}$ (M^{-3})
70.0
68.5
67.0
$\tilde{n}$
$\tilde{J}_{||}$
50
0
−50
CURRENT (μAM^{-2})
70.0
68.5
67.0
LATITUDE

Fig. 16

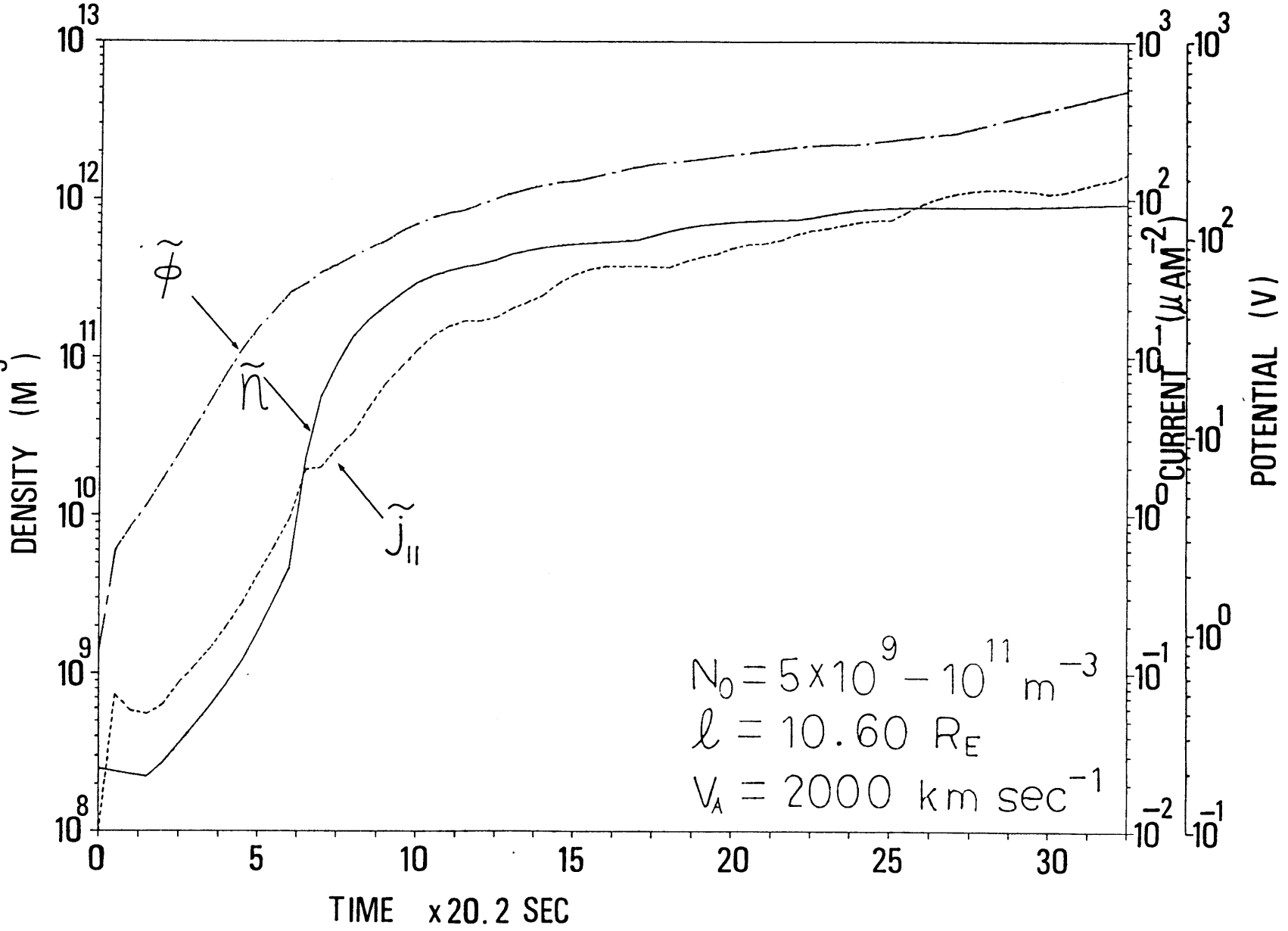
DENSITY (M^{-3})
CURRENT (μAM^{-2})
POTENTIAL (V)
TIME x20.2 SEC
$\tilde{\phi}$
$\tilde{n}$
$\tilde{j}_{||}$
$N_0 = 5 \times 10^9 - 10^{11}$ m^{-3}
$\ell = 10.60$ R_E
$V_A = 2000$ km sec^{-1}

Fig. 17

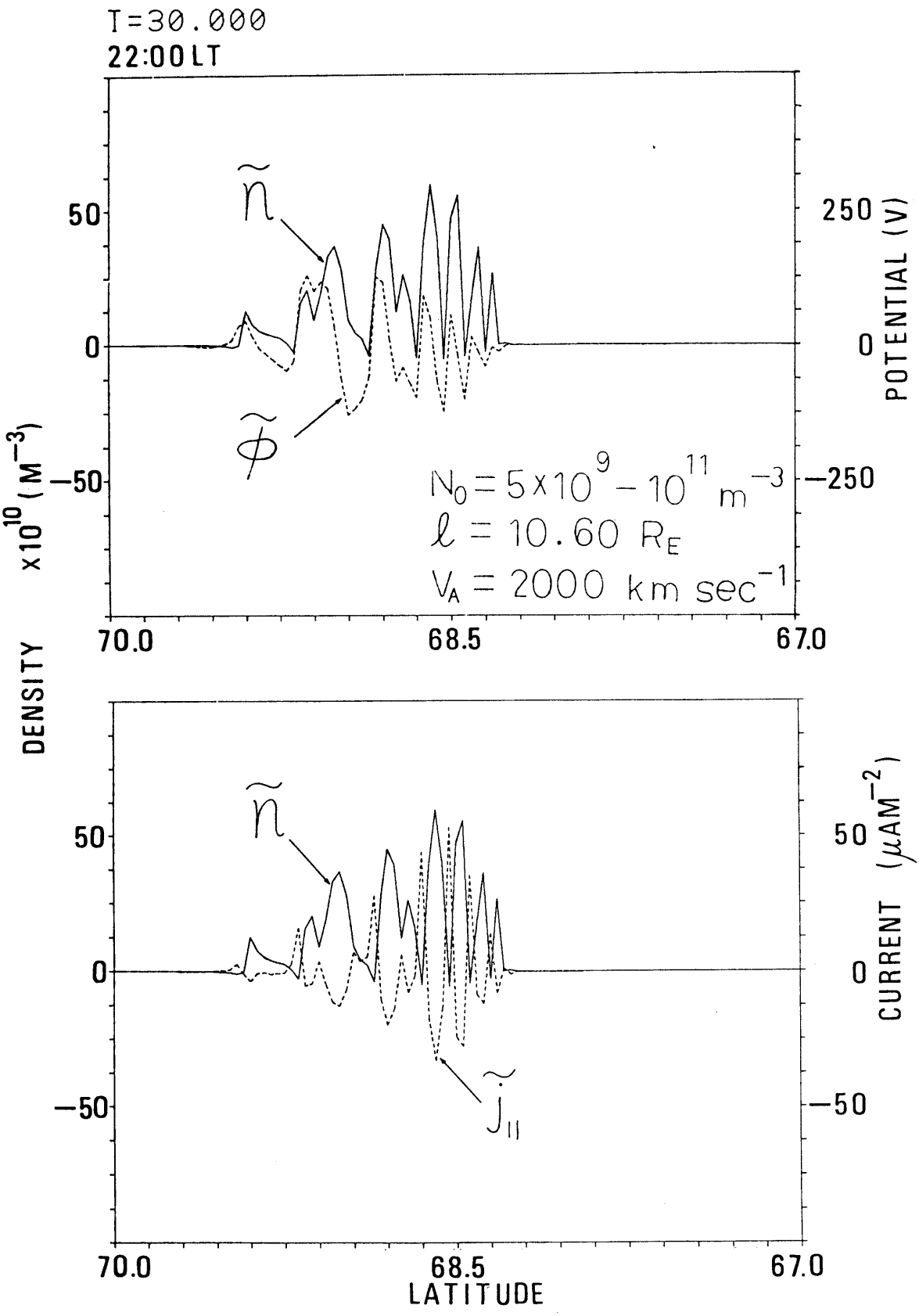
T=30.000
22:00 LT
50
0
−50
250
0
−250
POTENTIAL (V)
DENSITY ×10^10 (M^−3)
ñ
φ̃
N0 = 5×10^9 − 10^11 m^−3
ℓ = 10.60 RE
VA = 2000 km sec^−1
70.0
68.5
67.0
ñ
j̃11
50
0
−50
CURRENT (μAM^−2)
LATITUDE

Fig. 18

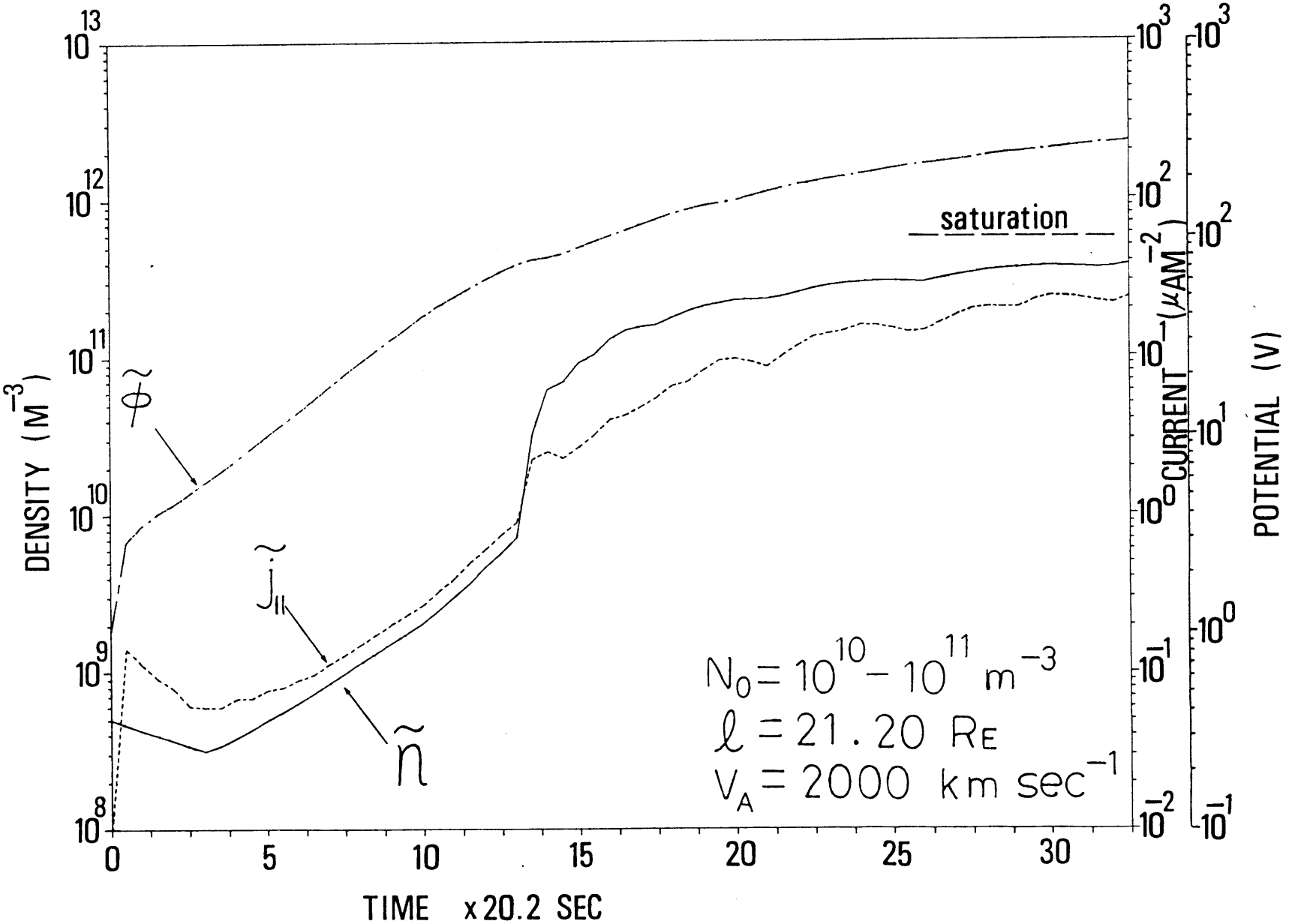
DENSITY (M^{-3})
CURRENT (μAM^{-2})
POTENTIAL (V)
TIME x20.2 SEC
saturation
$\tilde{\phi}$
$\tilde{j}_{\parallel}$
$\tilde{n}$
$N_0 = 10^{10} - 10^{11}\ m^{-3}$
$\ell = 21.20\ R_E$
$V_A = 2000\ km\ sec^{-1}$

Fig. 19

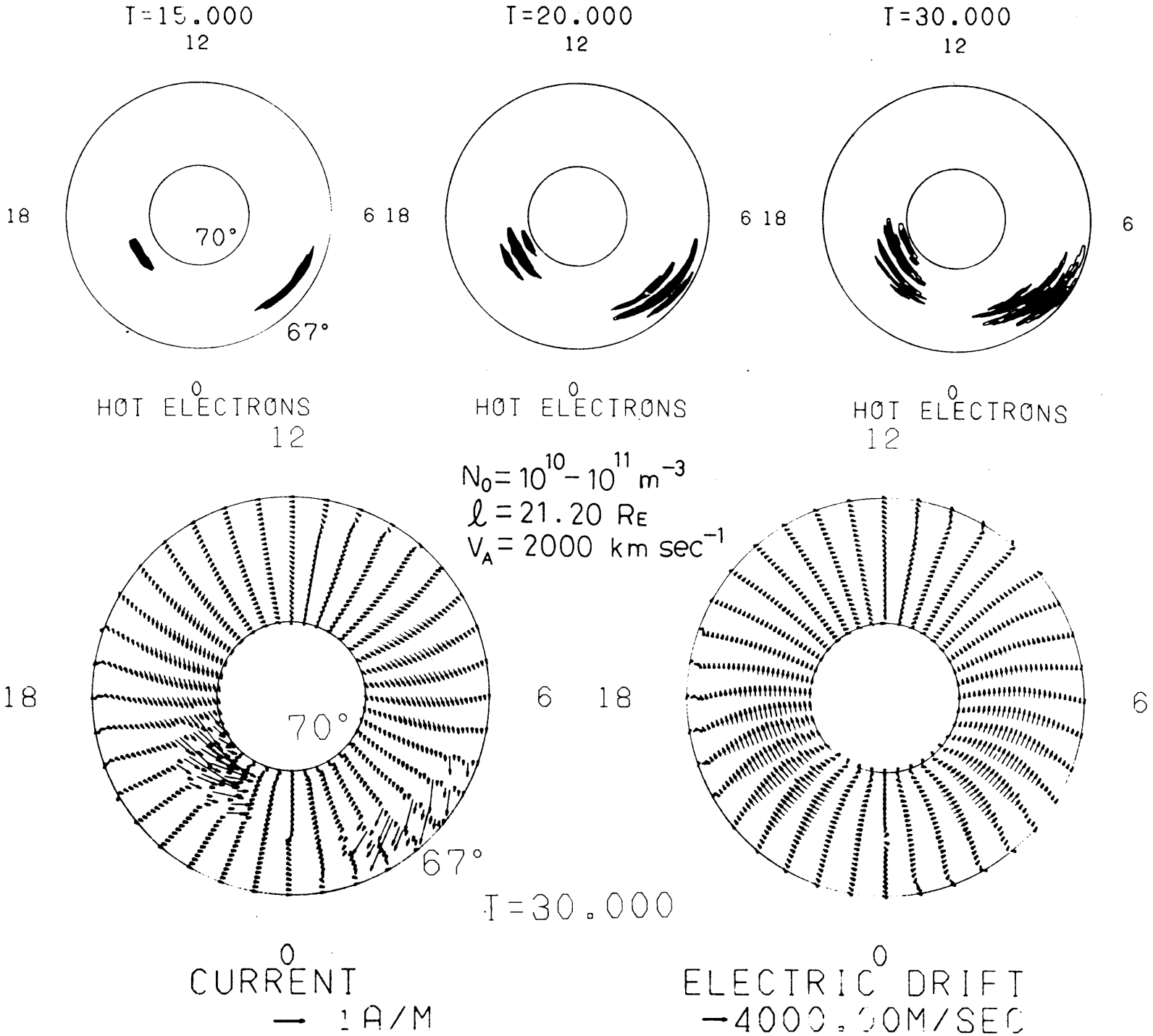
T=15.000
12
18
6 18
70°
67°
HOT ELECTRONS
0
12
T=20.000
12
6 18
HOT ELECTRONS
0
12
T=30.000
12
6 18
6
HOT ELECTRONS
0
12
$N_0 = 10^{10} - 10^{11}\ m^{-3}$
$\ell = 21.20\ R_E$
$V_A = 2000\ km\ sec^{-1}$
18
6
18
70°
67°
6
T=30.000
CURRENT
0
— 1A/M
ELECTRIC DRIFT
0
−4000.00M/SEC

Fig. 20

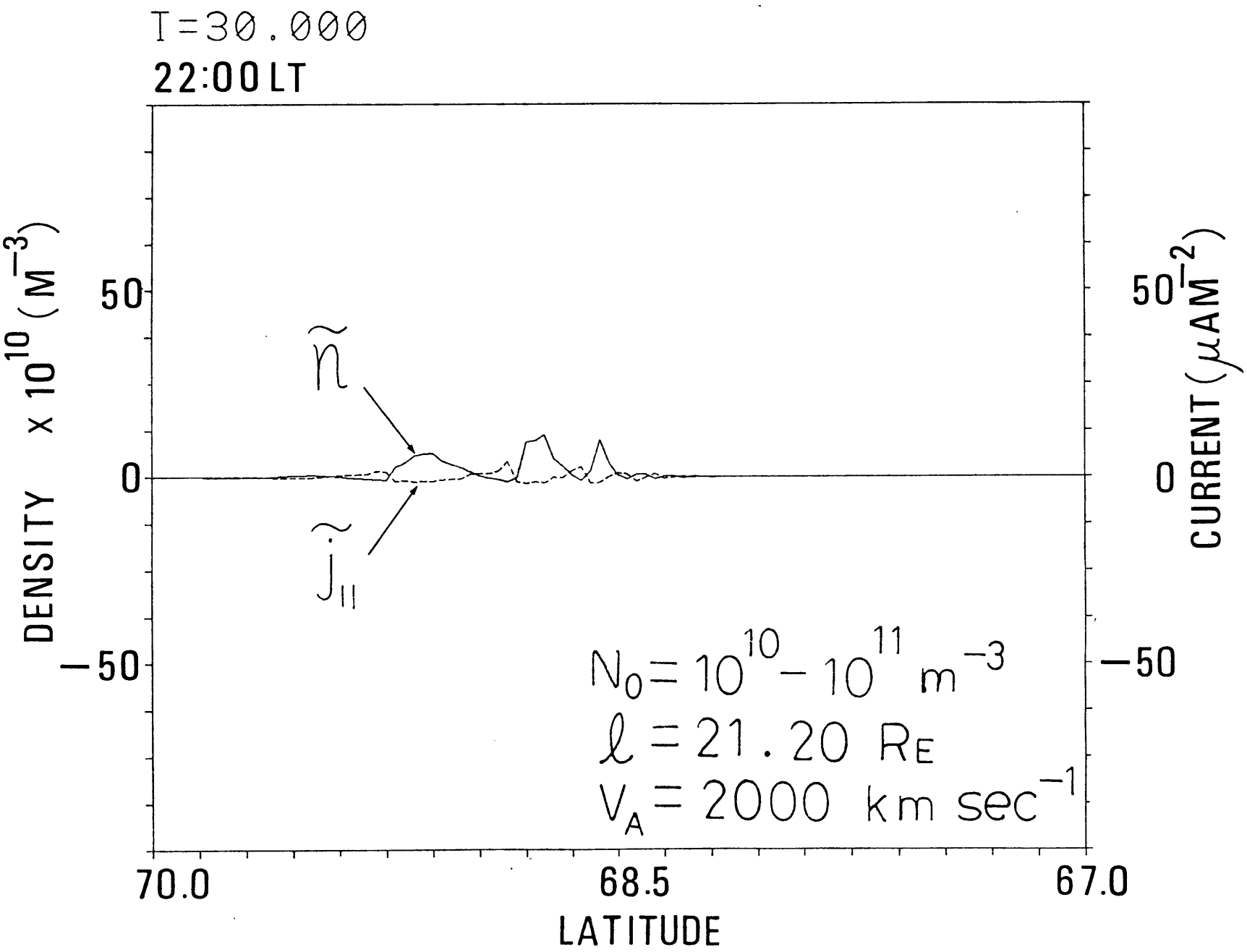
T=30.000
22:00 LT
DENSITY x 10^10 (M^-3)
50
0
-50
CURRENT (μAM^-2)
50
0
-50
ñ
j̃11
N0 = 10^10 - 10^11 m^-3
ℓ = 21.20 RE
VA = 2000 km sec^-1
70.0
68.5
67.0
LATITUDE

Fig. 21

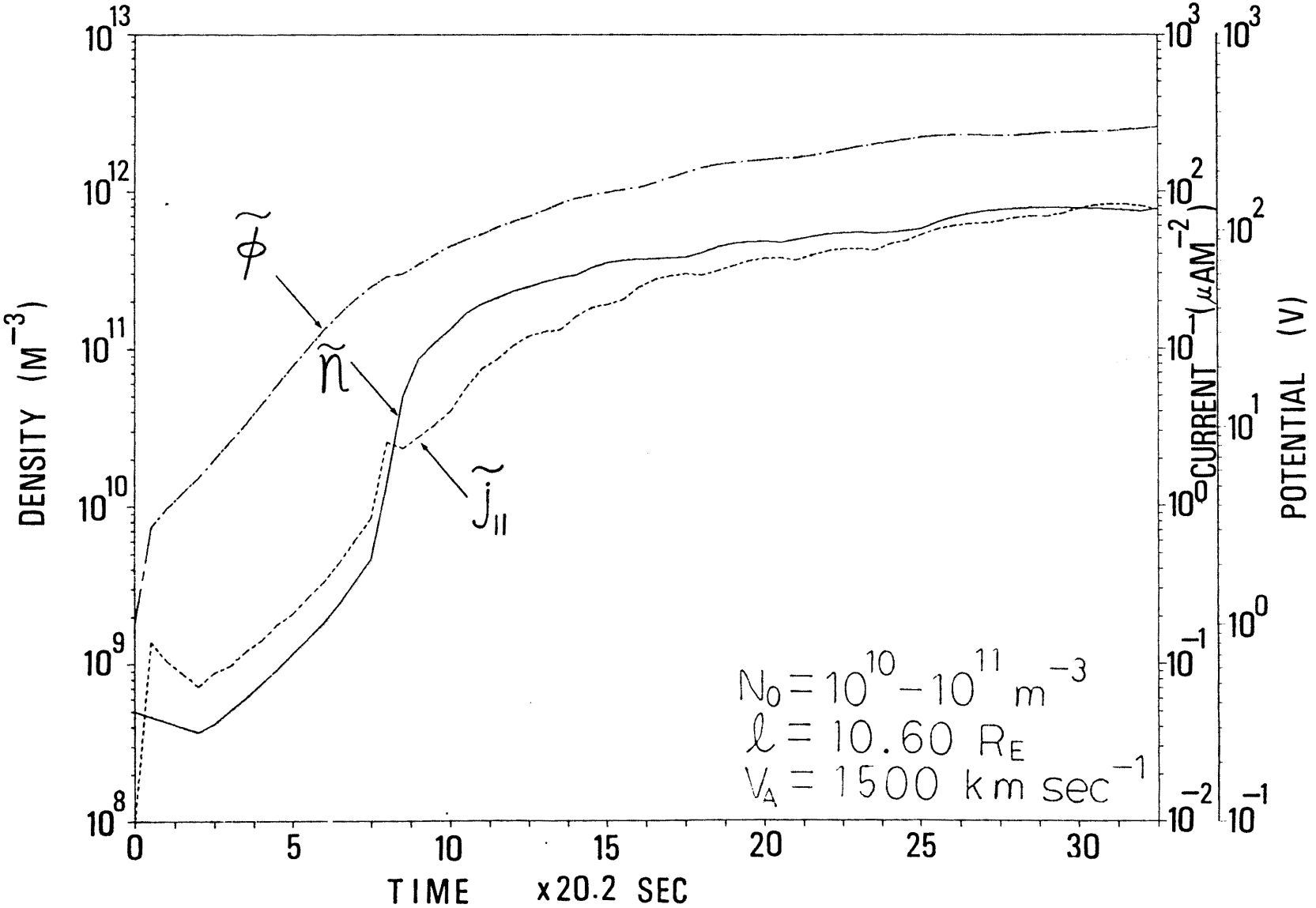
DENSITY (M^{-3})
10^{13}
10^{12}
10^{11}
10^{10}
10^{9}
10^{8}
$\tilde{\phi}$
$\tilde{n}$
$\tilde{j}_{\parallel}$
$N_0 = 10^{10} - 10^{11}\ m^{-3}$
$\ell = 10.60\ R_E$
$V_A = 1500\ km\ sec^{-1}$
0
5
10
15
20
25
30
TIME x20.2 SEC
CURRENT (μAM^{-2})
10^{3}
10^{2}
10^{1}
10^{0}
10^{-1}
10^{-2}
POTENTIAL (V)
10^{3}
10^{2}
10^{1}
10^{0}
10^{-1}

Fig. 22

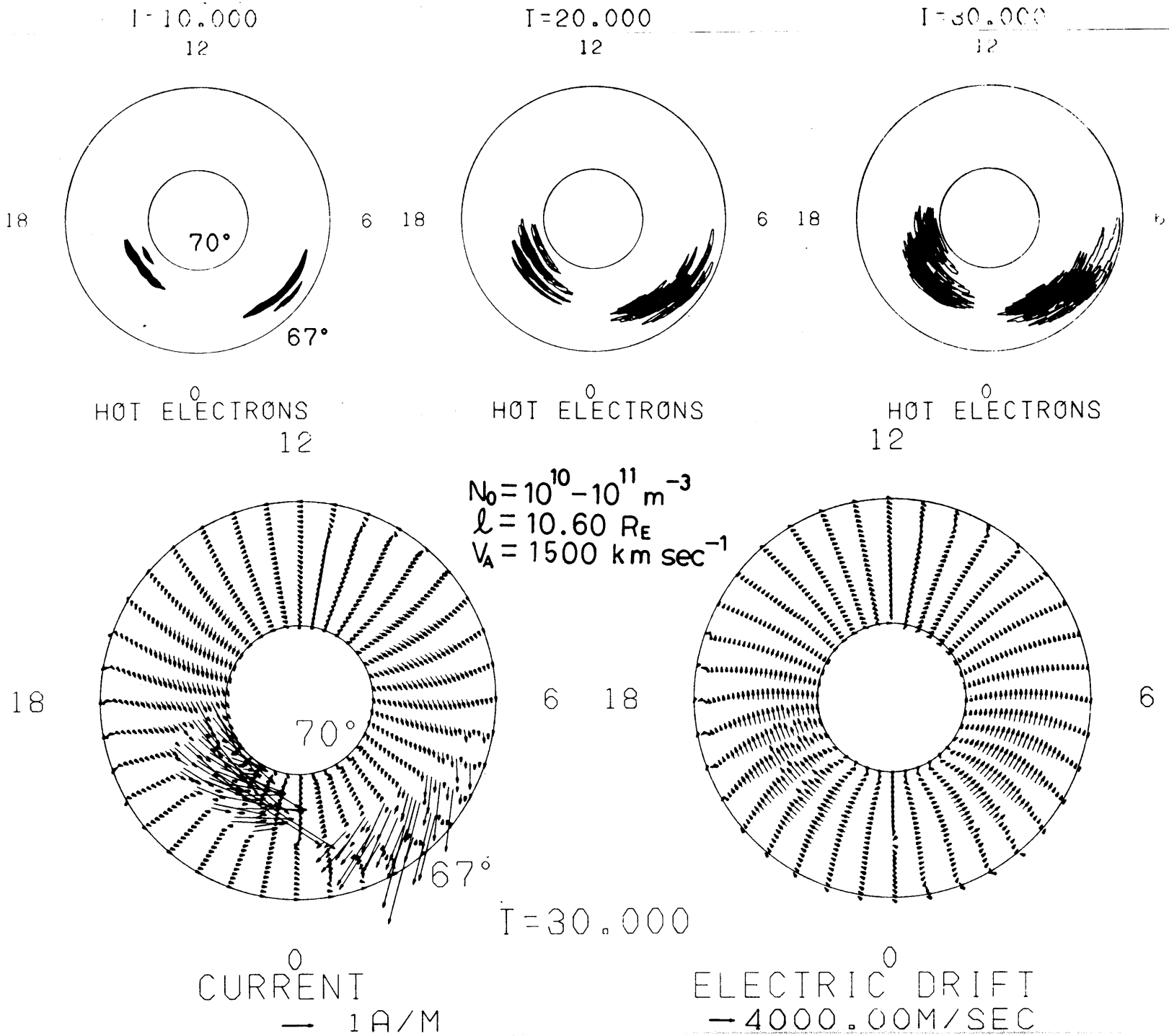
T=10.000
12
18
6
70°
67°
0
HOT ELECTRONS
T=20.000
12
18
6
0
HOT ELECTRONS
T=30.000
12
18
6
0
HOT ELECTRONS
$N_0 = 10^{10} - 10^{11}\ m^{-3}$
$\ell = 10.60\ R_E$
$V_A = 1500\ km\ sec^{-1}$
12
18
6
70°
67°
T=30.000
0
CURRENT
— 1A/M
0
ELECTRIC DRIFT
—4000.00M/SEC

Fig. 23

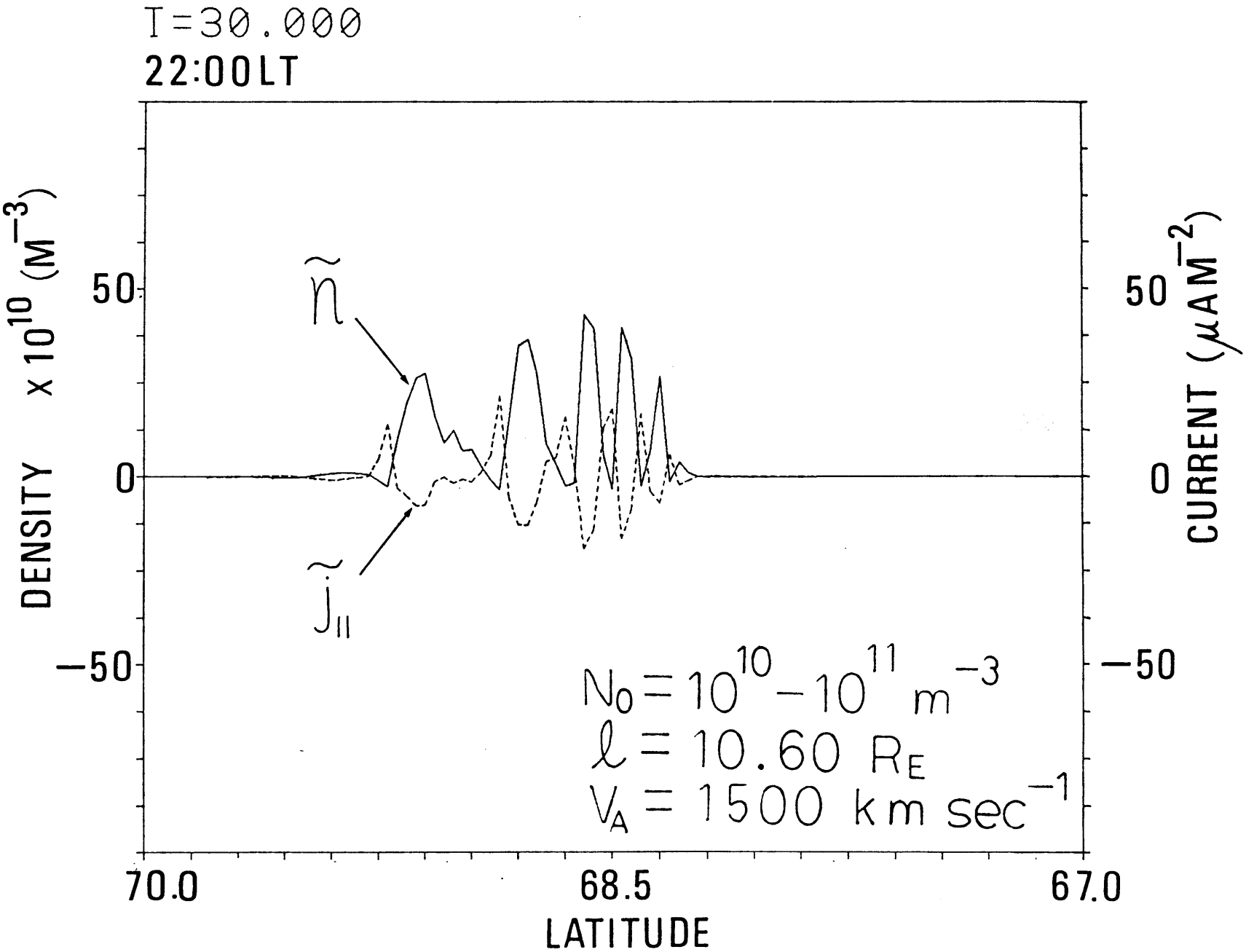
T=30.000
22:00LT
DENSITY x 10^10 (M^-3)
50
0
-50
$\tilde{n}$
$\tilde{j}_{||}$
CURRENT (μAM^-2)
50
0
-50
$N_0 = 10^{10} - 10^{11}$ m^{-3}
$\ell = 10.60$ R_E
$V_A = 1500$ km sec^{-1}
70.0
68.5
67.0
LATITUDE

Fig. 24

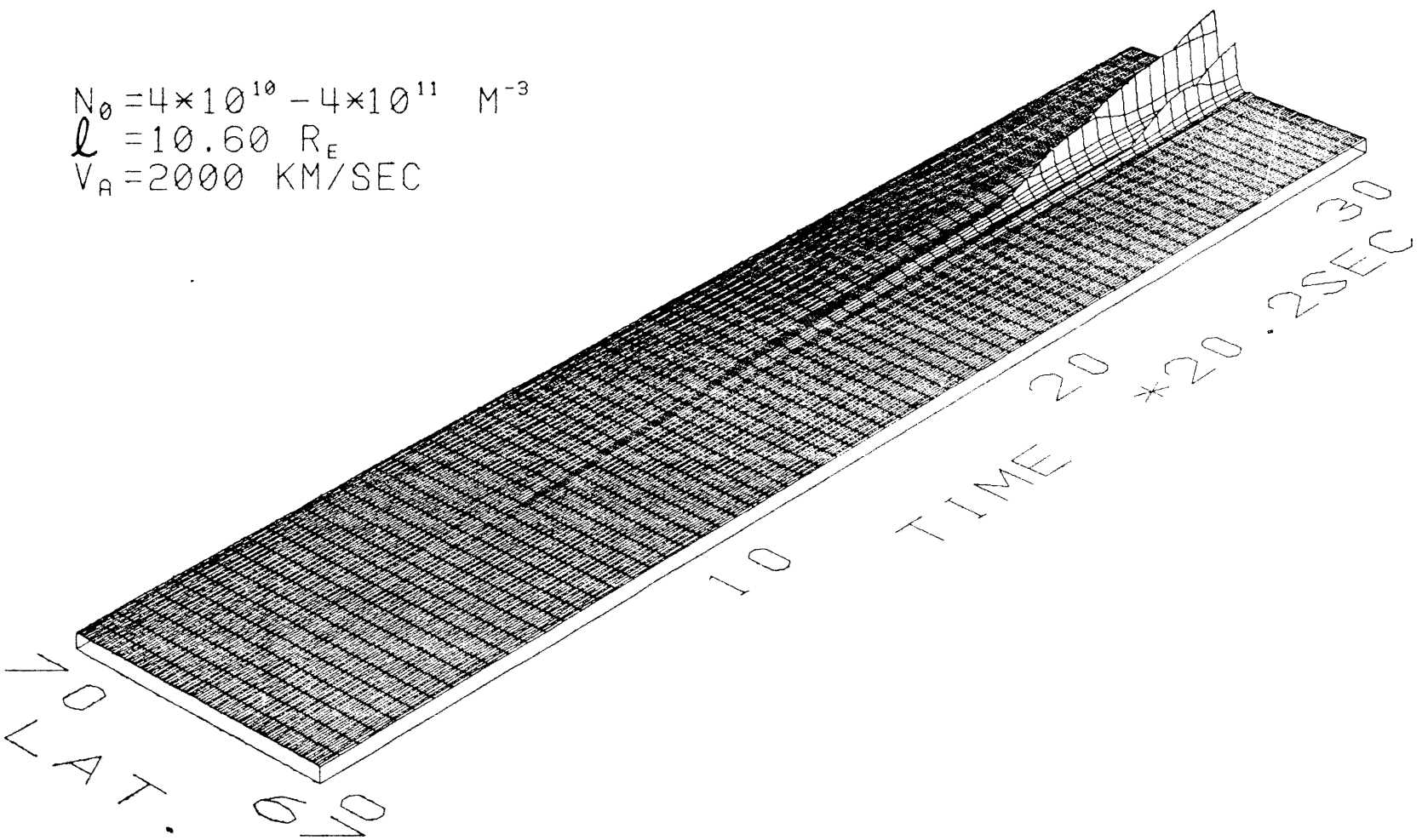

DYNAMIC VIEW OF DENSITY DISTURBANCE AT 22:00LT

Fig. 25

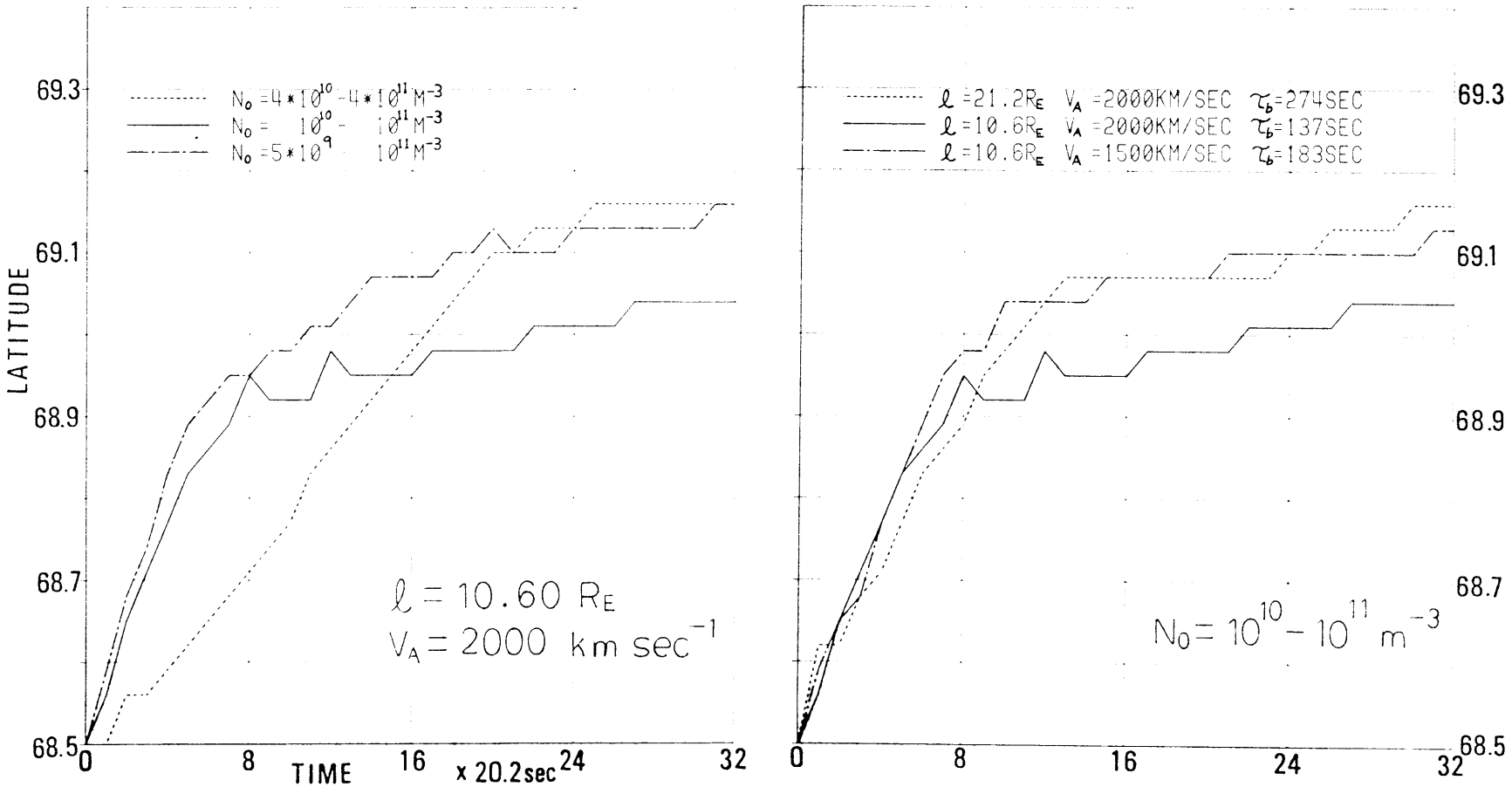
69.3
69.1
68.9
68.7
68.5
LATITUDE
$N_0 = 4*10^{10} - 4*10^{11} M^{-3}$
$N_0 = 10^{10} - 10^{11} M^{-3}$
$N_0 = 5*10^{9} - 10^{11} M^{-3}$
$\ell = 10.60\ R_E$
$V_A = 2000\ km\ sec^{-1}$
0
8
16
24
32
TIME
x 20.2sec
$\ell = 21.2 R_E$ $V_A = 2000 KM/SEC$ $\tau_b = 274 SEC$
$\ell = 10.6 R_E$ $V_A = 2000 KM/SEC$ $\tau_b = 137 SEC$
$\ell = 10.6 R_E$ $V_A = 1500 KM/SEC$ $\tau_b = 183 SEC$
$N_0 = 10^{10} - 10^{11}\ m^{-3}$

Fig. 26

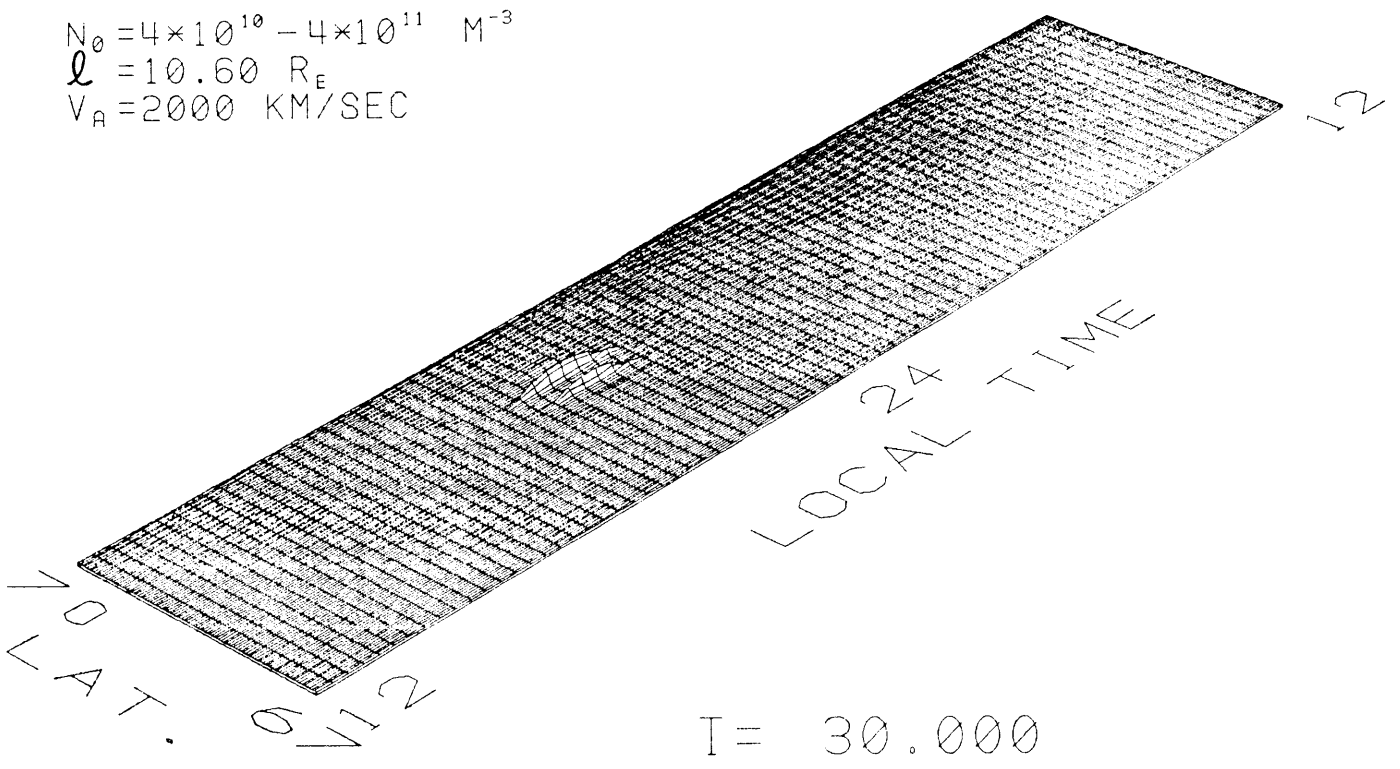

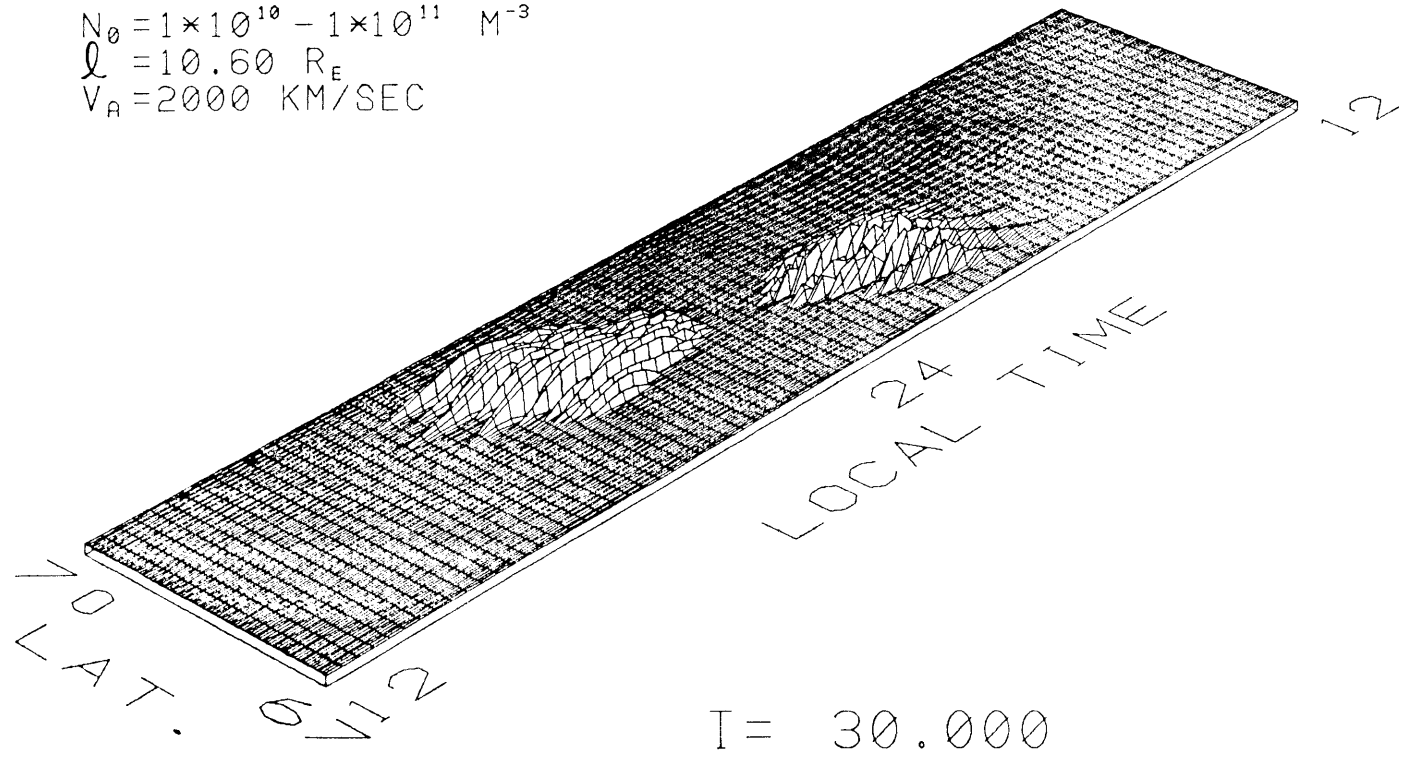

DENSITY DISTURBANCE

Fig. 27

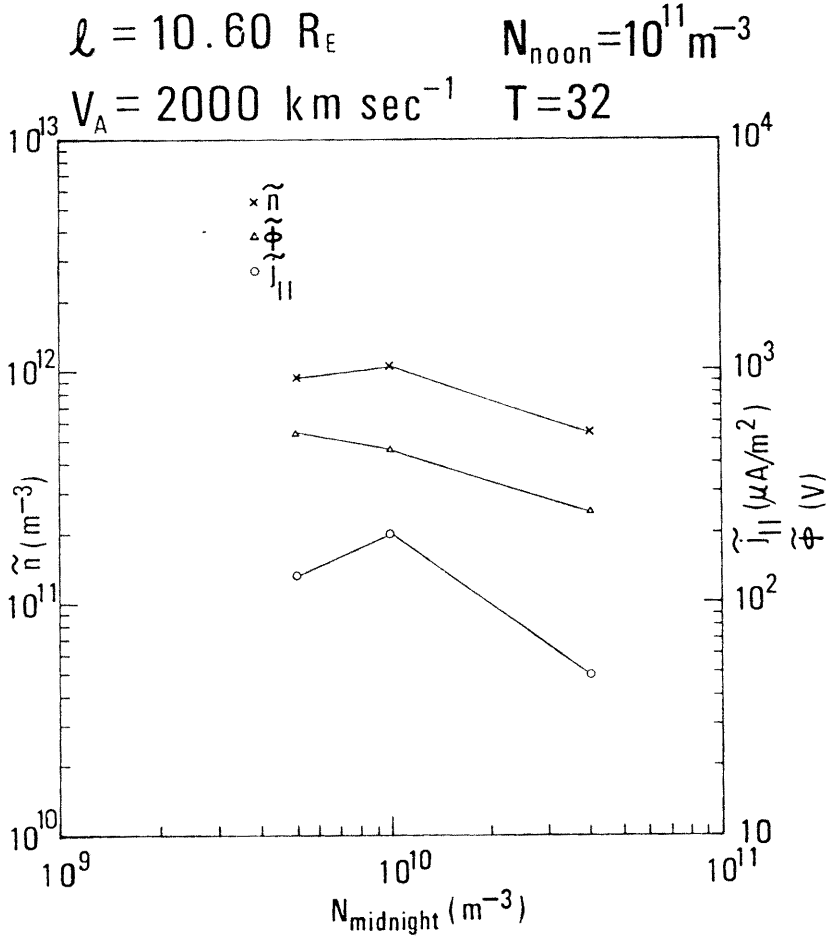
$\ell = 10.60\ R_E$
$N_{noon}=10^{11}m^{-3}$
$V_A = 2000\ km\ sec^{-1}$
$T=32$
10^{13}
10^{12}
10^{11}
10^{10}
10^4
10^3
10^2
10
$\tilde{n}\ (m^{-3})$
$\tilde{j}_{||}\ (\mu A/m^2)$
$\tilde{\Phi}\ (V)$
10^9
10^{10}
10^{11}
$N_{midnight}\ (m^{-3})$

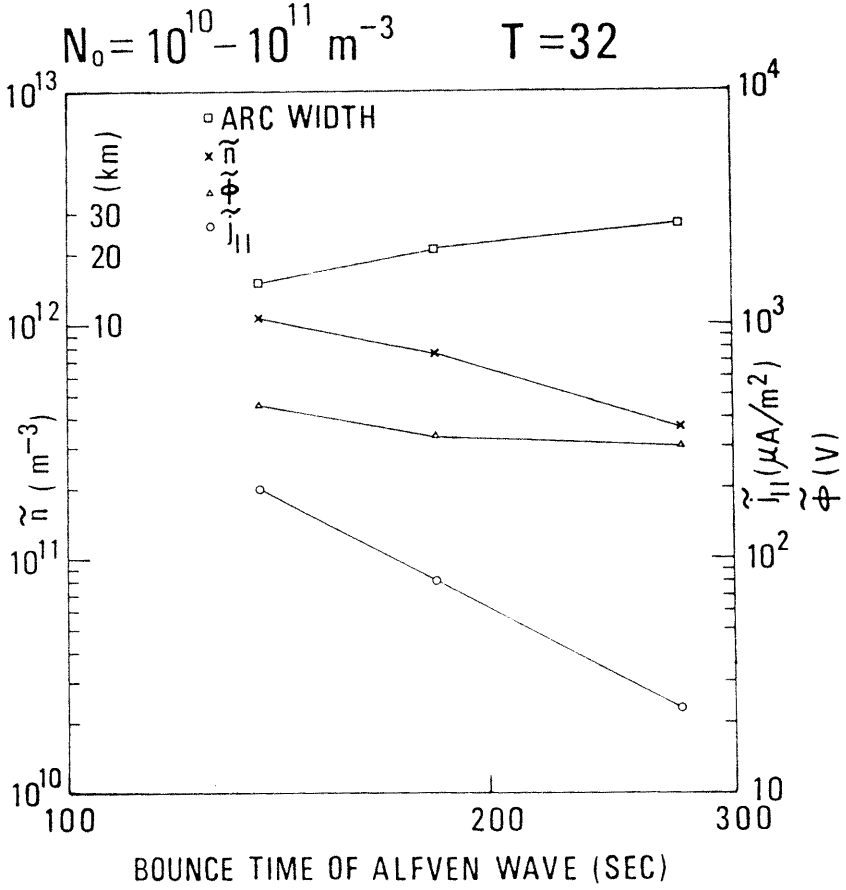
$N_o = 10^{10} - 10^{11}\ m^{-3}$
$T=32$
ARC WIDTH
(km)
30
20
10
10^{13}
10^{12}
10^{11}
10^{10}
10^4
10^3
10^2
10
$\tilde{n}\ (m^{-3})$
$\tilde{j}_{||}\ (\mu A/m^2)$
$\tilde{\Phi}\ (V)$
100
200
300
BOUNCE TIME OF ALFVEN WAVE (SEC)

Fig. 28

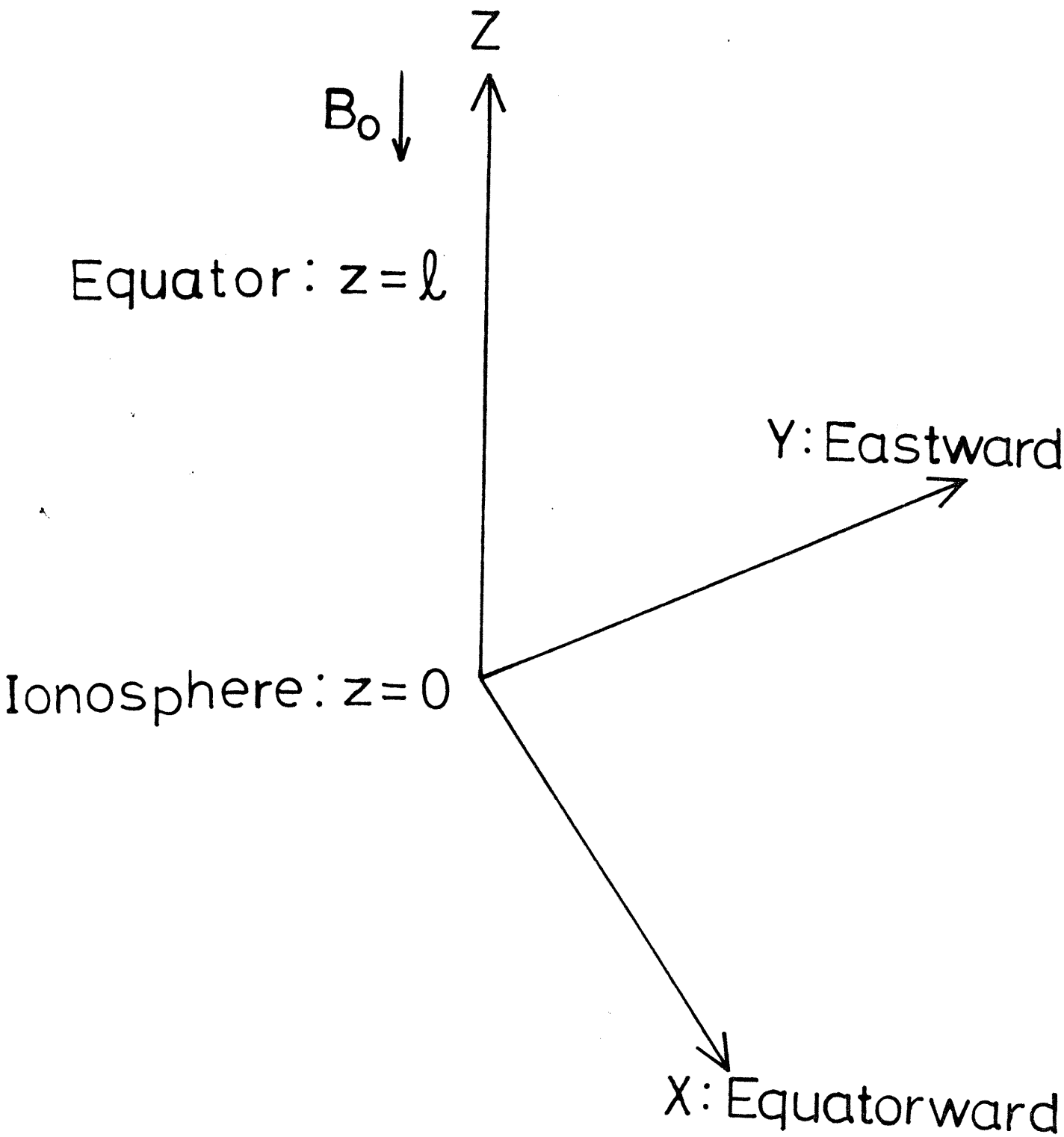

Fig. A.1.

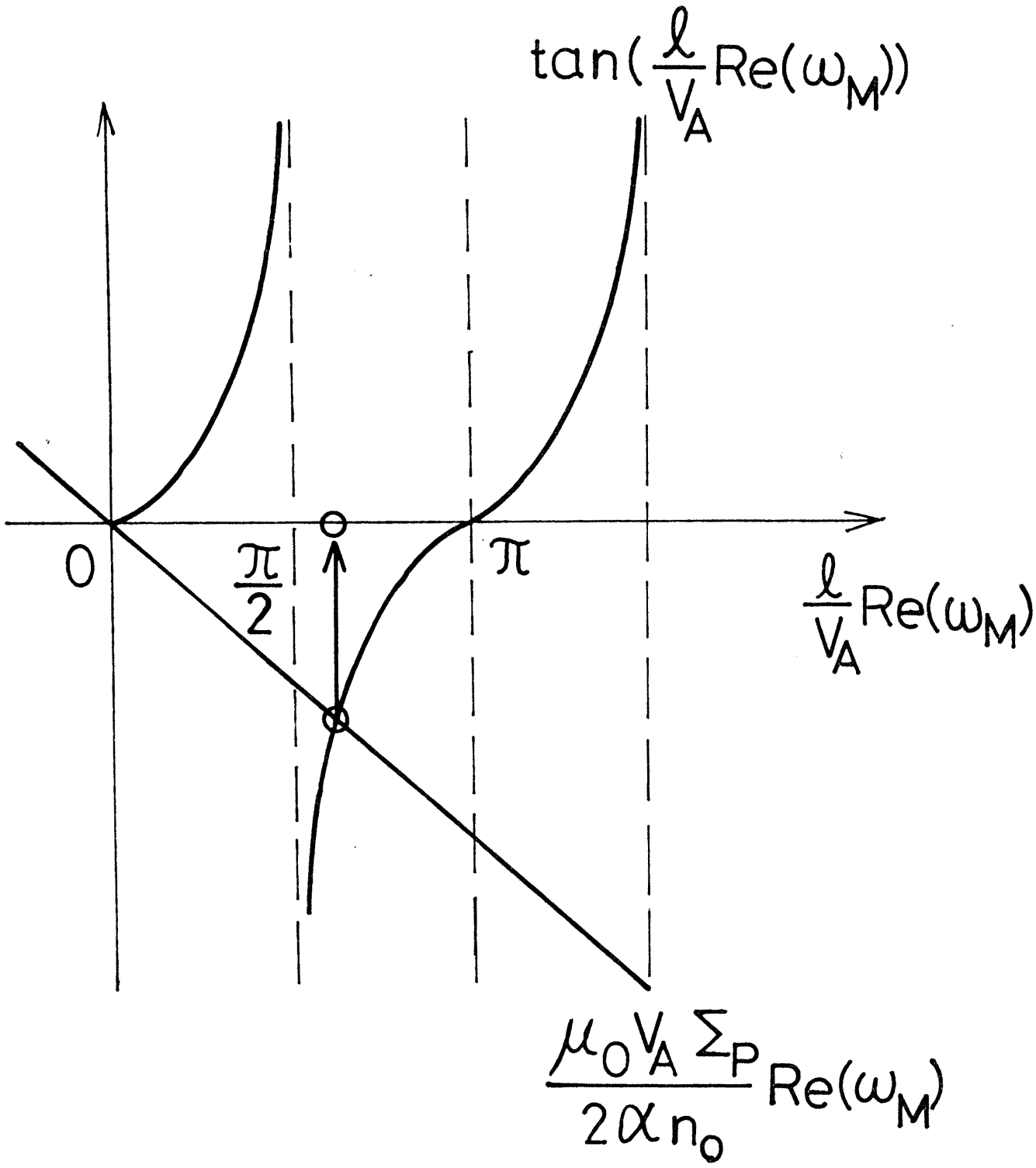
$\tan\left(\frac{\ell}{V_A}\mathrm{Re}(\omega_M)\right)$
0
$\frac{\pi}{2}$
π
$\frac{\ell}{V_A}\mathrm{Re}(\omega_M)$
$\frac{\mu_0 V_A \Sigma_P}{2\alpha n_0}\mathrm{Re}(\omega_M)$

Fig. A.2

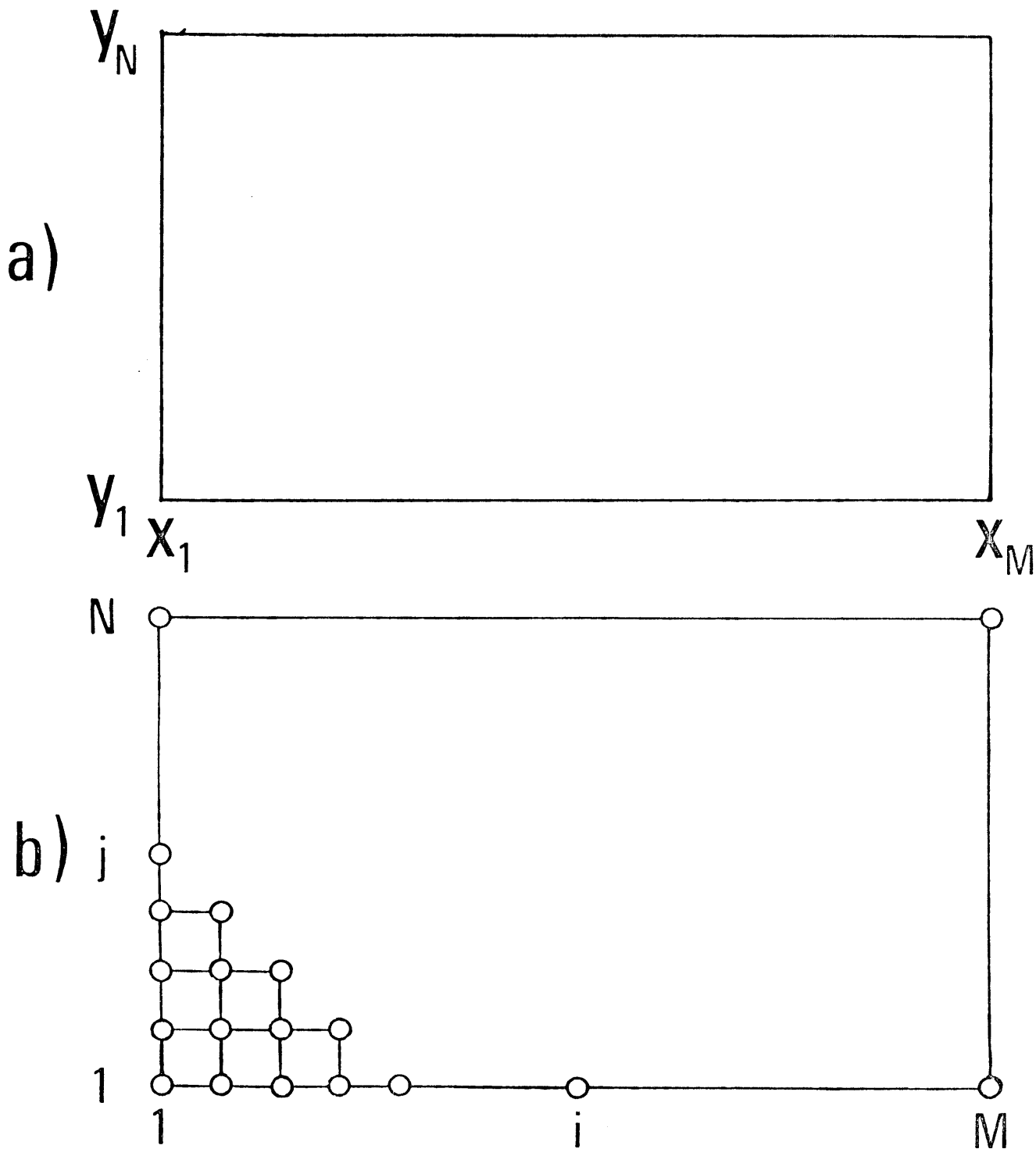

Fig. C.1

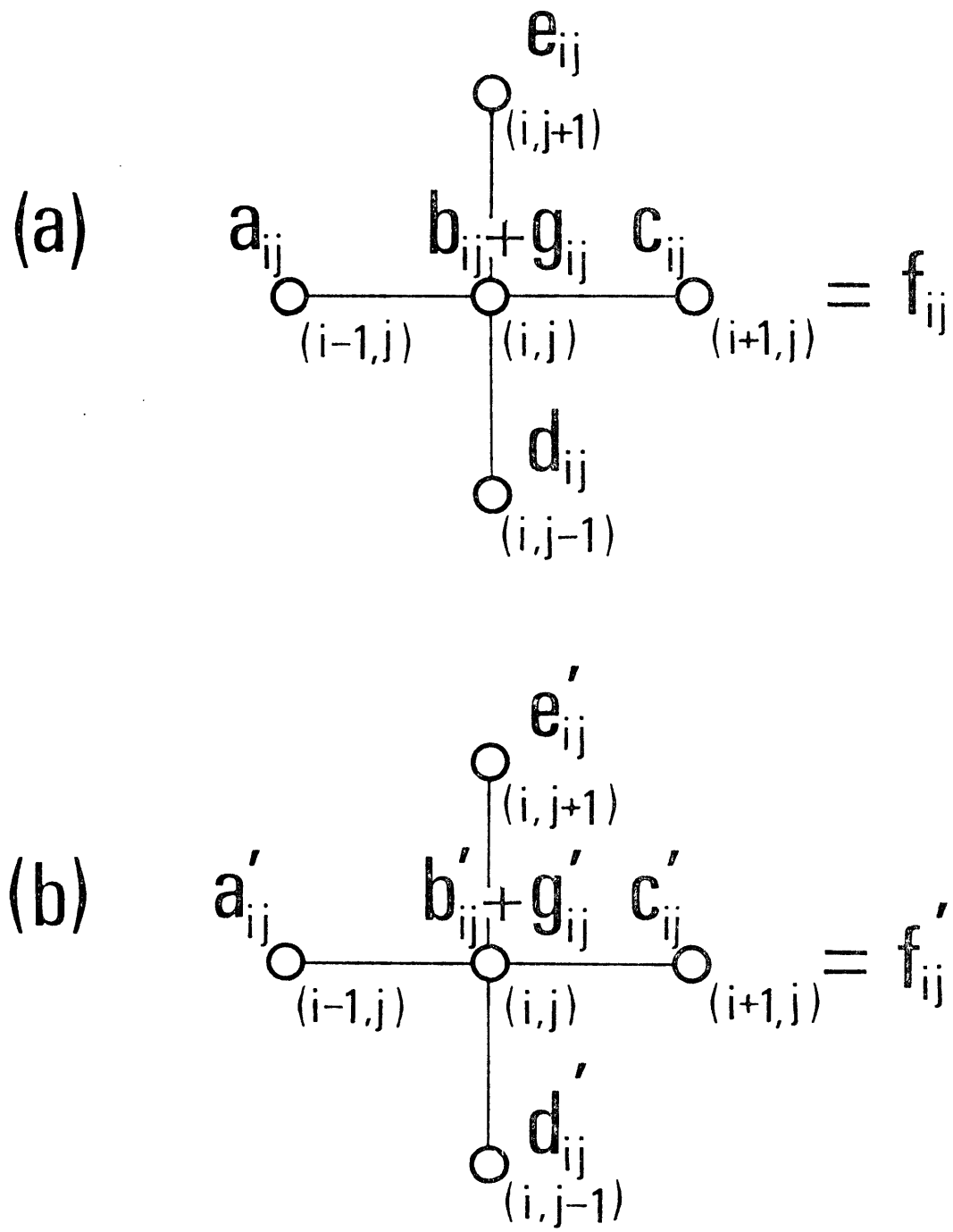
(a)
e_{ij}
(i,j+1)
a_{ij}
$b_{ij}+g_{ij}$
c_{ij}
$= f_{ij}$
(i−1,j)
(i,j)
(i+1,j)
d_{ij}
(i,j−1)
(b)
e'_{ij}
(i,j+1)
a'_{ij}
$b'_{ij}+g'_{ij}$
c'_{ij}
$= f'_{ij}$
(i−1,j)
(i,j)
(i+1,j)
d'_{ij}
(i,j−1)

Fig. C.2

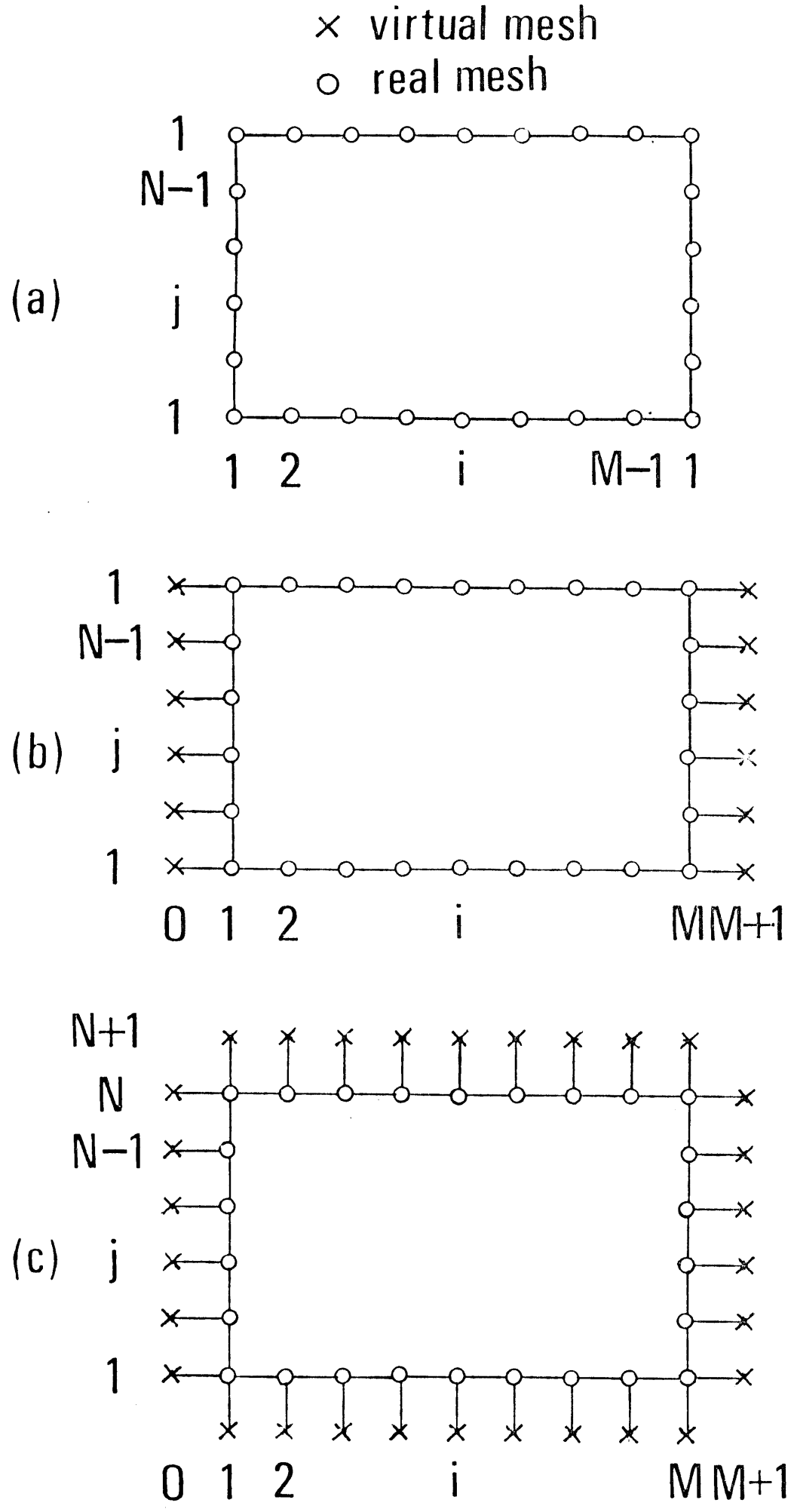
× virtual mesh
○ real mesh
(a)
1
N−1
j
1
1 2 i M−1 1
(b)
1
N−1
j
1
0 1 2 i MM+1
(c)
N+1
N
N−1
j
1
0 1 2 i MM+1

Fig. C.3

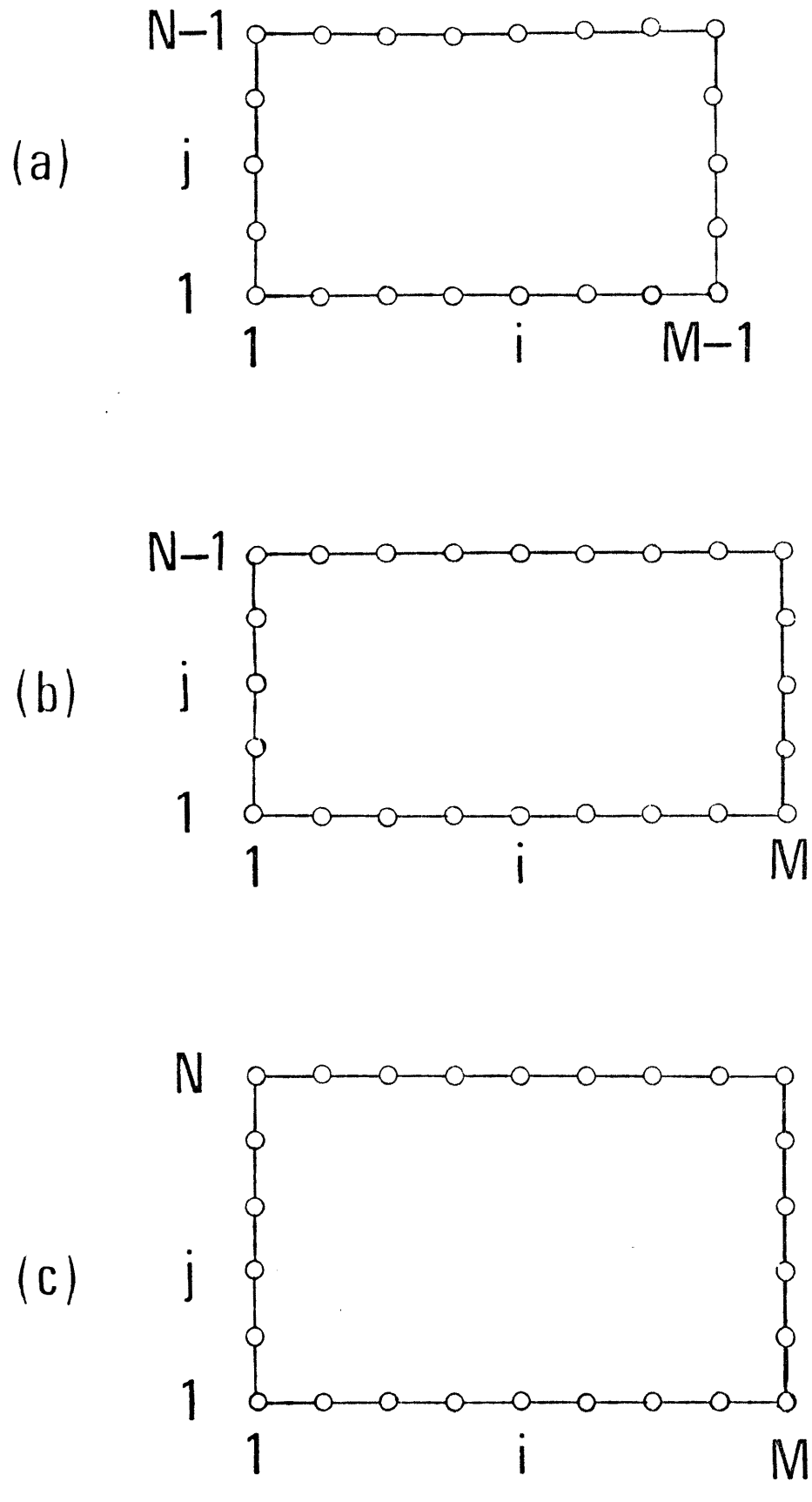

Fig. C.4